VISUAL ACUITY ESTIMATION FROM SIMULATED IMAGES

by

William J. Duncan

A Dissertation Submitted to the Faculty of the

COLLEGE OF OPTICAL SCIENCES

In Partial Fulfillment of the Requirements
For the Degree of

DOCTOR OF PHILOSOPHY

In the Graduate College

THE UNIVERSITY OF ARIZONA

2016

THE UNIVERSITY OF ARIZONA
GRADUATE COLLEGE

As members of the Dissertation Committee, we certify that we have read the dissertation prepared by William J. Duncan entitled Visual Acuity Estimation from Simulated Images and recommend that it be accepted as fulfilling the dissertation requirement for the Degree of Doctor of Philosophy.

Date: April 5, 2016

Jim Schwiegerling

Date: April 5, 2016

Hong Hua

Date: April 5, 2016

José Sasián

Final approval and acceptance of this dissertation is contingent upon the candidate's submission of the final copies of the dissertation to the Graduate College.

I hereby certify that I have read this dissertation prepared under my direction and recommend that it be accepted as fulfilling the dissertation requirement.

Date: April 5, 2016

Dissertation Director: Jim Schwiegerling

STATEMENT BY AUTHOR

SIGNED: William J. Duncan

ACKNOWLEDGEMENTS

I would like to acknowledge my wife for her consistant support, encouragement, and probably most importantly her patience, for without her this work would not be possible. Thank you to my family, without whom I would not be where I am today.

I would like to thank Professor Jim Schwiegerling for his endless freindship, guidance, and insight. Thank you to Professor Hong Hua and Professor José Sasián for serving on my committee and offering useful advice on the topics of my research.

My colleagues in the Visual and Ophthalmic Optics Lab have served as an important outlet for discussing a myriad of topics, including those that hieghtened my understanding of my research. Thank you to Carmen Paleta, Nick Savidis, Dan McCormick, Carl Chancy, Dulce María González Utrera, Ashley Valdez, Eddie LaVilla, Jordan Jur, and Brian Redmen.

Finally, I much grattitude to my friends and colleagues. Every one of you has served as a trusted confidant and supporter. I owe you all so very much.

DEDICATION

To my loving and supportive wife, Pei-Chih.

TABLE OF CONTENTS

LIST OF FIGURES

LIST OF TABLES

ABSTRACT

Simulated images can provide insight into the performance of optical systems, especially those with complicated features. Many modern solutions for presbyopia and cataracts feature sophisticated power geometries or diffractive elements. Some intraocular lenses (IOLs) arrive at multifocality through the use of a diffractive surface and multifocal contact lenses have a radially varying power profile. These type of elements induce simultaneous vision as well as affecting vision much differently than a monofocal ophthalmic appliance. With myriad multifocal ophthalmics available on the market it is difficult to compare or assess performance in ways that effect wearers of such appliances. Here we present software and algorithmic metrics that can be used to qualitatively and quantitatively compare ophthalmic element performance, with specific examples of bifocal intraocular lenses (IOLs) and multifocal contact lenses. We anticipate this study, methods, and results to serve as a starting point for more complex models of vision and visual acuity in a setting where modeling is advantageous. Generating simulated images of real-scene scenarios is useful for patients in assessing vision quality with a certain appliance. Visual acuity estimation can serve as an important tool for manufacturing and design of ophthalmic appliances.

CHAPTER 1

INTRODUCTION

The human eye, while an impressive optical system, is sensitive to many different pathologies especially in older eyes. The most common malady is presbyopia. Presbyopia is a progressive condition in which the crystalline lens hardens over time causing a diminished ability to accommodate. Displayed in Figure 1.1 is a schematic layout of the human eye. This dissertation will discuss certain aspects of three main bodies within the eye. The cornea, crystalline lens (labeled "lens" in Figure 1.1), and the retina.

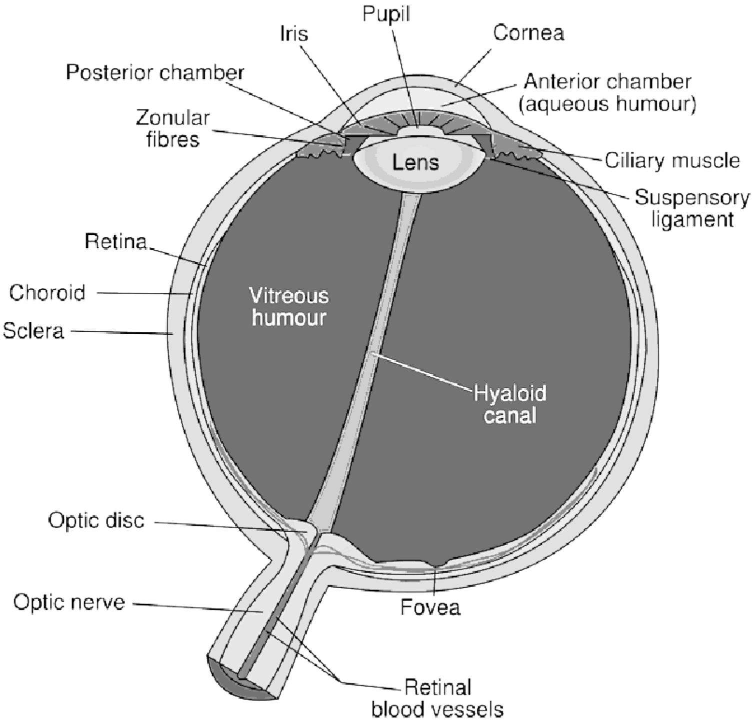

Figure 1.1: Schematic layout of human eyeball. Image reproduced under license from Creative Commons.

Accommodation is the process of the crystalline lens changing shape, which induces a change in the overall optical power, allowing the eye to focus at different distances or vergences. Presbyopia comes from the Greek words for “old eye” and is a condition that progresses throughout life, but is typically not noticed until a person is in their mid-40s. Children can accommodate upwards of 10 diopters (D), meaning they can clearly focus on objects ranging from infinity to as near as 10cm **[1]**.

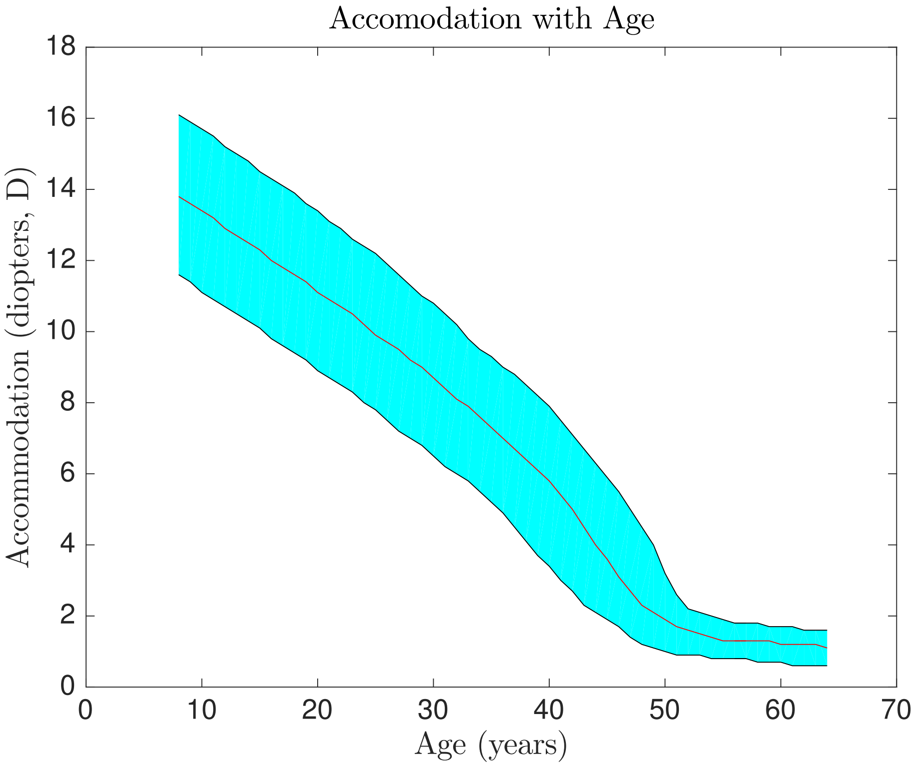

Figure 1.2: Accommodation as a function of age. Measured and presented by Duane, 1922 [1]. Shaded cyan region shows the extent from maximum measured accommodation to minimum measured accommodation. Red line in the mean of Duane’s clinical population.

This accommodation range steadily diminishes to about 2D in the fifth decade, reducing the range of clear focus from infinity to about 50 cm from the eye. Further aging reduces the accommodation to near zero in the ensuing decade. Reading text is usually done at a patient’s near plane, which is the closest point at which they can focus. Once the accommodative ability falls below 3D, corresponding to a point about 330mm in front of the patient, reading becomes difficult. This is because the eye must be able to focus on the reading plane, and if accommodation has diminished to less than 3D, they eye cannot focus close enough. This value of 3D - corresponding to a point about 330mm in front of the patient - is dictated essentially by the length of the person's arms i.e. how far they can extend the reading plane in front of them.

Treatments for presbyopia provide additional optical power to a patient's corrective prescription . The prescription fixes their focus to infinity and the "add" power provides the additional power require to see closer objects. The most familiar presbyopic correction is a pair of reading glasses. Here the add power is mounted in a spectacle frame, but requires the user to remove existing distance spectacle (if needed) and replace them with near spectacles. The logistics of carrying multiple spectacles and switching between various tasks is tiresome. Consequently, presbyopic correction that provides two or more powers within the same platform are desirable. The earliest example of this type of correction are bifocal spectacle lenses, in which an additional positive power lens is added to the lower portion of a patient's spectacle lenses. In the early days of bifocal spectacle lenses, the upper and lower half of one's spectacles were actually separate lenses. The invention of this type of bifocal lens is widely attributed to Ben Franklin [5, 6]. Progressive Addition Lenses (PALs) are another presbyopic treatment that has evolved since the middle of the last century. Here, the spectacle lens power gradually changes from the top - distance correction - portion and the bottom - near correction - portion.

While bifocal spectacle lenses and progressive addition spectacle lenses are widely used as treatment for presbyopic patients, both present drawbacks. Bifocal spectacle lenses, in all forms, cause image jump. This is where the image of a continuous object is not continuous due to the discontinuity in optical power of the lens. Figure 1.3 shows an example of image jump in a bifocal spectacle lens.

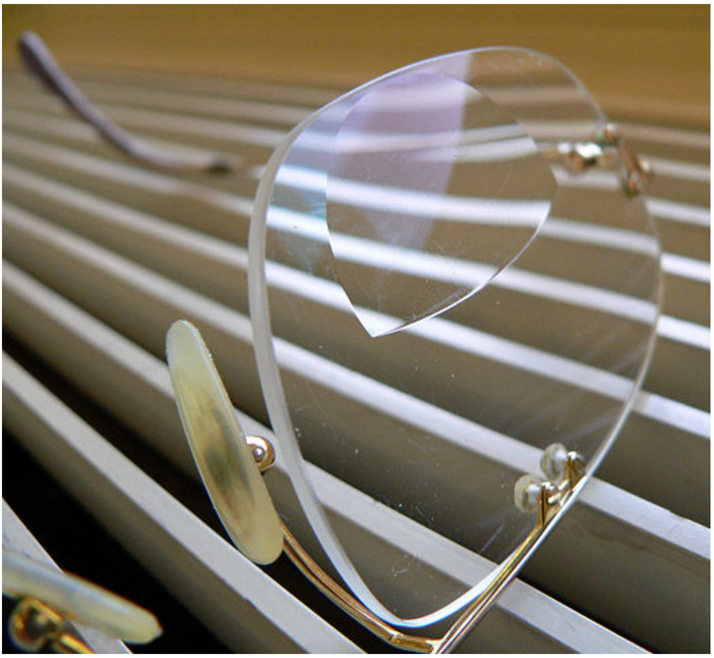

Figure 1.3: Bifocal spectacle lens. Image just can be seen in the right lens at the discontinuity from the distance corrective portion of the lens (lower portion in the image) to the near vision correction portion (inset). Image licensed under the Creative Commons.

Progressive addition lenses solve the matter of image jump presented by bifocals, but present a new set of drawbacks. Due to the nature of a PAL surface, within the intermediate and near correction areas, the field of view will be reduced since the near and intermediate portions of the lens do not cover the width of the lens. Further, these regions will exhibit astigmatism since the local power of these regions depends upon the meridian chosen.

More recently, multifocal contact lenses have emerged as a treatment for presbyopia. Since these lenses are on the eye, they cannot operate with the mechanism as spectacle lenses. In spectacle lenses, the eye can rotate behind the lens to select different regions of power. Contact lenses move with the eye and therefore rely on simultaneous vision to provide presbyopic correction. As an aside, the discussion here will only pertain to "large" contact lenses, meaning contact lenses that cover the entire cornea and part of the sclera (the white part of the eye, see Figure 1.1). Rigid Gas Permeable (RGP) lenses are smaller lenses that do not cover the entire cornea and in some cases are available as multifocals. Multifocal RGP lenses can be pushed up by the lower eye lid during a downward gaze, to select a different portion of the lens to be over the pupil. We will limit our discussion to the more widely used simultaneous vision multifocal contact lens that is stationary on the eye.

In the simplified case of bifocals, simultaneous vision in contrast to gaze-angle selection and monovision, presents two concurrent images to the eye. One in focus, and other out of focus. The presentation of a sharp and blurred image simultaneously causes a contrast loss as well as requiring the brain to process which image is desired. Not all wearers of simultaneous vision ophthalmics tolerate the contrast loss or effective learn process the images correctly.

While many different designs are present in the market, they generally fall into two categories, center-near and center-distance. In a center-near contact lens, the central portion of the contact lens provides near-vision correction and the outer portion provides distance-vision correction. Center-distance contact lenses are the opposite, the central portion provides distance correction while the outer part of the lens provides near correction. Both of these designs have variations with gradual changes in power as a function of radius and abrupt changes is power as a function of radius, i.e. power zones. With a gradual change in power from the apical portion to the edge, the lens can no longer be thought of as a bifocal lens. There are no longer two distinct planes in front of the wearer that are in focus on the retina. Now, there is a continuum of object distances that contribute to an in-focus image. This effect is an example of extended depth of focus. More will be elaborated on multifocal contact lenses in Chapter 4. Figure 1.4 shows an example power profile for a center-near multifocal contact lens.

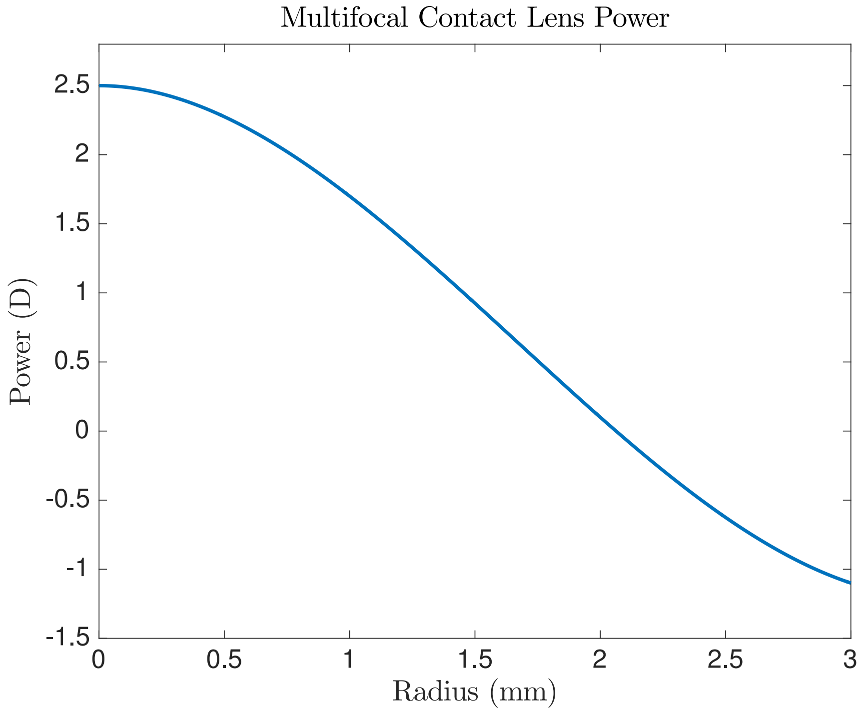

Figure 1.4: Example center-near multifocal contact lens radial power profile. Note that the central portion of the contact lens will have a high add power that decreases as the radius increases.

Another solution for the treatment of presbyopia currently in the final stages of Food and Drug Administration (FDA) approval at the time of writing, is the ReVision Optics Raindrop Near Vision Corneal Inlay. The Raindrop inlay is a small hydrogel disk, about 2mm in diameter, which is placed under an intra-stromal corneal flap. Once the Raindrop inlay has been placed and corneal flap replaced, the cornea has been effectively transformed into something that looks like a center near contact lens. A small portion of the cornea, in the center of the pupil, has an increased curvature and therefore an increased “add” power. This region provides the patient with near vision correction. The outer part of the cornea, unchanged by the Raindrop inlay, continues to function as expected. Providing the patient with distance vision. The Raindrop Near Vision Corneal Inlay is a simultaneous vision ophthalmic device, much like simultaneous vision multifocal contact lenses.

Cataracts are a second common malady of the aging eye and in some cases, the young eye due to certain pathologies. Cataracts are an opacification of the crystalline lens, see Figure 1.1 labelled “lens”). The presence of cataracts can cause diminished vision or if left untreated, blindness. The opacification of the lens causes light entering the eye to scatter and not form an image on the photosensitive layer of the eye, the retina. Cataracts are commonly treated by removing the crystalline lens and replacing it with an artificial lens, called an intra-ocular lens (IOL).

After cataract surgery and the replacement of the natural lens with an IOL, the eye has no ability to accommodate. This isn’t usually an issue, since most who suffer from cataracts have lost most or all of their ability to accommodate. One solution for providing patients with near and distance vision is to correct one eye for near vision and the other eye for distance vision, i.e. monovision. Unlike contact monovision correction, IOL monovision correction predicates that both eyes have cataracts and are treated concurrently. Although there have been many attempts at creating an accommodating IOL and many failures, this is a less common treatment route than using a multifocal IOL. Multifocal IOLs provide simultaneous vision, like that of contact lenses, but different in that they usually employ a diffractive surface to achieve multiple foci. One example that will be elaborated on in Chapter 4 is the AcrySof IQ ReSTOR Multifocal IOL from Alcon Laboratories (Fort Worth, Texas). The ReSTOR IOL has a spherical refractive anterior surface, and an apodized diffractive posterior surface. The refractive part of the lens creates the distance focus, and the diffractive part creates the near focus.

Visual acuity is a common clinical measure of visual performance. It is essentially a resolution test for the on-axis portion of the visual field. Optical system performance is usually measured with some other metric, for example, the Modulation Transfer Function (MTF) is common. The MTF captures information regarding contrast loss in the optical system. Ocular or visual performance encompasses many additional effects that are not captured by the MTF of a single element or of the entire optical system. Take the example of contact lenses. Contact lenses require a certain amount of hydration in order to perform as designed. As such, ocular hydration, blinking, and tear film dissipation can all effect the performance of an eye [7]. These effects lead to scatter, stray light, and transient aberrations.

This dissertation aims to develop software tools in order to simulate images as seen through different ophthalmic elements. Further, we wish to develop the functionality to estimate and predict visual acuity when certain multifocal ophthalmic elements are in use. Comparisons to clinical data are shown for a few examples of these types of ophthalmic elements.

1.1 Software

1.1.1 Simulated Images

Previous authors have enumerated methods for simulating retinal images [8]. It has been shown that there are means for directly measuring ocular wavefront error and in turn using these data to reconstruct blurred images. A Shack-Hartmann wavefront sensor (SHWFS) is a typical instrument used in the research setting for this task. In this work, we have not included the added level of sophistication proposed previously, including patient specific corneal topographic data or complete ocular wavefront error. Nevertheless this would be a relatively simple extension for customized, patient specific retinal images. Although, if one were to go to the trouble of measuring corneal topographic data, the complete ocular wavefront aberration of a patient could be measured with the same relative ease, providing a more accurate representation of a patient specific retinal image.

In this work, we have developed the tools necessary to simulate images in a streamlined way for an arbitrary optical system, given some set of information about it e.g. wavefront error, physical prescription, or power profile. Further, the software has the ability to find “best” focus for an images set. This feature was needed with much of the data used for simulating images from multifocal contacts. Here, the data included a measurement offset not directly linked to the lens power or add-power. More will be elaborated on this in Chapter 5.

1.1.2 Estimating Visual Acuity

A second software package developed by the author, along with Dr. Alan Lang (ReVision Optics LLC, Lake Forrest, CA) and Professor Jim Schwiegerling, aims to take simulated images, specifically blurred letter charts, and use them to estimate the visual acuity of the optical system used to blur the images. Key metrics used by the software and the algorithm therein were developed by the author. This software will be elucidated in Chapter 5, along with the metrics and algorithms it uses.

1.2 Contents Summary

This dissertation is organized as follows: Chapter 3 is a discussion of techniques used for generating blurred images. Here we will discuss convolution methods as well as Fourier methods. Next, Chapter 5 is a brief discussion of visual optics and metrics used therein. Then a presentation of work done by the author to estimate and predict visual acuity from simulated blurred images for: a monofocal eye model, a multifocal eye model, multifocal pseudophakic intra-ocular lenses (IOLs), and finally a comparison of various multifocal contact lenses. While Chapter 5 discuses quantitative metrics for assessing performance, Chapter 3 aims to qualitatively evaluate optical performance. This is accomplished by blurring "real world" scenes as they would be seen through first monofocal then multifocal optics. Simulated three dimensional scenes are generated with artifacts that are present in normal vision, i.e. blur varying with distance, regions of occlusion, and in the case of the presence of multifocal ophthalmics, multiple regions or distances in focus. Previous work by Barsky et al. have coined the term *vision realistic rendering* to describe this type of scene image generation.

CHAPTER 2

IMAGE PROCESSING

Images simulated as though they were taken through an optical system can provide insight into the performance of that optical system. In this chapter the methods used to generate simulated images are laid out. Generally, we take a Fourier approach with the assumptions that the optical system of interest can be classified as linear and shift-invariant.

2.1 Generating Simulated Images

From an image processing perspective, generating a simulated image for a given optical system can take the form of a convolution of an “object” (which is usually a two dimensional image to start with) and the optical system’s point spread function (PSF). That is to say, a two dimensional convolution operation of the object space irradiance distribution function, $o(x,y)$, and the point spread function, $PSF(x,y)$. Computationally, this convolution will be a discrete operation with both $o(x,y)$ and $PSF(x,y)$ being discrete, finite arrays. For small array sizes, this route can be shown to be a viable option. To proceed down this avenue, knowledge of the PSF is required. In a given circumstance, there can be a few ways to arrive at knowledge of the PSF. One common way is through an optical modeling software such as Zemax (Zemax LLC, Kirkland, WA) or CodeV (Synopsys Inc., Mountain View, CA). One can extract an array with discrete PSF values at each of the array locations, for a modeled optical system and a given object distance/field location. In this instance, knowledge of the PSF will be limited to values inside of the spatial extent of the array, x and y values. It is possible that some information will be thrown away due to the truncation of the PSF to a finite array or tails of the PSF can wrap around to the other side of the array causing errors.[8]. Consequently, adequate sampling and array sizes are needed to ensure fidelity in the blurred images.

Alternatively, the required information can be obtained from the wavefront error, $W(x,y)$, of the optical system from the software. This again will be a discrete array, but can be chosen to extend to cover the entirety of the exit pupil of the system. If desired, the wavefront error could be fit to some orthogonal polynomial set such that an arbitrary sampling could be achieved. The simulated image generation can instead be performed using the optical transfer function, rather than the point spread function. It turns out that the optical transfer function can be related to the wavefront error as follows. The pupil function, $P(x,y)$, can be written as

$$P(x,y) = T(x,y)\exp\left(-i\frac{2\pi}{\lambda}W(x,y)\right), \tag{2.1}$$

with $T(x,y)$ being the transmission function of the pupil containing both information of both the shape and transmission properties of the aperture. As an example, for a circular aperture with unit amplitude transmission and zero phase modulation, $T(x,y)$ will be a cylinder function (defined in Equation 2.3). Furthermore, the optical transfer function will completely contain the information about impulse response for the system, in a finite array. For the case of incoherent illumination, the optical transfer function (OTF) is given by the autocorrelation of the pupil function $P(x,y)$. In the special case of a circular aperture of unit transmission and no phase modulation, the OTF is given as

$$OTF(\xi,\eta) = \frac{2}{\pi}\left[\cos^{-1}(\rho) - \rho\sqrt{1-\rho^2}\right]\mathrm{cyl}\left(\frac{\rho}{2}\right) \tag{2.2}$$

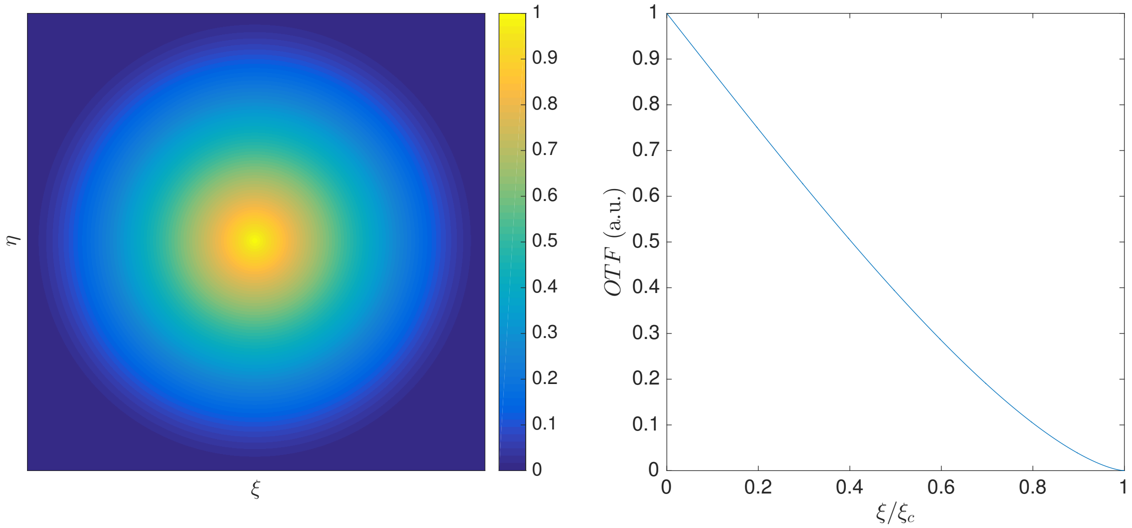

Figure 2.1: Optical Transfer Function for a circular aperture of unit transmission. Left: Two dimensional map of the on-axis OTF. Right: Cross section through OTF, from $\xi = 0$ to $\xi = \xi_c$, with ξ_c being the cutoff frequency i.e. where the OTF goes to zero.

with $\rho = \sqrt{\xi^2 + \eta^2}$ and the cylinder function defined as Gaskill does [9].

$$\text{cyl}\left(\frac{r}{d}\right) = \begin{cases} 1, & 0 \leqslant r < \frac{d}{2} \\ \frac{1}{2}, & r = \frac{d}{2} \\ 0, & r > \frac{d}{2} \end{cases} \tag{2.3}$$

The OTF is normalized to have a value of unity at the origin. This is essentially a statement of conservation of energy via the central ordinate theorem. The volume under the PSF is equal to the OTF value at the origin. With a more complicated pupil function, for example a different shape aperture or transmission variation within the pupil, the OTF will maintain its central value of unity at $\xi = \eta = 0$, yet will be reduced at other values of ξ, η. This reduction can cause decreased contrast for a given spatial frequency or even contrast reversals. The OTF may take on negative values, meaning there will be a contrast reversal due to a π phase shift. If the PSF is still a desired quantity, it may be calculated as the inverse Fourier transform of the OTF.

$$OTF(\xi,\eta) = \mathscr{F}\{PSF(x,y)\} \tag{2.4}$$

Although, calculating the PSF in this manner may still cause some loss of information since the finite, discrete sampling of the pupil function corresponds to the tails of the PSF. Figure 2.1 shows the optical transfer function for a incoherently illuminated circular aperture of unit transmission. The OTF will be rotationally symmetric for a rotationally symmetric aperture function and an on-axis object point. For off-axis points, the OTF will be hermitian.

2.1.1 Fourier Techniques

As noted in the previous section, once we have an array representing the PSF or the OTF, we can generate a simulated image via a two dimensional convolution of the object space irradiance function, $o(x,y)$, and the point spread function,

$$i(x,y) = o(mx,my) ** PSF(x,y), \tag{2.5}$$

resulting in the image $i(x,y)$, with m being the transverse magnification. Note, hereafter it will be implied that $m = 1$ when using $o(x,y)$. Here, we are using Gaskill's notation of the double asterisk to denote the two dimensional convolution operation. Computationally, a two dimensional convolution operation can be computationally expensive and therefore slow for large arrays. In many cases it is computationally advantageous to arrive at the image irradiance function by way of the convolution theorem which states that if $\mathscr{F}\{g(x,y)\} = G(\xi,\eta)$ and $\mathscr{F}\{h(x,y)\} = H(\xi,\eta)$ then

$$\mathscr{F}\left\{\iint_{-\infty}^{\infty} g(\xi,\eta)\, h(x-\xi,y-\eta)\, \mathrm{d}\xi \mathrm{d}\eta\right\} = G(\xi,\eta)\, H(\xi,\eta), \tag{2.6}$$

$$\begin{tikzcd}
 & P(x,y) \arrow[d, "|F.T.|^2" description] & \\
o(x,y) \arrow[r, "**" description] \arrow[d, "F.T." description] & PSF(x,y) \arrow[r, "=" description] \arrow[d, "F.T." description] & i(x,y) \\
O(\xi,\eta) \arrow[r, "\times" description] & OTF(\xi,\eta) \arrow[r, "=" description] & I(\xi,\eta) \arrow[u, "F.T.^{-1}" description]
\end{tikzcd}$$

Figure 2.2: Convolution Theorem. The image $i(x,y)$ can be found by the convolution of the object $o(x,y)$ and the point spread function $PSF(x,y)$. Conversely, one can multiple the object spectrum $O(\xi,\eta)$ and the optical transfer function $OTF(\xi,\eta)$ to find the image spectrum, then take the inverse Fourier transform to arrive at the image $i(x,y)$.

or more simply

$$\mathscr{F}\{g(x,y)**h(x,y)\} = G(\xi,\eta)H(\xi,\eta), \tag{2.7}$$

which is to say that performing a convolution in the space domain is equivalent to: the inverse Fourier transform of the product of the Fourier transform of each function. [10]. Computationally, this is a much less expensive proposition with the aid of such tools as the Fast Fourier Transform (FFT) algorithm. Multiplying large matrices together and two two-dimensional FFT operations is much faster than a two dimensional convolution operation for all but very small arrays. The convolution theorem method of arriving at the image irradiance distribution function as applied to the imaging problem is shown schematically in Figure 2.2. The diagram shows that one can perform a two dimensional convolution operation on the object $o(x,y)$ and point spread function $PSF(x,y)$ to get the image $i(x,y)$, while a completely equivalent path is to take the Fourier transform of the object to find the object spectrum, take the Fourier transform of the PSF to find the optical transfer function $OTF(\xi,\eta)$, or use the OTF directly since we have elaborated why using the OTF is superior. Then multiply the object spectrum, $O(\xi,\eta)$, and $OTF(\xi,\eta)$ to find the image spectrum $I(\xi,\eta)$, then inverse Fourier transform the image spectrum to find the image irradiance distribution $i(x,y)$.

2.2 Image scaling

In a later chapter it will be elucidated that we are interested in simulated images of letter charts, for example the Snellen letter chart. In this instance, it is important that the letters in the chart are scaled properly to the dimensions of the optical system being simulated. This section will lay out the necessary quantities for scaling the image (discrete array). We can consider our pupil function to be a cylinder function

$$P\left(x_i, y_j\right) = \mathrm{cyl}\left(\frac{r_{ij}}{d}\right), \tag{2.8}$$

with $r_{ij} = \sqrt{x_i^2 + y_j^2}$ in an array of width $2d$ and i, j denoting pixel or element numbers. We can note that the cylinder function is of width d, half that of the array. From this, the OTF is then the autocorrelation of the pupil function. In the Fourier method of simulated image generation outlined above, the OTF array will be multiplied by the object spectrum array, element wise. Therefore, the arrays must be of the same dimensionality. If we assume that our object array is $N \times N$, then our OTF array will also be $N \times N$. Further, the object spectrum array $O\left(\xi_i, \eta_j\right)$ will also be $N \times N$. Typically, N is a power of 2 since the fast Fourier transform is optimized for these values. The cutoff frequency of the OTF will be at the edge of the OTF array since the OTF will have non-zero values over a width of $2d$. As seen in Figure 2.3, we can geometrically derive both the cutoff frequency and thereby the width of the OTF. The autocorrelation operation will yield non-zero values when there is overlap between the two copies of the pupil functions that is non-zero. Therefore, in one dimension, we can see that when the pupil functions are just touching i.e. the autocorrelation and OTF will be nonzero, the centers of the pupils

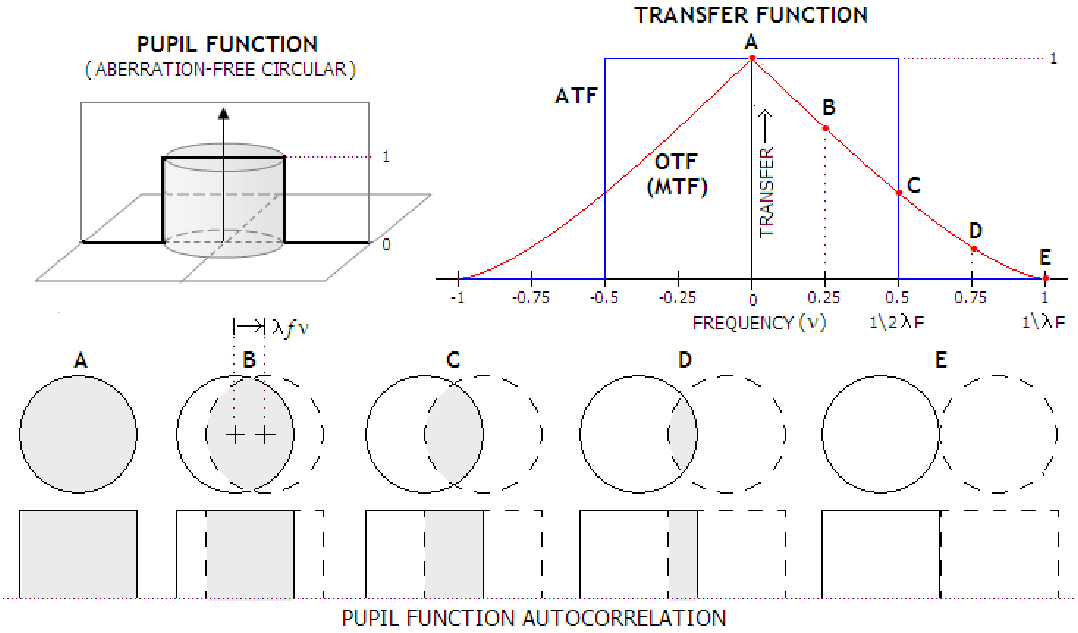

Figure 2.3: Autocorrelation of circular pupil, showing different directions one can derive the cutoff frequency. Image reproduced from Sacek .[2]

will be separated by $d = \lambda f \xi_{\text{cutoff}}$. The cutoff frequency will then be given by

$$\xi_{\text{cutoff}} = \frac{1}{\lambda f/\#} = \frac{d}{\lambda f}. \tag{2.9}$$

Here, λ is the wavelength and f is the focal length of the system. This can easily be extended to two dimensions to include variation in the η direction, then the Euclidean distance will be considered in the $\xi - \eta$ plane rather than just along the $\xi-$axis [11]. The units of ξ_{cutoff} will be that of the inverse of d. For ophthalmic applications it is often useful to work in angular frequency space. Then the cutoff frequency will be

$$\xi_{\text{cutoff}} = \frac{d}{\lambda} \frac{\text{cycles}}{\text{rad}}, \tag{2.10}$$

and the width of the OTF array will be $2d/\lambda$.

In PSF space, the width of 1 pixel or element in the array, $\Delta x = \left| x_{ij} - x_{i+1,j} \right|$, will be the reciprocal of the full width of the OTF array,

$$\Rightarrow \Delta x = \frac{\lambda}{2d}\text{rad}. \tag{2.11}$$

Often for ophthalmic applications, angular dimensions are scaled to minutes of arc. The reasoning behind this scaling of angular dimensions will be covered more in depth in Chapter 5, but for now it can be said that for ophthalmic applications it is desirable to scale angular dimensions to the nominal resolution limit of the human eye; namely, one minute of arc. Then, the size of a pixel in OTF space is

$$\Delta x = \left(\frac{\lambda}{2d}\text{rad}\right)\left(\frac{180^\circ}{\pi\text{rad}}\right)\left(\frac{60'}{1^\circ}\right) = \frac{10800}{\pi}\frac{1}{2}\frac{\lambda}{d}\text{arcmin}. \tag{2.12}$$

Finally, we can define the Snellen fraction S such that a 20/20 letter implies $S = 1$, and similarly, 20/40 implies $S = 1/2$. Although it is introduced here, the Snellen fraction will be covered more in depth in Chapter 5. The size of a letter in minutes of arc is

$$\alpha = \frac{5}{S}\text{arcmin}. \tag{2.13}$$

For example, a 20/20 letter will have an angular size of

$$\alpha_{20/20} = \frac{5}{S}\text{arcmin} = \frac{5}{1}\text{arcmin} = 5\text{arcmin}. \tag{2.14}$$

To find the extent of a given letter in terms of pixels, divide α by Δx,

$$n = \frac{\alpha}{\Delta x}. \tag{2.15}$$

In the code used for simulating blurred letter charts (in Chapter 5), d is dictated by the data. There, the data is measured wavefront data or profile data for contact lenses and intra-ocular lenses. In case, wavefront data d is given by the size of the sensor used to make the measurement (assuming unit magnification) and in the case of physical profile. Although the parameter is adjustable, for all simulations in this dissertation, $d = 5.1482\text{mm}$. Therefore, a 20/20 letter for these data should be

$$n_{20/20} = \frac{\alpha_{20/20}}{\Delta x} = 5\text{arcmin}\left(\frac{2\pi}{10800}\frac{d}{\lambda}\text{arcmin}\right)^{-1} \approxeq 19\text{pixels}. \tag{2.16}$$

CHAPTER 3

THREE DIMENSIONAL SCENE SIMULATION

As discussed in the previous chapter, simulated images can provide insight into optical system performance. This chapter will build on the previous, and extend the ideology to simulating images of objects at different distances from the optical system. For a given optical system, if the PSF is assumed to be spatially invariant, then the formalism developed previously can be used to obtain a simulated image. If the PSF varies across the field of view, multiple field points are sampled and interpolated to give the PSF for any point in the field of view. Simulated images can then be assembled with blurring from each field point's respective PSF. These techniques assume a two dimensional planar object. We will extend this image simulation technique to include three dimensional scenes. The PSF will now depend on the field point location as well as object distance. The formalism needed for this extension will be discussed as well as approximation that can be implemented to reduce computation time.

Raytracing programs, such as Zemax, have image simulation capabilities. Using the example of Zemax, one could use the image simulation tool in a sequential or non-sequential model. This image simulation tool can generate a simulated image by sampling the PSF over the field. Figure 3.1 shows an example PSF grid from a sequential Zemax model. In a sequential image simulation, Zemax will sample the PSF on a grid, and interpolate at each pixel between sample locations for each pixel in the input image. Then each PSF is convolved with corresponding pixel of the input image to produce the output image[12]. Here, while each operation is a convolution, we cannot write that the operation as a whole is a convolution, since the PSF varies with location in the field. Now,

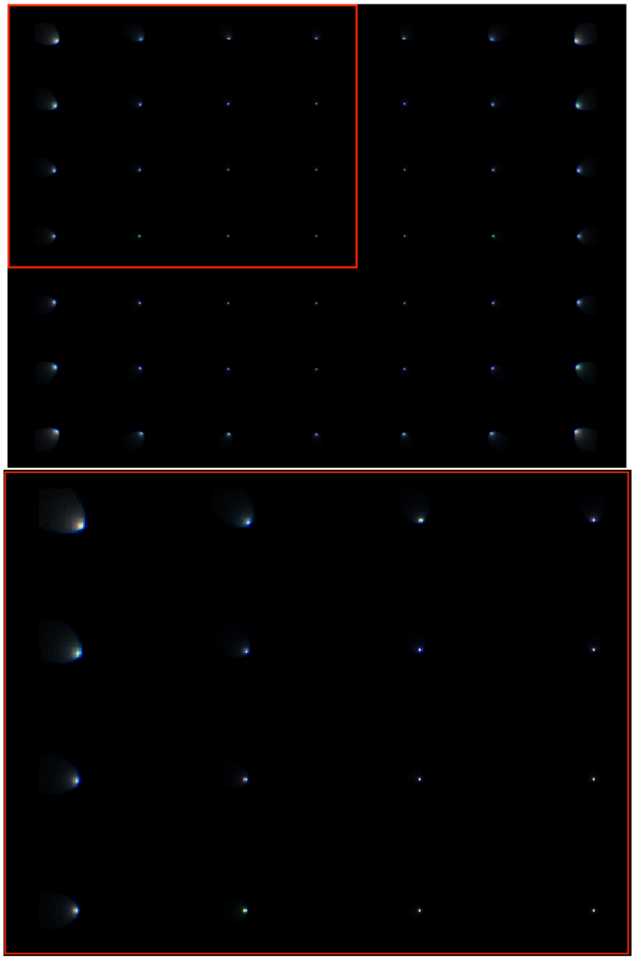

Figure 3.1: Sequential image simulation PSF grid in Zemax. Top shows the PSF grid sampled over the field of view. Bottom is the red inset in the top image, magnified upper left quadrant. As the field increases, it is quite easy to see that the PSF degrades; at the edges of the field coma can be readily seen.


(a) (b)

Figure 3.2: Input and output images from sequential Zemax image simulation tool.

mathematically we can write that the image is

$$i(x,y) = \int h\left(x,y;x',y'\right) o(x,y) \, \mathrm{d}x' \mathrm{d}y', \tag{3.1}$$

with $h(x,y;x',y')$ being the PSF at each location of the input image or "object" $o(x,y)$. Figure 3.2 shows the input and output images for this PSF grid generated for a plano-convex singlet. Figures 3.2a and 3.2b can be compared and the barrel distortion and blurring toward the edges are very apparent. In using a non-sequential model, the number of pixels in the input image and detector are specified, as well as how many rays to trace per pixel. This is the discrete corollary to discretizing the object into a summation of point sources, with the "point" sources now having the extent of the pixel in the input image. Then Zemax will trace the specified number of rays from each pixel. Since this is a non-sequential model, some, all, or even none of these rays will make it into the entrance pupil of the optical system being simulated and make it to the detector plane. Consequently, unless hundreds of millions or billions of rays are traced the output image tends to be "grainy" due to a limited number of ray intersections with the detector. Such a high number of rays being traced in a non-sequential manner necessarily has an increased computation time. Here, we will look at methods to work around these limitations.

Realistic scene simulation has been discussed in the literature recently and has applications in computer vision, augmented and virtual reality, and gaming [13, 14]. Grover *et al.* presented a method for simulating multi-camera systems using simulated images to compare camera-scene geometries, as well as image processing algorithms. The simplifying assumption that all objects in the scene are at a fixed, unique distance allows the computation to be straightforward. In actuality, the PSF will vary for every object distance, contributing to defocus for a fixed single focus optical system, and field angle. This object-point distance and field location variation of the PSF has been dubbed the Object Space Point Spread Function (OSPSF) [14] . Sampling the PSF at upwards of a million or more locations, i.e. at every pixel location on the optical system sensor, and integrating them into a final image is computationally challenging. We will therefore look at methods to work around this avenue.

Another issue that arises when simulating three dimensional objects and scenes is occlusion. Occlusion is the obstruction of part of the distant scene by a near by object. An example of this would be the region of the computer screen that is blocked by the cell phone in the foreground of Figure 3.3. Our goal here will be to enable the simulation of multi-depth scenes such as the office of Figure 3.3 as though it were seen through a multifocal optical system. This chapter will elaborate on the software, methods, and verification used for this simulation while Chapters 4 and 5 will go into more detail on multifocal optical systems, their applications, and justify an interest in them.

We will start with a simplification of a complex scene like that of Figure 3.3 in order to make some headway. Here, our proposed method for dealing with occlusion will be elaborated along with the simplification that we will be generating a full simulated scene and compare the image to that of a photographed scene with a DLSR camera.

Figure 3.3: Office scene showing occlusion. Image taken with a very large depth of field such that everything in the scene from the near plane of the cell phone to the distance plane of the outside buildings.

3.0.1 Experimental Setup

We have chosen a relatively simple experimental setup as a starting point for developing the necessary algorithms and code. Our 3D scene consists of two target letter E's at two distances from a consumer DLSR camera, specifically a Canon EOS Rebel XSi with a Canon EF-S $f = 18-55$mm, $f/3.5-5.6$ lens, and a 4272×2448 pixel sensor. Our image set used for comparison with simulation was taken at $f = 44.0\text{mm}, f/5.7$. The distance target was placed a distance $d_{\text{dist}} = 91.44$cm from the front surface of the camera lens, and the near target was placed a distance $d_{\text{near}} = 45.72\text{cm} = d_{\text{dist}}/2$ from the front surface of the camera lens. Images of the targets were taken with the camera focused on the near target, midway between the targets ($d_{\text{mid}} = 68.65$cm), and the distance target. Next, the PSF of the camera was probed with a white-light source and 50μm pinhole to give a point source. The point source was first placed at the near target distance d_{near} and images were taken with the camera focused at the three planes of investigation. This was then repeated with the point source at the distance target location d_{dist}. Figure 3.4 shows the experimental setup. The target E's are scaled such that their image is the same size, i.e the distance target E is a 2X scaling of the near target E.

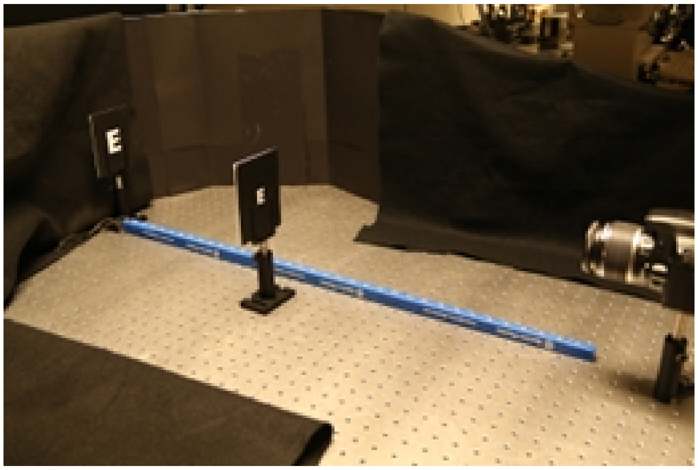

Figure 3.4: Experimental Setup. Canon DLSR camera at right, target E's placed approximately 1m and 0.5m from the front surface of the camera lens. Background is darkened as much as possible with black felt and black boards.

3.1 Simulation of 3D Scene

A MATLAB script was developed to simulate images of the object scene. Since our test scene is nominally black and white, all PSF and scene images were reduced to a 2D array by element-wise averaging of RGB color channels. Given that we are dealing with arrays with greater than 10M elements, convolution in this space is both computationally expensive and time consuming. Therefore, we generate a simulated target E by way of the convolution theorem, i.e. multiplying the Fourier transforms of PSF and binary E arrays, then taking the Inverse Fourier transform of the product as discussed in Chapter 2 [9]. This allows for a significant reduction in computation time and resources. Target Es for simulation are a binary matrix, of the same dimension as images generated by the camera, with regions inside of the E being unity and regions outside being zero.

Each blurred E in the simulated image is generated by convolving the binary E matrix with the PSF image corresponding to the proper distance and focus. As Figure 3.5a shows, the left (near target) E is generated by convolving the binary E in Figure 3.5b with the near target PSF at near focus, shown in Figure 3.5c. Similarly, the right (distance target) E is generated by convolution with the distance target PSF at near focus shown in Figure 3.5d. In order to match irradiance, or saturation, values within each E and the resulting blur, we scale the simulation image to have a maximum value as determined by a sample within the region of the near target E in the actual image. Our camera's image sensor displayed a significant amount of noise at such low light levels that were used in our experiment. To rectify this, outside of a small region around the PSF the values within the image were decimated to zero. With a newer, or higher grade digital sensor, this step in processing may not be needed.

For example, in Figure 3.7 we have a comparison of the actual image at near focus and the simulated image. Here, in the simulated image, the left (near target) E was generated by convolving the binary E matrix with the image of the point source at the near target location with the camera focused at the near target location. The right (distance target) E was generated by convolving the binary E matrix with the image of the point source at the distance target location and the camera focused at the near target location.

3.1.1 Occlusion of Targets

The problem of occlusion has been discussed with regard to computer vision [15]. In our real scene, the near target slightly overlays the distance target which is a commonplace situation for real scenes of interesting complexity. To simulate this, the blur from the distance target must be blocked by the near target. In the region of the near target, only blur from this target should be present. Outside the region of the near target, we expect an overlay of blur from both targets. To deal with the occlusion of the distance target by the near target in our simulation, we take a region of the blurred distance target image,

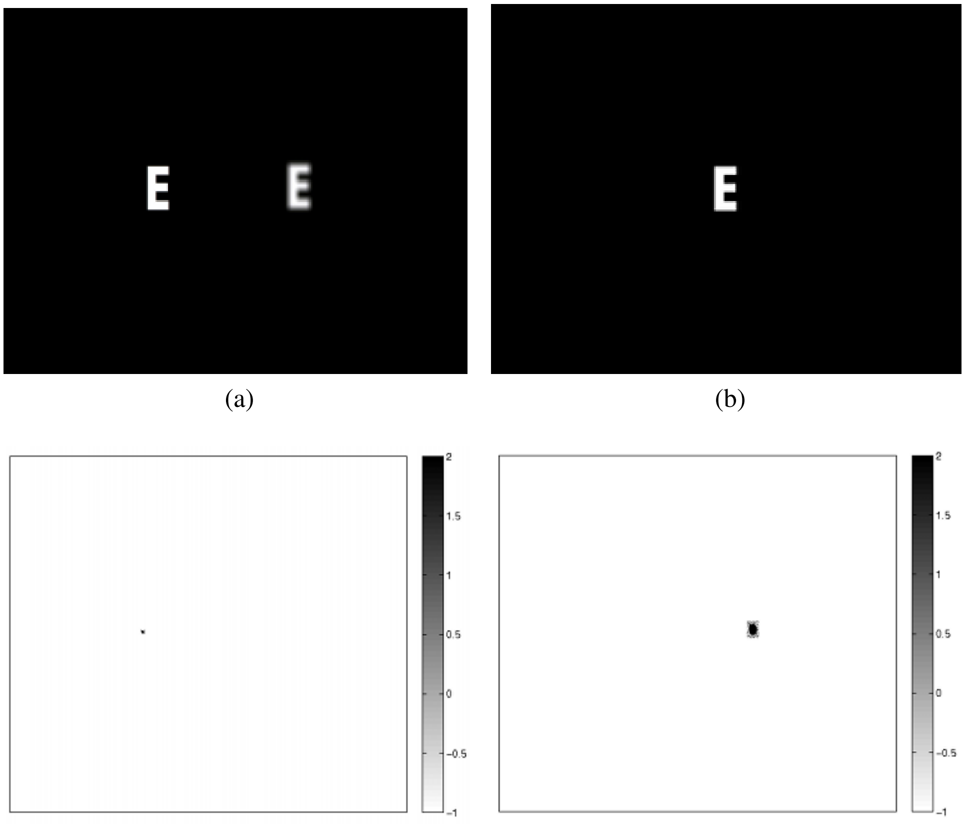

(a) (b)

(c) (d)

Figure 3.5: Elements used to generate a simulated target E. (a) Simulated blurred E's. Left E is at near target distance, where the camera is focused, and right E is at distance target location, (b) binary E, (c) near target PSF at near focus, (d) distance target PSF at near focus. Parts (c) and (d) are displayed on a truncated log-scale (inverse grayscale) colormap showing three decades to increase visibility to the reader.

where the near target will fall once the near are distance target images are added, and set the values in this region to zero making a black rectangular region. Then, we add the blurred near target image to the blurred distance target image (with occlusion region decimated). This achieves our goal, since we are left with a region where there is only blurring from the near target and elsewhere we have blurring from both near and distance target. Pictorially, this is shown in Figure 3.6.

3.2 Results

Figures 3.7 - 3.12 show a comparison of our simulation compared to actual images of our two-plane scene. Visually they are nearly indistinguishable. Two issues that can be seen in Figures 3.7, 3.9, 3.11 are vertical offset of targets in the actual image is not present in the simulated image, and the aspect ratio of the target E's in the actual image is different than that of the simulated target E's. The offset of target E's in the actual images is not present in the simulated images because the point source was kept at the same height for all PSF images. Since the convolution process with the PSF will locate the blurred E in the simulated image, both the near target and distance target E's are at the same height. The binary E used for simulation has a slightly different aspect ratio than that used in our experimental setup. Future work will deal with both of these issues since they are quite easily solved.

3.2.1 Simple scene geometry

3.2.1.1 Two-plane object scene

In Figures 3.8, 3.10, 3.12 blue lines represent a vertical slice through our actual image of the scene, near target on the left and distance target on the right with red lines being a vertical slice at the same location in our simulated image. The registration issue of the near target with simulated near target is easily identified. Non-optimal scene illumination

(a) Distance PSF

(b) Distance target E

(c) Near PSF

(d) Near target E

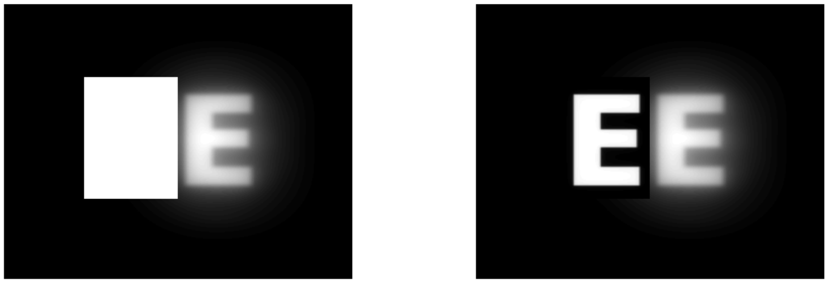

(e) Distance target E with occlusion region shown as white rectangle.

(f) Combined image

Figure 3.6: Method for simulating occlusion. Binary E shown in Figure 3.5b and distance PSF (b) are convolved to give the distance target E (c), while Figure 3.5b and near PSF (d) are convolved to give the near target E (d). In (f), the white rectangular region is set to zero, giving the region that is blocked by the near target E. Figures (e) and (f) are combined to give (g), the total image.

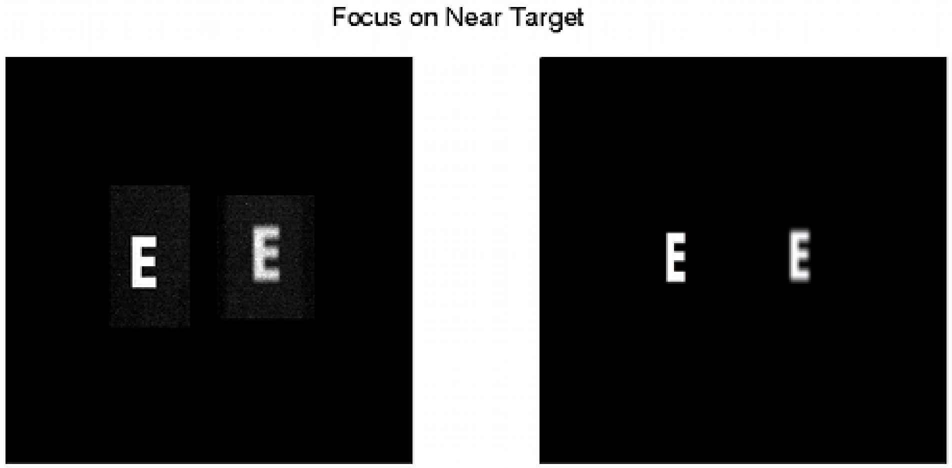

Figure 3.7: Left: Photograph of 3D scene with camera focused on near target. Right: Simulated image

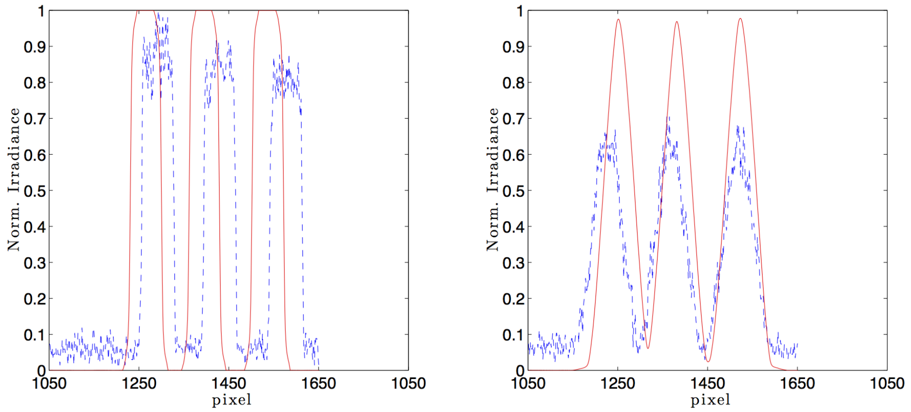

Figure 3.8: Comparison at near focus. Left: Vertical slice through near target E, blue-dashed line is from actual image and red line is from simulation. Right: Slice through distance target E, blue-dashed line is from actual image and red line is from simulation.

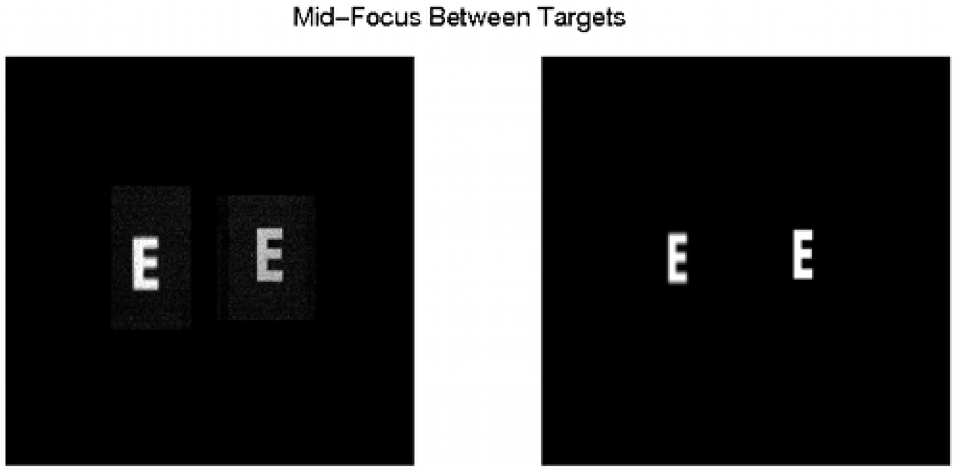

Figure 3.9: Left: Photograph of 3D scene with camera focused midway between the near target and distance target. Right: Simulated image.

can be seen in the slices of the distant target Es having a maximum normalized value of about 0.6.

As discussed, registration between actual scene image and simulated image can be overcome with greater attention to detail, likewise with scene illumination.

3.2.1.2 Three-plane object scene

Next, we can extend these techniques to a more complicated scene geometry, with the goal of simulating something with at least three regions of distance. Similar to the previous section, we have E targets at different distances. In Figures 3.13,3.14, and 3.15 we see a simulation generated image on the right alongside an actual image of the three plane test scene on the left. Figure 3.13 shows images taken and generated for the optical system focused at the near target plane. The reader should take note of the sharp edge of the near E target as well as the increasing amount of blur from the mid target plane to the distance plane. Further, the reader may notice a discrepancy in the grayscale levels between the actual image and the simulation generated image, this section and these results are to

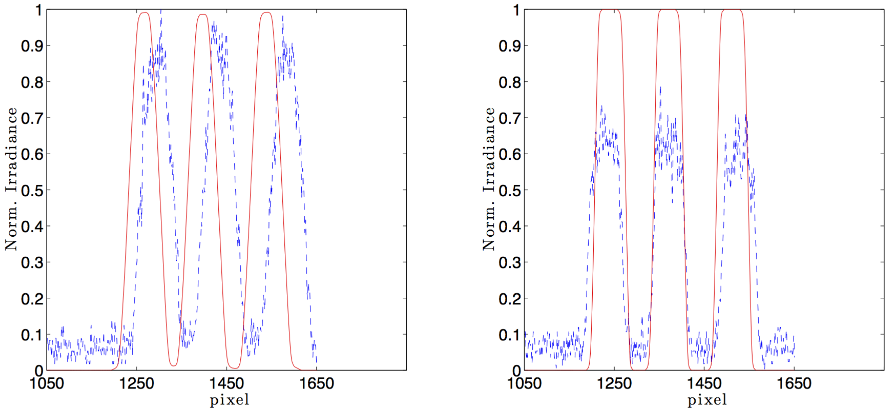

Figure 3.10: Comparison at mid-focus. Left: Vertical slice through near target E, blue-dashed line is from actual image and red line is from simulation. Right: Slice through distance target E, blue-dashed line is from actual image and red line is from simulation.

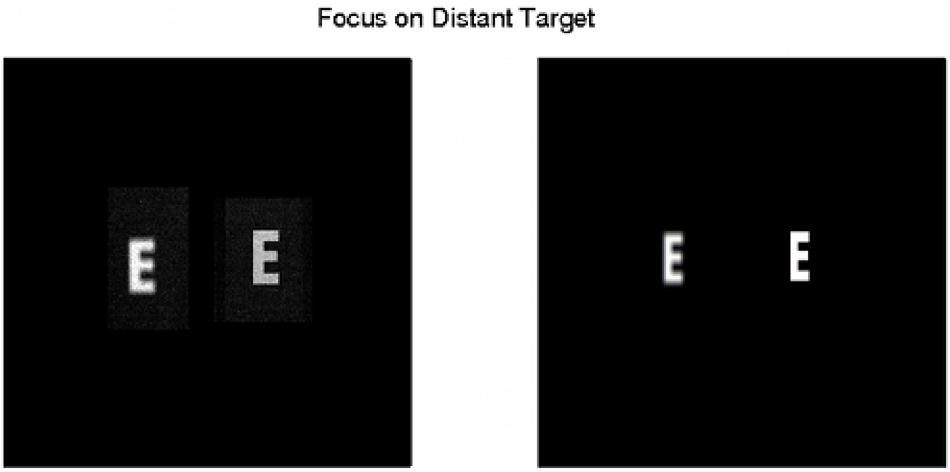

Figure 3.11: Left: Photograph of 3D scene with camera focused on distance target. Right: Simulated image.

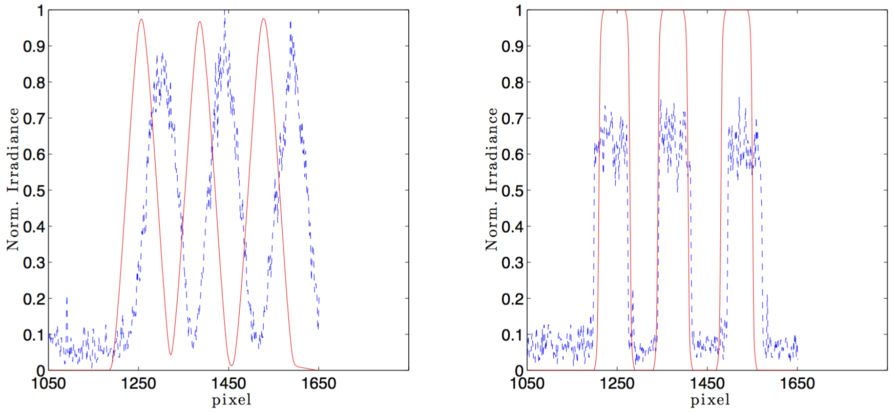

Figure 3.12: Comparison at distance focus. Left: Vertical slice through near target E, blue-dashed line is from actual image and red line is from simulation. Right: Slice through distance target E, blue-dashed line is from actual image and red line is from simulation.

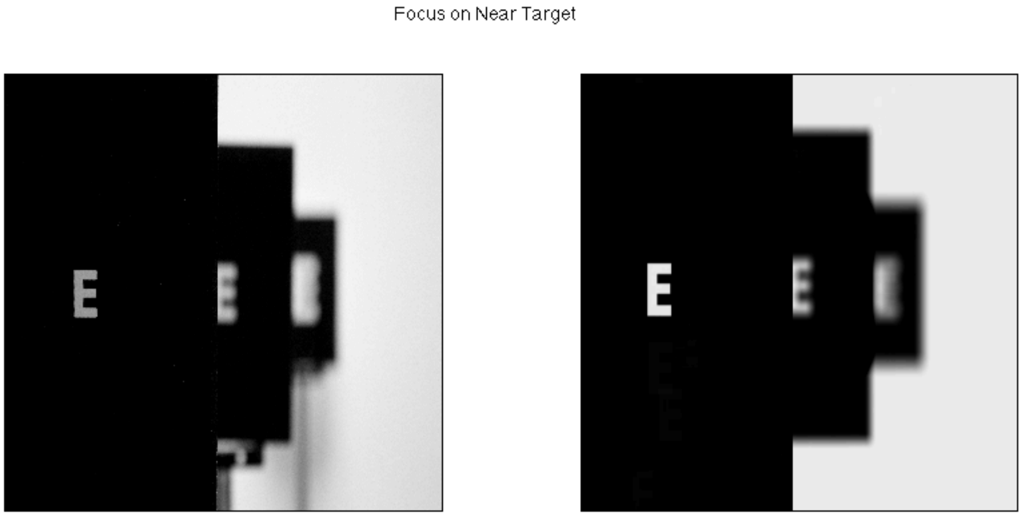

Figure 3.13: Three-plane scene simulation with camera focus at the near plane. Left: actual photo from camera. Right: simulation generated scene. Note that the right edge of the near target has a sharp edge with the distance target having more blur than the mid target.

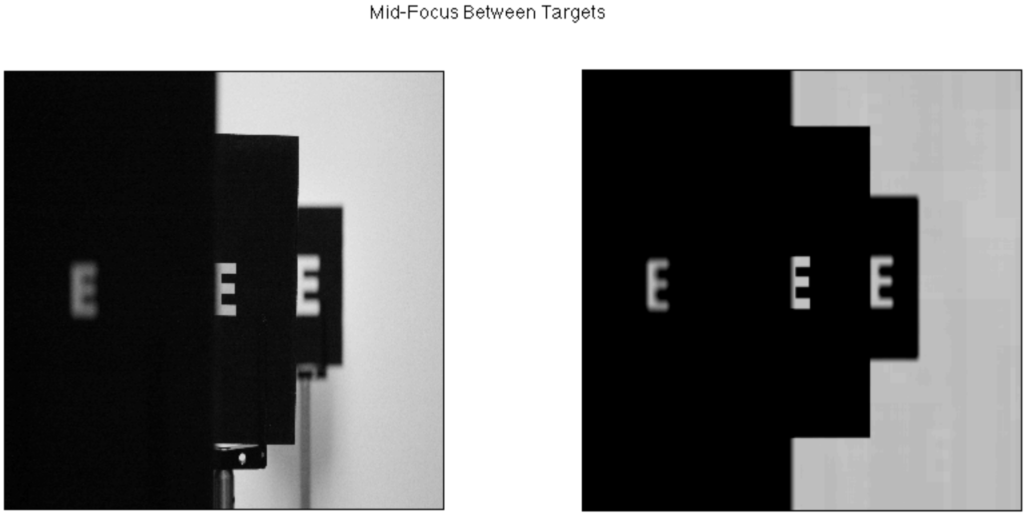

Figure 3.14: Three-plane scene simulation with camera focus at the mid plane. Left: actual photo from camera. Right: simulation generated scene. Note the sharp edges of the mid target, with different amounts of blur between the near and distance target planes.

demonstrate the ability to model a more complicated scene with three discrete planes and target occlusion. Figure 3.14 again shows an actual scene image taken with the DSLR described above on the left, and a simulation generated image on the right, both for the optical system focused at the mid target distance. Here the reader should take note of the sharp edges on the mid target and differing levels of blur at the near and distance planes. Figure 3.15 shows the actual scene image on the left with the camera focused at the distance target plane and the simulation generated image on the right. Note the sharp edges of the distance target and increasing blur as targets decrease their distance to the camera, or equivalently, increase their distance from the plane of focus (distance target plane).

3.2.1.3 Real scene simulation

Graphical rendering, especially with the onset of a mainstream paradigm of virtual and augmented reality, is a field that may benefit greatly from realistic scene image simula-

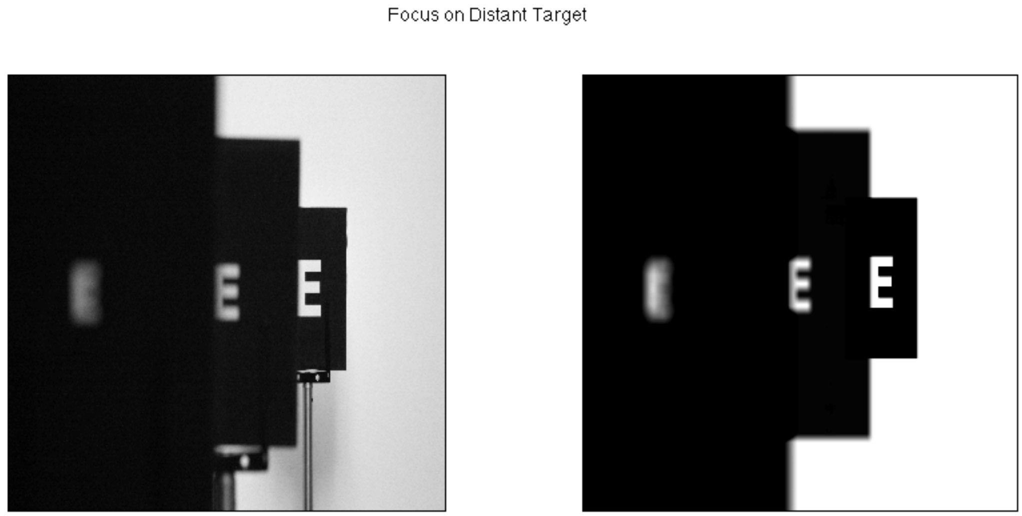
Focus on Distant Target

Figure 3.15: Three-plane scene simulation with camera focus at the distance plane. Left: actual photo from camera. Right: simulation generated scene. Note the sharp edges of the distance target as well as the greater blur in the near plane than that of the mid plane. The grayscale difference between left and right images is not important here as we are demonstrating a method for occlusion and blurring of different planes with their respective PSFs.

tion. Building on the work of the previous sections, we will show here the techniques applied to the simulation of a real scene image. Occlusion effects are paramount in this context as it is one of the difficulties as well as an important component of a realistic simulated image. Barsky *et al.* have proposed an algorithm and methods for addressing issues that may arise due to occlusion and discretization effects [16]. Here, they refer to the discretization of scene depths. Similar to our method, they use a chop-blur-combine method for blurring different regions of depth. Yet they have proposed two methods for identifying objects that may span multiple depth regions. One method is to find adjacent pixel differences in the depth maps, while the other is to use a Canny edge detection algorithm. Previously, Barsky *et al.* had proposed a method for identifying or approximating pixel color information based on ray intersections in the image plane and different object planes [17, 18]. Combining these ray intersections with object identification, using either

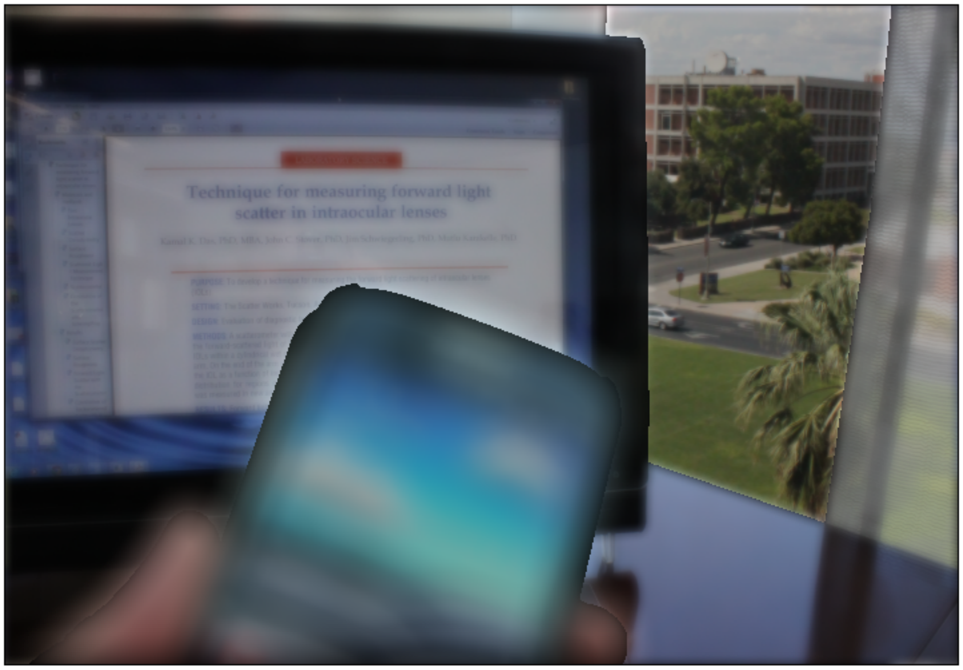

Figure 3.16: Occlusion effects. Black boarders can be seen around differing regions of depth, i.e. the near ground cell phone, mid-ground computer screen, and distance outdoors.

method, greatly reduces the edge effects seen without these considerations. Occlusion effects can be seen as the black boarders around the near-ground cell phone, and computer screen in the mid-ground in Figure 3.16. These edge effects are a byproduct of the method initially, albeit naively, for dissecting the original image, blurring each depth region, and recombining.

Our first method was to (for the example given in Figure 3.16 i.e. three planes of depth):

1. Identify regions of a given depth,
2. Apply a mask to the original image, unity in the region of interest and zero elsewhere,
3. Save masked image for this depth,

4. Repeat steps 1-4 for other depths.

Next, once a masked image has been generated for each scene depth (e.g. near-cell phone, mid-computer/curtains/desk, distance-outside scene) each depth can be blurred as outlined in Chapter 2 with a PSF corresponding to that depth for a given optical system and focus. This of course makes the assumption that the PSF is spatially invariant within each of the sub-regions, but changes from region to region. The edge effect shown in Figure 3.16 being black boarders at edges of each depth region arise from the masking and blurring steps. Masked images can be seen in Figures 3.17a - 3.17c. Since during the convolution process, the PSF will be "dragged" across the image, and overlap summed and assigned to that pixel location, it can be understood that edges will be darker (more black) than expected, as part of the PSF be multiplied by zero.

Another method we investigated for generating these simulated real-scene images with occlusion and deal with the roll off effect caused by black masked regions was to include a boarder around the masked region with a non-zero value. Specifically, the boarder region is set to be the half-width of the PSF for that depth. The pixel value within each boarder region is found from the mean pixel value, for each color channel, within the boarder region of the original image. While this method reduces the roll off effect, it doest not address the issue fully. Further, there are bright halos created at the boarder regions, due tho the summation of sum-images where both images contribute to that area. In Figure 3.18 the intermediate steps for this method are shown. Figure 3.19 shows the result of this method. Note the halos around the cell phone and hand in the near plane, and extending into the window from the mid plane of the computer and desk.

3.2.1.4 Alpha Blending

A technique called Alpha Blending is used to achieve proper transparency and occlusion in regions of blur. White regions are opaque to the background ($\alpha = 1$), while black

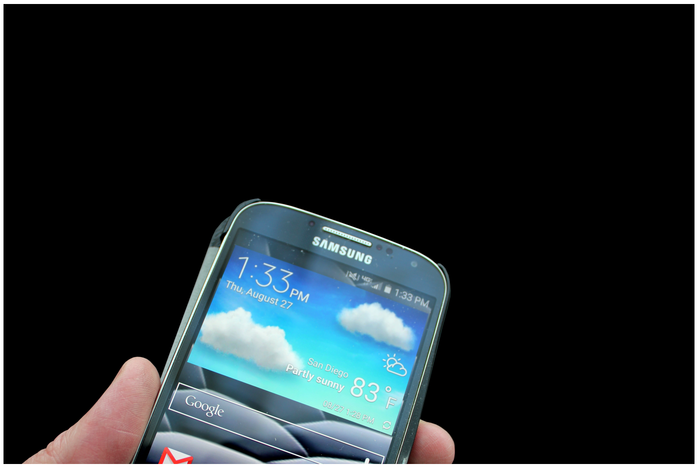

(a) Masked near plane - cell phone

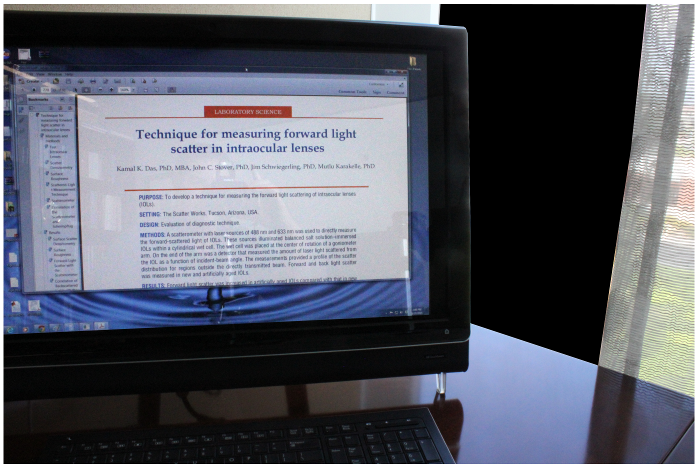

(b) Masked mid plane - computer scree/desk/curtains

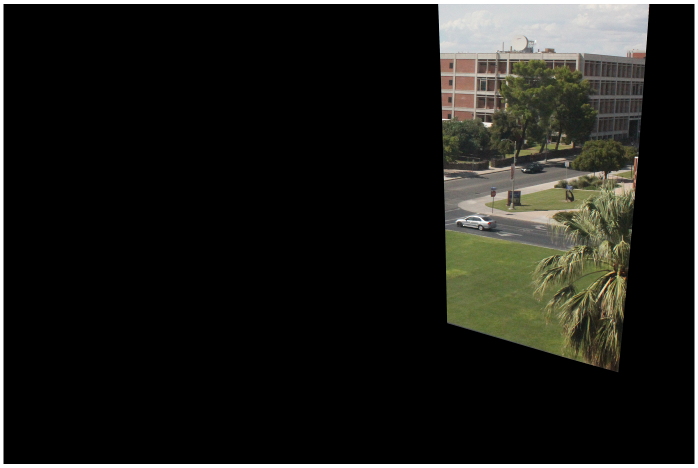

(c) Masked distance plane - outside

Figure 3.17: Masked images showing a source of darkened edges in the recompiled image.

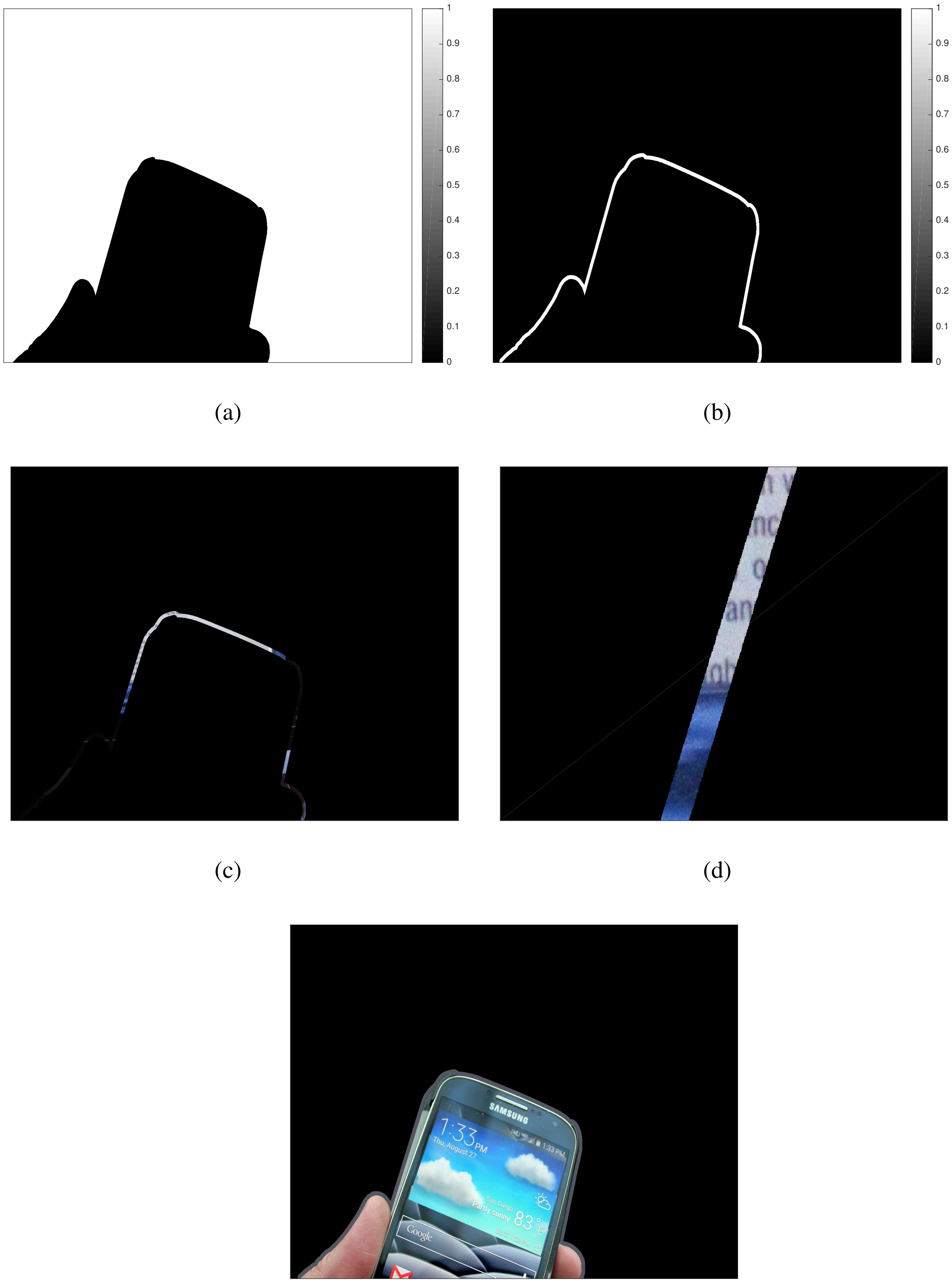

(a) (b)

(c) (d)

(e)

Figure 3.18: Boarder method.

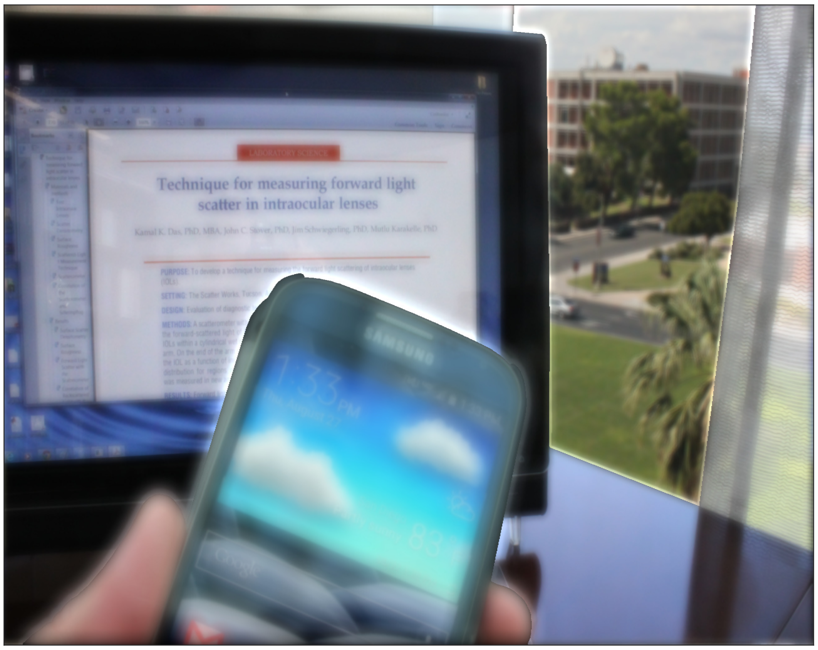

Figure 3.19: Boarder method. Average pixel value in each color channel is averaged and assigned to a boarder region of each mask to reduce the edge roll off effect caused by masks with black background. Note the bright halos around the hand and phone in the near plane, and extending into the outdoor area from the computer and desk in the mid plane. Generated with a multifocal contact lens for presbyopia (DACP high add).

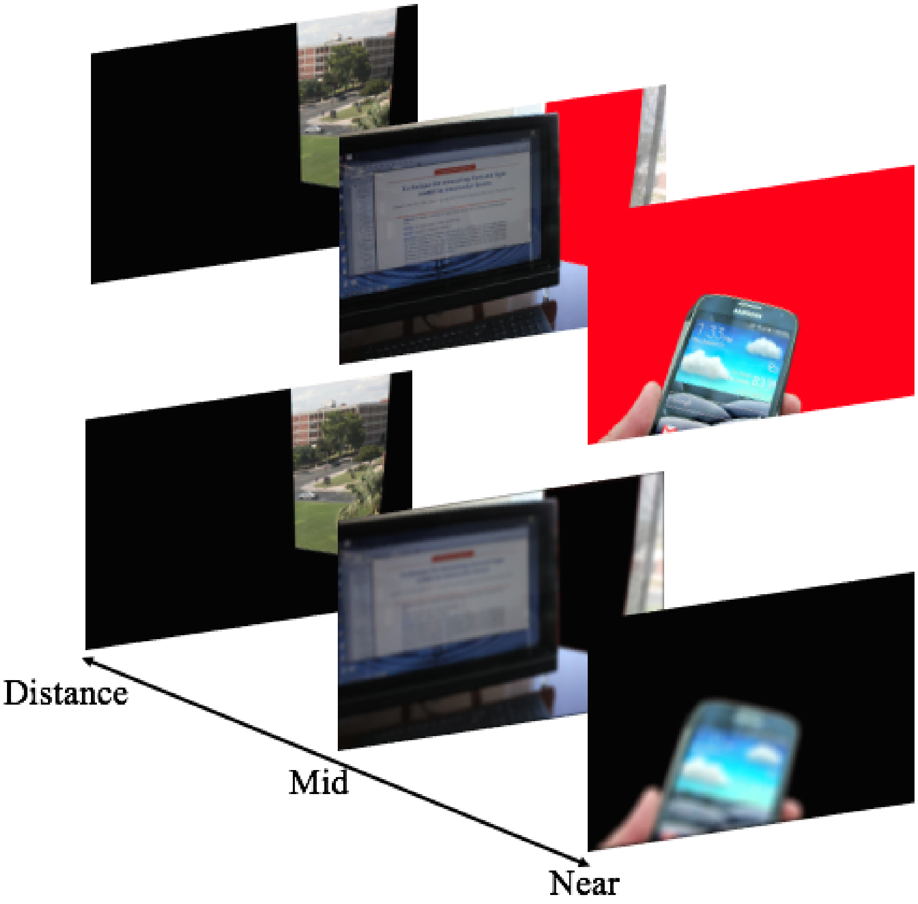

Figure 3.20: Sub-images Top: Sub images decomposed from original as a function of depth from viewer. The left image is the most distant and the planes become progressively nearer moving to the right. Distance portion of the image is what can be seen through the window. Mid-range portion of the image consists of the computer, desk, and curtains. Near portion of the image is the cell phone and hand. Bottom: Shows blurred distance, mid, and near sub-images ready for recombination.

regions are fully transparent to the background $(\alpha = 0)$. The edges of the mask take on a value between zero and unity. This creates the required occlusion and transparency effects. This creates the occlusion and transparency needed. The final composite image is combined using alpha blending with:

$$\text{Composite} = \alpha(\text{foreground}) + (1-\alpha)\,(\text{background}). \tag{3.2}$$

Figure 3.20 shows the masks that are used to recombine the images post-blurring. The structure for this technique is as follows:

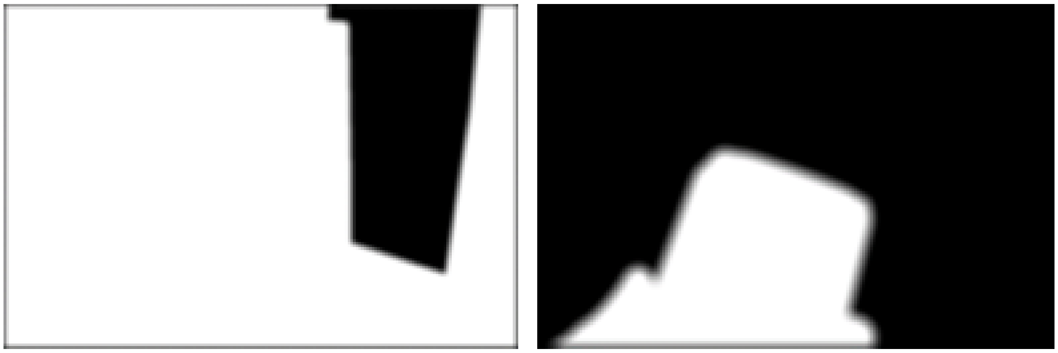

Figure 3.21: Alpha Channels Left: Shows the Alpha Channel mask used to blend the blurred distance and mid-plane images. Right: Shows the Alpha Channel mask used to combine the near plane with the mid and distance planes.

1. Decompose scene image by depth into sub-images,
2. Generate PSFs for each depth by adding defocus to wavefront error,
3. Blur each sub-image with corresponding PSF Blur each mask with corresponding depth's PSF,
4. Recombine sub-images using Alpha Blending and masks.

In Figure 3.21, the blurred masks are shown. Black represents a value of $\alpha = 0$ with white regions being $\alpha = 1$. Grayscale regions take on a value between zero and unity according to the grascale value. This technique gives realistic scene images with proper occlusion effects and color blending at edges.

3.2.1.5 Results using ophthalmic appliances

Using the alpha blending technique to blur planes and their respective masks, along with the linear combination of subimages allows for the generation of real scene images to compare different ophthalmic appliances. Chapter 4 will go into more detail on ophthalmic appliances and their relative differences, but here we will show the results for real scene simulation through a variety of lenses.

Figure 3 shows the simulation results for a variety of visual situations. For all simulations a 4 mm pupil size and no residual accommodation was assumed. Figure 3a shows a distance corrected presbyope with no residual accommodation. The outside scene is clear, but intermediate and near planes are blurred. Figure 3b shows the effect of putting a +2D pair of readers on this presbyope. The cell phone is now clear, but the intermediate and distance planes are blurred. Figure 3c simulates monovision. Here, the two previous scenes were averaged to simulate the superposition of the binocular images. The intermediate plane remains blurred in this scene. The distance and near planes are functional, but have reduced contrast due to the out-of-focus component overlapping the in-focus component. Figure 3d is a simulation for a aspheric progressive center near multifocal lens (Type I). Here, the sphere has been optimized to provide good vision for all three distances. Each range is clear with some slight loss in contrast for the cell phone image. Figure 3f shows a second example of aspheric progressive center near multifocal (Type II). Here, the lens relies solely on spherical aberration to provide the depth of focus in the scene. The distance and intermediate planes are in focus, but the near plane is degraded when compared to the Type I aspheric progressive lens. Finally, Figure 3e is a simulation of a ring type multifocal lens. Here the lens is a center distance design with a +2D add in a 1 mm wide ring with an inner diameter of 2 mm. The distance and near planes in this simulation are clear, but the intermediate plane is blurred.

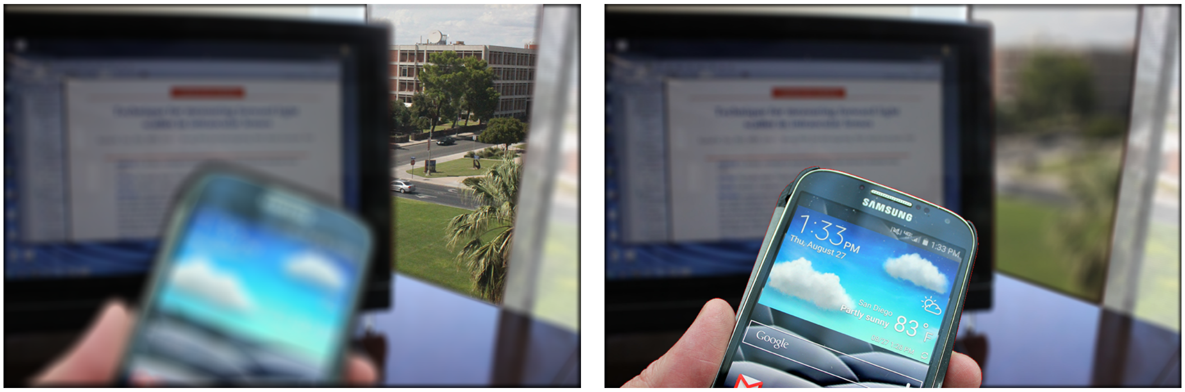

(a) Distance corrected presbyopia (b) Near vision correction

(c) Monovision (d) Ring type bifocal

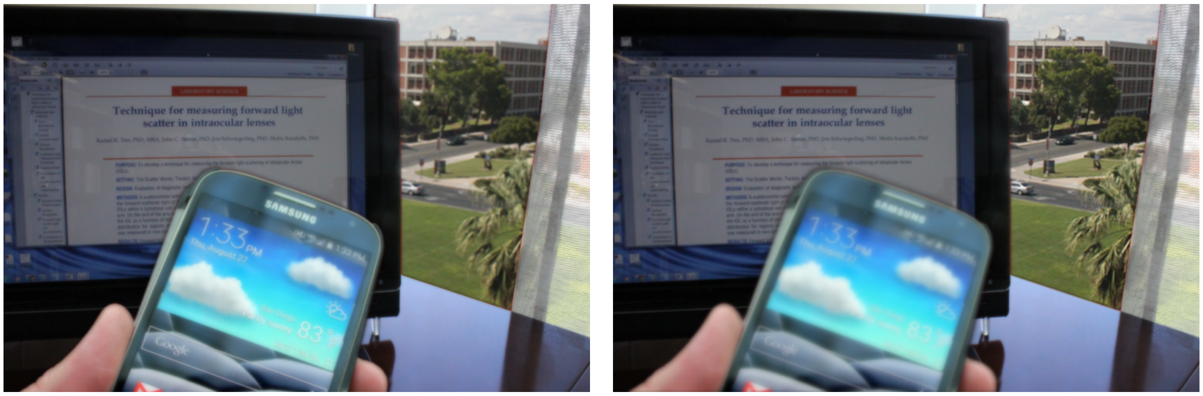

(e) Aspheric center-near design 1 (f) Aspheric center-near design 2

Figure 3.22: Recombined images for a variety of vision modalities including a range of designs multifocal contact lenses. (a) Distance-corrected presbyopia (b) Near vision correction. (c) Monovision (d) Aspheric center near +2.0D add multifocal Type I. (e) Aspheric center near +2.0D add multifocal Type II. (f) Ring-type design +2.0D multifocal contact lens.

CHAPTER 4

PRESBYOPIA AND ITS TREATMENT

4.1 Presbyopia

As discussed in Chapter 1, presbyopia is a condition that describes the progressively diminished ability to accommodate and focus on near objects. The diminished ability to accommodate is due to decreased elasticity in the crystalline lens. Loss of accommodative amplitude occurs throughout ones life until about an age of 52 years, where it is diminished to zero [19]. It is at this age or possibly sooner, depending on the refractive errors present in the eye, when the near point of the eye extends farther than an arm's length. Once diagnosed, it is readily treated with a number of methods. It is estimated that by year 2020, the global prevalence of presbyopia will be 1.4 billion cases [20].

4.1.1 Treatment of Presbyopia

Common treatment modalities for presbyopia are reading spectacles, bifocal spectacles, progressive addition lenses, and multifocal contact lenses. Reading spectacles are usually worn solely during reading and removed for tasks requiring distance vision or low on the bridge of the nose such that a wearer may look through them during a downward gaze to read. This may be the simplest solution, albeit cumbersome. Bifocal spectacles combine distance vision corrective lenses with near vision corrective lenses into a single pair of spectacles. There are many ways to achieve this combination, with the earliest method being to simply cut each lens in half horizontally and mount them in the same frame. More sophisticated and modern methods include having an inset portion of the distance vision corrective lens with s different material and index of refraction. Progressive addition lenses are a freeform, non-rotationally symmetric shape that had s continuous curvature change from the top portion of the lens to the bottom portion of the lens. There are pros and cons to each one of these modalities, but the important distinction is that they are all gaze-selective devices, meaning that the eye rotates to align its gaze through a different porition of the lens to select a different power correction. We do not include these modalities into our simulations.

4.1.1.1 ReVision Optics Raindrop Corneal Inlay

There is another class of devices that are not gaze-selective. Some of the presbyopic corrective modalities in this category that we will discuss are multifocal contact lenses, and the ReVision Optics Raindrop Corneal Inlay. The Raindrop Corneal Inlay, shown in Figure 4.1 being placed under an intra-stromal flap, is a device that induces the cornea to be a multifocal element. One method used to implant the device is to create a thin partial slice in the cornea, specifically in the stromal layer, to create a corneal flap. The Raindrop is then placed on the cornea and the flap is replaced. With the Raindrop device now lodged intra-corneally, the central part of the cornea will have a larger curvature and therefore more optical power while the annular region not affected by the extent of the inlay will remain as it was before the procedure, contributing to distance vision.

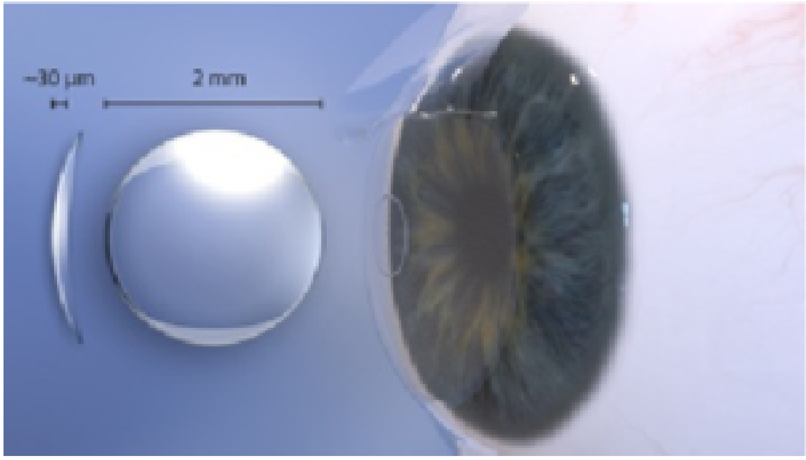

Figure 4.1: Image courtesy of ReVision Optics. ReVision Optics Raindrop Corneal Inlay, here shown being placed under and intra-stromal flap. The Raindrop is a hydrogel disk 2mm in diameter and about 30µm in thickness at its center. The Raindrop, in effect, makes the cornea a multifocal element with the central 2mm contributing to near vision and the remaining annular region of the cornea contributing to distance vision.

4.1.1.2 Multifocal contact lenses

Multifocal contact lenses are unique in that their power profile varies with radius. The most common paradigm for power geometry is a center-near profile, meaning that the central region of the lens has a greater optical power than the periphery. There are some examples of lenses that do not adhere to this norm, these lenses have a center-distance profile, i.e. the central region of the lens has a smaller optical power than the periphery. An example power profile of a center-near contact lens is shown in Figure 1.4. While some power profiles have slope discontinuities, most are slope continuous meaning it is mathematically smooth over the extent of the lens. Since both the Raindrop inlay and multifocal contact lenses do not function as gaze-selective devices, it is important to discuss their operation. The next section will elucidate the operation of these prosthetics.

4.2 Simultaneous Vision

The ReVision Optics Raindrop Corneal Inlay is surgically located and fixed within the cornea itself. Contact lenses sit directly on the eye and move with it during rotation of the globe. Therefore, an in focus image from the near point and an in focus image from the distance will be contemporary on the retina. This phenomenon is called simultaneous vision and is in contrast to spectacle lenses and contact lenses that have a constant optical power over their aperture, which are called single vision lenses. Gaze selective devices, such as a bifocal spectacle lens where the eye ball can rotate its gaze to select an optically different area of the lens, allow the eye to form and in focus image from a single object distance. Simultaneous vision lenses allow the eye to form an image of multiple object distances or sometimes a range of object distances.

There are both advantages and disadvantages to this method of near vision correction. An advantage of simultaneous vision devices is the user is free to look anywhere the eye is able and have both near and distance correction rather than being bound the the field of view within the spectacle lens, or subset regions of the spectacle lens for each task. Some disadvantages of simultaneous vision lenses are, depending upon the power geometry, loss of contrast and contrast sensitivity and slightly diminished distance acuity [21, 22]. This can be seen as a trade-off between distance vision and near vision, since both modalities persist simultaneously.

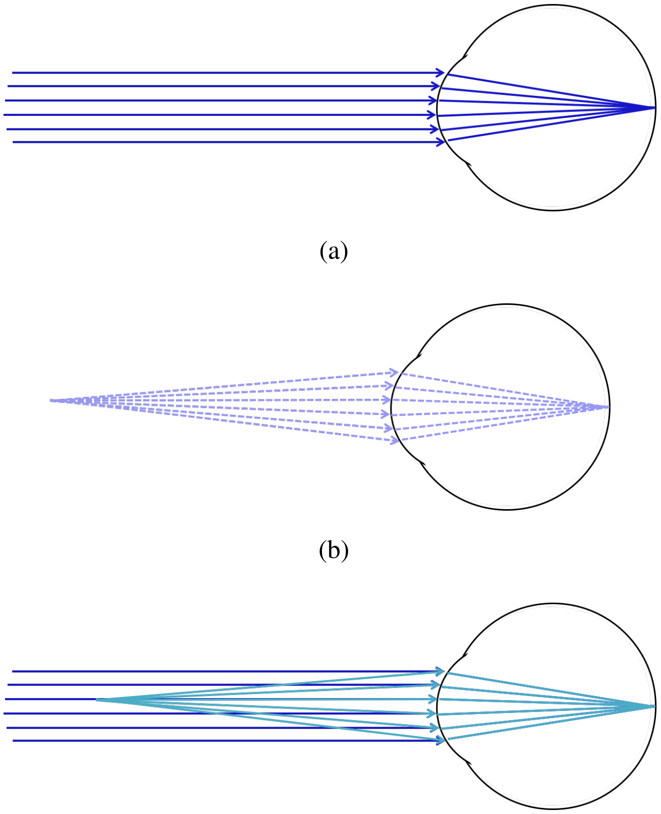

(a)

(b)

(c)

Figure 4.2: Schematic of simultaneous vision. (a) shows distance vision, (b) shows the eye focused at a near point, and (c) simultaneous vision showing both near and distance vision.

4.3 Multifocal IOLs

Intraocular lenses (IOL) are used in the treatment of cataracts. To surgically treat a cataract, the crystalline lens is removed, leaving the eye aphakic or without a lens. Often, an intraocular lens in implanted after the removal of the crystalline lens. The IOL is an artificial lens that allows a patient to regain sight and often obviates the need for spectacles, but removes the ability to accommodate. Multifocal IOLs are one method used satiate the desire for spectacle free vision, both near and distance. While there are many types of multifocal IOLs, we will discuss a singular class: diffractive multifocal IOLs. Figure 4.3 shows a diagram of a ReSTOR diffractive bifocal IOL. Diffractive multifocal IOLs usually come in the form of a refractive front surface and a diffractive rear surface.

The ReSTOR specifically employs an apodized diffractive surface such that the diffraction grating does cover the full extent of the clear aperture of the lens. In the case of a apodized diffractive *bifocal* IOL, the diffraction grating is optimized to diffract into the first order, giving a split between near and distance focus.

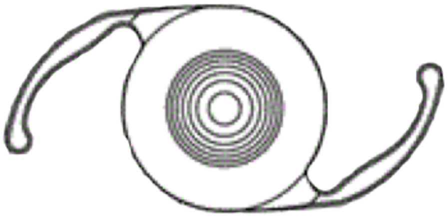

Figure 4.3: Diagram of a multifocal IOL, specifically a ReSTOR IOL. This view shows the diffractive surface, while the other surface would be a spherical or toric refractive surface.

Multifocal IOLs do give the user an increase in depth of field, but this gain does not come without a loss. An issue that can be found with use of diffractive IOLs is glare and holos, especially during use in dark scenarios with bright lights, e.g. driving at night [23]. Another issue that is inherent in the use of multifocal IOLs, similar to that of multifocal contact lenses, is the reduction in contrast of produced image [24]. These issue vary from user to user, but remain an present in use across the board.

4.3.1 Vertex Adjustment

Multifocal intraocular lens power, is specified in the plane of the IOL, this must be converted to power in the spectacle plane to compare to clinical data for trial lens defocus given at the spectacle plane. A multifocal IOL can be said to have two powers

$$\phi_{\text{IOL}} = \phi_{\text{base}} + \phi_{\text{add}} \tag{4.1}$$

ϕ_{base} is the base power of the IOL and ϕ_{add} is the add power. Since these powers are in contact, we can add them directly. Transferring the IOL power to the corneal plane

$$\phi'_{\text{IOL}} = \phi'_{\text{base}} + \phi'_{\text{add}}, \tag{4.2}$$

$$\phi'_{\text{IOL}} = \frac{\phi_{\text{IOL}}}{1 + t_1\left(\phi_{\text{IOL}}\right)}, \tag{4.3}$$

$$\phi'_{\text{base}} + \phi'_{\text{add}} = \frac{\phi_{\text{base}} + \phi_{\text{add}}}{1 + 0.005\text{m}\left(\phi_{\text{add}} + \phi_{\text{add}}\right)}. \tag{4.4}$$

With $t_1 = 5\text{mm}$ being the distance between the IOL plane and the corneal plane.

	Monofocal	ReSTOR +2.5	ReSTOR +3.0	ReSTOR +4.0
ϕ_{base}	20	20	20	20
ϕ_{add}	0	2.5	3.0	4.0
$\phi'_{\text{base}} + \phi'_{\text{add}}$	18.18	20.22	20.62	21.43
ϕ'_{add}	0	2.04	2.45	3.25

Table 4.1: IOL powers transferred to corneal plane. All powers given in diopters. Row 1 represents the nominal IOL power, Row 2 is the nominal IOL add power, Row 3 is the total IOL power transferred to the corneal plane, and Row 4 is the add power at the corneal plane.

Clinical through focus acuity (TFA) tests are performed by placing a spectacle lens $t_2 = 12\text{mm}$ in front of the eye. From our combined three thin lenses $\phi_{\text{cornea}} + \phi'_{\text{base}} + \phi'_{\text{add}}$ we expect two peaks in visual acuity. The first when $\phi_{\text{spec}} = 0$ due to the distance portion of the IOL (base power) and the second when ϕ_{spec} cancels the effect of ϕ'_{add}. Therefore, we can again transfer ϕ'_{add} to the spectacle plane so we can easily cancel it with the spectacle power ϕ_{spec}. Therefore

$$\phi''_{\text{add}} = \frac{\phi'_{\text{add}}}{1 + t_2\phi'_{\text{add}}} = \frac{\phi'_{\text{add}}}{1 + 0.012\text{mm}\phi'_{\text{add}}}. \tag{4.5}$$

	Monofocal	ReSTOR +2.5	ReSTOR +3.0	ReSTOR +4.0
ϕ'_{add}	0	2.04	2.45	3.25
ϕ''_{add}	0	1.99	2.38	3.125

Table 4.2: IOL powers transferred to spectacle plane. All powers given in diopters. Row 1 is the add power at the conceal plane and Row 2 is the add power of the IOL at the spectacle plane.

In actuality, $\phi_{\text{spec}} = -\phi''_{\text{add}}$ such that they cancel. However, in Chapter 5 the clinical data shown in Figures 5.8, 5.9, and 5.10 is displaying ϕ''_{add} vs. logMAR acuity. Figure 4.4 shows a schematic of the clinical test. A test lens is placed in the patient's spectacle plane. The patient reads the chart and the VA is recorded. The test lens is then replaced with another test lens of different power, and the VA measurement is repeated. This is done for every defocus value of interest, with a typical range of lens powers being -2.00D (which induces hyperopia) to +5.00D (which induces myopia) in 0.25D steps.

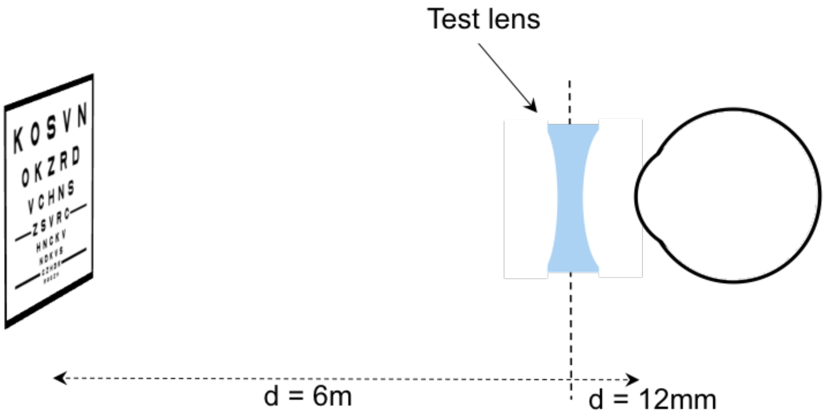

Figure 4.4: Clinical Through Focus Acuity testing. Test lens placed in patient's spectacle plane and the chart is read to determine VA. This is repeated for every value of defocus of interest.

4.4 Multifocal Contact Lenses

In the next chapter the qualitative and quantitiative performance of a range of multifocal contact lenses will be compared. These lenses include:

- Acuvue Moist Multifocal and Acuvue Oasys Multifocal (Johnson and Johnson Vision Care Inc, Jacksonville, FL),
- Biofinity Multifocal (CooperVision Inc.),
- PureVision Multifocal and PureVision2 Multifocal (Bausch & Lomb Inc., Rochester, NY),
- Biotrue ONEday Multifocal (Bausch & Lomb Inc., Rochester, NY),
- Clariti 1day Multifocal (Sauflon), Proclear 1 day Multifocal (CooperVision Inc.),
- Air Optix Multifocal (Alcon, Atlanta, GA), and
- Dailies AquaComfort Plus Multifocal (Alcon, Atlanta, GA).

A range of base power and add power for each lens type were used and is enumerated in Table 4.3. Transmitted wavefront data was measured using a ClearWave (Lumetrics, Rochester, NY) wavefront measurement system.

Lens Name	Replacement Frequency
Acuvue Moist Multifocal	Daily
Proclear 1 day Multifocal	Daily
Biotrue ONEday Multifocal	Daily
Clariti 1day Multifocal	Daily
AirOptix Multifocal	Daily
Dailies AquaComfort Plus Multifocal	Daily
Acuvue Oasys Multifocal	Semimonthly
Biofinity Multifocal	Monthly
PureVision Multifocal	Monthly
PureVision2 Multifocal	Monthly

Table 4.3: Multifocal contacts used in study.

Using the wavefront data and software developed in Chapter 2, we can generate through focus test charts and feed them through visual acuity estimation software that will be presented in Chapter 5 to estimate the visual acuity of an individual wearing one of these lenses.

CHAPTER 5

VISUAL ACUITY: ESTIMATION AND PREDICTION FOR PRESBYOPIC CORRECTIONS

As discussed in Chapter 1, there are many different solutions used in the treatment of presbyopia. This chapter will explore software that was developed to estimate and eventually predict visual acuity. Although this software has been used to investigate multifocal optics and presbyopic treatments, it could be used for monofocal ophthalmics as well. In order to elucidate the software and its results, a discussion is needed of a few tertiary topics: visual acuity, metrics and methods for measuring visual acuity and retinal anatomy and structure. Visual acuity describes an individual's ability to resolve some target, typically a letter chart with targets of diminishing size is used. Here we will discuss different measures of visual acuity as well as their drawbacks and benefits. A strategy for predicting visual acuity when multifocal elements are in place will be described as well.

5.1 Visual Acuity

One common measure of visual acuity was invented by Dutch ophthalmologist Herman Snellen [25, 26]. Snellen came up with a chart for measuring visual acuity shown in Figure 5.1a. The chart was designed to be read from a specified distance, originally 20 Paris feet [27]. A patient would read the chart, and the smallest (lowest on the chart) line that could be read would be recorded. The Snellen fraction was defined to be [28]

$$S = \frac{\text{Greatest distance the subject can just read a given line on the chart}}{\text{Greatest distance a "normal" observer can read the same line on the chart}}. \tag{5.1}$$

One of the drawbacks of the Snellen measure of acuity can immediately be seen that it references a “normal” observer.

While the Snellen acuity chart has been around since the mid-nineteenth century and widely used, the ETDRS chart was developed in order to achieve a standardization of test [27]. In clinical research the ETDRS charts are predominantly used due to its numerous advantages in this setting. Namely, the ETDRS chart is advantageous over a Snellen chart for two reasons. First, the ETDRS chart has a constant number letters per line. From a clinical standpoint, this is advantageous because the probability of correctly guessing all of the letters on the line correctly is the same which cannot be said for the Snellen chart which has a few as 1 letter per line (20/200 line, top) and as many as 8 letters per line (20/5 line, bottom). The second advantage of the ETDRS chart is that the size progression from line to line was chosen purposefully to be a constant rate of 0.1 on the logMAR scale (more on this in the next paragraph. Snellen originally designed his chart for use at 20 Paris feet, which is approximately 6.5m, with letter sizes for viewing at 20, 30, 40, 50, 70, 100, and 200 feet. It is unclear if Snellen had a methodology in mind when choosing these size/distances, nonetheless the progression closely approximates a geometrical progression with a factor of 10 change in letter size in 6 steps regardless of starting location [27]. This gives an approximate line-to-line ratio of $\sqrt[6]{10}$. Whereas the ETDRS chart has a logarithmic progression in letter size.

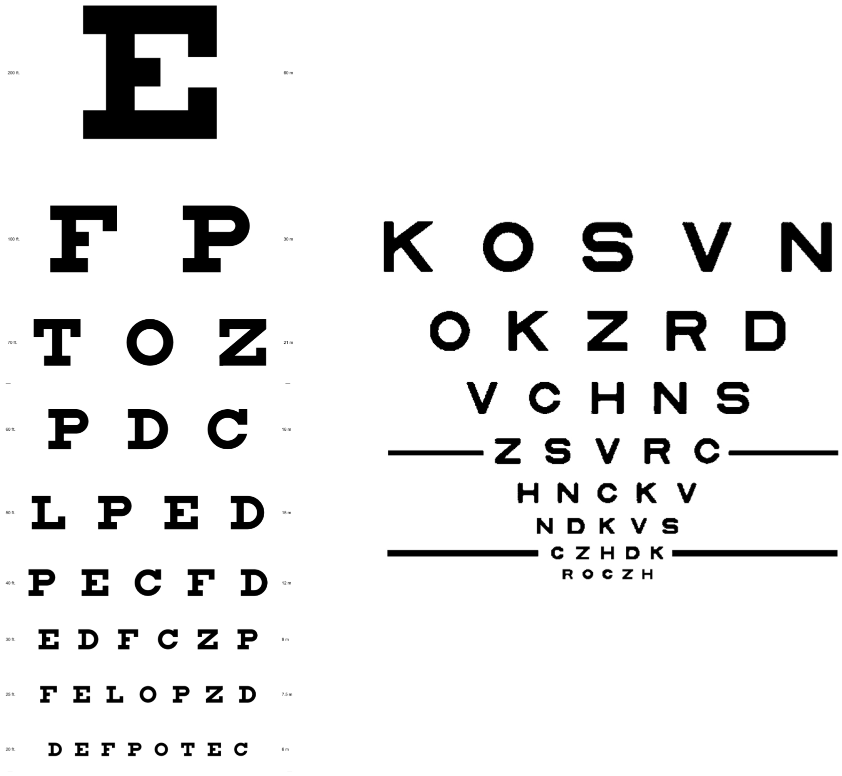

(a) (b)

Figure 5.1: (a) Snellen chart, commonly used with one letter on the largest, top, line which is usually $S = 20/200$ through up to eight or more letter per line near the bottom, which as shown above is the $S = 20/5$ line. (b) ETDRS chart. Developed to standardize the clinical test chart used. Constant line-to-line ratio in letter size as well as a constant number of letters per line.

Figure 5.1 shows both a Snellen chart and a ETDRS chart.

LogMAR is a measure of acuity that is aimed at having a continuous value, rather than the discrete steps of the Snellen measure and others. logMAR is short for the logarithm of minimum angle of resolution. Extrapolating on the idea of the minimum angle of resolution, a discussion of the retinal anatomy is necessary.

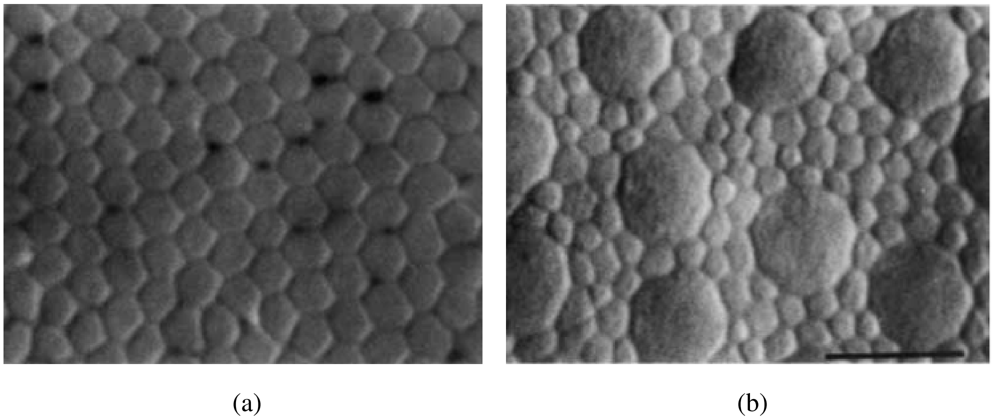

Figure 5.2: Images reproduced from Curcio *et al.* (1990) [3]. (a) and (b) shows en face optical sections of a human retina. (a) shows the central fovea region, light grey roughly hexagonal shapes are cones. (b) shows the near periphery, large shapes are cones with small shapes between being rods. Scale bar for both shown in (b) is 10µm

The fovea is the region of the retina that is densest with photoreceptors, specifically cones. Figure 5.2 shows en face section of two regions of a human retina, in the fovea and periphery. In the fovea, which is the region of the retina aligned with the visual axis, the only photoreceptor present are cones. In this region the cones are smallest and most densely packed. Moving away from the fovea, the cones become larger, and less densely packed with the intervening region filling with rods. A more complete discussion of retinal structure can be found in Section 5.2. From Figure 5.2 it can be seen that the approximate diameter of a cone is $d_{\text{cone,fovea}} \approxeq 2.5\mu\text{m}$. Therefore, the angular extent of a cone in the fovea, projected into object space is

$$h = f \tan\theta, \tag{5.2}$$

$$\theta = \arctan\left(\frac{h}{f}\right), \tag{5.3}$$

$$\theta_{\text{cone,fovea}} = \arctan\left(\frac{d_{\text{cone,fovea}}}{f_{\text{eye}}}\right), \tag{5.4}$$

$$\theta_{\text{cone,fovea}} = \arctan\left(\frac{2.5\mu\text{m}}{17\text{mm}}\right) \approxeq 05\text{arcmin}, \tag{5.5}$$

with $f_{\text{eye}} \approxeq 17\text{mm}$ corresponding to a total ocular power of about 60D [28]. In order to resolve two features, the image of the features must fall onto two cones separated by another. Therefore the smallest resolvable feature in the retina space, can be considered to be two cones, a “bright” cone and a “dark” cone. Thus, smallest feature resolvable by the eye has an angular extent $2\theta_{\text{cone,fovea}} = 1\text{arcmin}$. Of course there are variations in the focal length of eyes due to the natural variation in anatomical shapes, but this value has been standardized for acuity measurement. Therefore the minimum angle of resolution is $\text{MAR} = 2\theta_{\text{cone,fovea}}$, and the base 10 logarithm is taken such that the logMAR value has a value of zero,

$$\text{logMAR} = \log_{10} 2\theta_{\text{cone,fovea}} = 0. \tag{5.6}$$

It turns out that many individuals have a logMAR acuity less than zero, corresponding to better than a Snellen fraction of 20/20. The logMAR value can be calculated for an individual by taking the base 10 logarithm of the angular extent of the smallest resolvable feature, measured in minutes of arc. In practice, this could be quite cumbersome, therefore, the logMAR value can also be calculated as the logarithm of the inverse of the Snellen fraction, that is

$$\text{logMAR} = \log_{10}\left(\frac{1}{S}\right), \tag{5.7}$$

where S is the Snellen fraction defined in Equation 5.1.

Letters read can be counted in order to score the VA, starting on the top left of the chart and moving towards the bottom right. Each letter on the logMAR chart has a value of 0.02 log units with each line having a value of 0.1 log units given the 5 letters per line[29]. Therefore the logMAR Visual Acuity (logMAR VA) can be calculated as

$$\text{logMAR VA} = 0.1 + \text{value of smallest line read} - 0.02 \times (\text{number of letters read})\,. \quad (5.8)$$

Which gives a more continuous value for the logMAR VA by assigning value to each letter of the chart.

5.2 Retinal Anatomy

There are three known classes of photosensitive neurons in the human retina: rods, cones, intrinsically photosensitive retinal ganglion cells. Rods contain rhodopsin, which a photosensitive receptor protein. Rods are extremely sensitive and contribute to low light monochromatic vision [30, 31]. Cones contain one of three types of photopsin, which are photosensitive receptor portions that are sensitive to different regions of the spectrum.[1] Cones are designated L, M, and S cones corresponding to the region of the visible spectrum they are sensitive to Long, Medium, and Short wavelengths. [28] Cones are responsible for color vision. Finally, intrinsically photosensitive retinal ganglion cells contain the photosensitive receptor protein melanopsin and play a role in our circadian rhythm among other things [33–35]. These cells do not play a role in image formation.

The retina and brain are responsible for a significant amount of post-processing of visual data, at the retinal level, processing occurs before any information is transmitted to the brain [36–38]. The neural cells in the retina play a major role in this data processing. Figure 5.3 shows diagram of a cross section of retina. The reader should take note of the three types of cells connecting the rods and cones to the retinal ganglion cells and to each other. These are the amacrine cells, bipolar cells, and horizontal cells. The function of these cells has been shown to allow them to do what amounts to boost contrast near edges,

---

[1] This is true for trichromats, or persons with three types of cones. There is evidence that some women, a very small portion of the population, have four functional types of cones. [32]

among other things. In effect, these cells are doing on-board image processing. This will become an important feature in the discussion in Section 5.3.2.

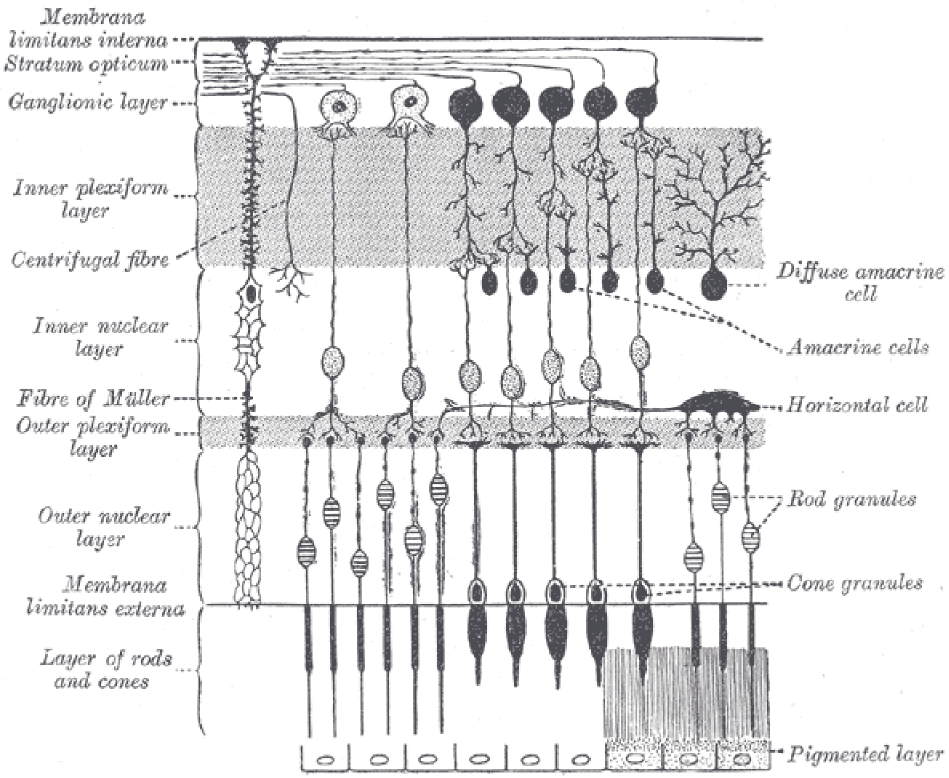

Figure 5.3: Retinal anatomy. Amacrine cells connect two or more retinal ganglion cells, bipolar cells connect two or more photoreceptors (rods and cones) to two or more retinal ganglion cells, horizontal cells connect several photoreceptors.

5.3 Estimation and Prediction of Visual Acuity

As discussed in previous sections, many modern ophthalmic appliances induce the eye to become multifocal. To understand how these devices affect vision, we present tool developed to estimate visual acuity from simulated letter chart images by selecting and correlating individual letters of an aberrated ETDRS acuity chart with an unaberrated (control) chart. The tool was motivated by a project with ReVision Optics and initially developed for estimating visual acuity from images simulated using the following method, specifically for understanding effect of their Raindrop Corneal Inlay.

Aberrated letter charts were simulated using the Liou-Brennan model eye in the Zemax raytracing program [4]. According to Liou and Brennan, model was developed for image quality calculations among other things and is considered to be a “quasi-true anatomical representation of an average emmetropic human eye” [4]. Using a method and data presented in Steinert *et al.* A Zemax “phase surface” was added to the model eye’s pupil. The phase surface was used to bias the model eye to the mean preoperative aberrations of patients in that study, using the mean preoperative wavefront [39]. This will be the “monofocal model” in Sections 5.3.2 and 5.3.3.1. From there, the eye model changed such that the anterior corneal surface was representative of the mean anterior corneal surface height of the postoperative eyes. The image simulation tool in Zemax was used to simulate the retinal image of a standard ETDRS letter chart for the preoperative and postoperative eyes. Finally, ETDRS chart retinal images were generated with Zemax’s image simulation tool. Table 5.1 describes the structural parameters of the Liou-Brennan schematic eye model.

Surface	Radius (mm)	Asphericity	Thickness (mm)	n at 555nm
1	7.77	-0.18	0.50	1.376
2	6.40	-0.60	3.16	1.336
3 (pupil)	12.40	-0.94	1.59	Grad A
4	Infinity	–	2.43	Grad P
5	-8.10	+0.96	16.27	1.336

Table 5.1: Structural parameters of the Liou-Brennen schematic eye model [4].

These charts were correlated with an unaberrated chart in order to estimate the visual acuity of a subject with an eye corresponding to the eye model. This technique demonstrates its utility in simulating the visual acuity for eye models with multifocal contacts, intraocular lenses, and corneal inlays.

With the VA tool developed, it can be used to investigate the effects of other ophthalmic appliances on visual acuity. For these appliances, those other than the ReVision Optics Raindrop Corneal Inlay, images were simulated using methods developed in Chapter 2. That is, wavefront data or a physical prescription of the optic was used to generate an Optical Transfer Function, and a blurred image was generated in the Fourier domain.

5.3.1 Background

With a monofocal optic like that of the preoperative model in the previous section, one avenue for pursuing a metric that encapsulates "readability" is that of a contrast based metric. One way this can be understood is that blur will be predominantly symmetric through focus. Thus, a contrast based metric can do well as a first order approximation. Here, contrast describes the difference in pixel values to between a completely white letter (pixel value of 255) on a completely black background (pixel value of 0). With more complex through focus behavior like that from the postoperative eye model, or a multifocal ophthalmic appliance as discussed, a more complex metric is needed in order to capture this behavior. The nature of the blur from one of these simultaneous vision multifocal elements suggests that edges are important in pattern recognition. It has also been suggested in the literature that edges are an important part of image formation and recognition [37, 40].

The metrics used in the VA estimation tool are elucidated below. The goal in using these metrics is to identify an appropriate threshold value of the metrics that will allow for detection of a readable letter in a given location in the blurred chart.

5.3.2 Metrics

The contrast based metric can be described as a point-wise correlation of the source image in 5.4a with the aberrated image in 5.4b. Mathematically, the contrast based metric is:

$$\text{Contrast metric} = \sum_{i,j} \frac{A(i,j) \cdot B(i,j)}{[A(i,j)]^2} \tag{5.9}$$

with $A(x,y)$ being a single letter section of the inverted binary source image (Figure 5.4a) and $B(x,y)$ is a single letter section of the inverted aberrated image (Figure 5.4b). The edge-enhancement metric aims to identify edges and sharpness of edges while still allowing the central "fill" region of the letter to contribute. Pictorially, in Figure 5.5, the edge-enhancement metric will be a point-wise correlation of the images in the third column. The edge enhanced metric is given as

$$\text{Edge enhancement metric} = \sum_{i,j} \frac{1}{4} \frac{S(i,j) \cdot T(i,j)}{[S(i,j)]^2} \tag{5.10}$$

with $S(x,y)$ being a single letter section of the sum of: the inverted source image and the gradient of the source image. $T(x,y)$ is a single letter section of the sum of: the inverted aberrated image raised to the real, constant power γ and the gradient of the aberrated image. That is:

$$S = \frac{255 - \text{Source}}{255} + \text{grad}(\text{Source}), \tag{5.11}$$

$$T = \left(\frac{255 - A}{255}\right)^{\gamma} + \text{grad}(A), \tag{5.12}$$

$$\text{Combined metric} = (1 - gradSplit)\,\text{Contrast metric} + (gradsplit)\,\text{Edge metric}. \tag{5.13}$$

Where *gradsplit* is the weighting associated with the edge enhancement metric, scaled between zero and unity. "Threshold" is the level of Combined Metric that predicts VA and is chosen such that the predicted or estimated VA is well matched to the known data. The parameter γ, dubbed γ-correction, allows for an overall remapping of gray levels in the blurred image.

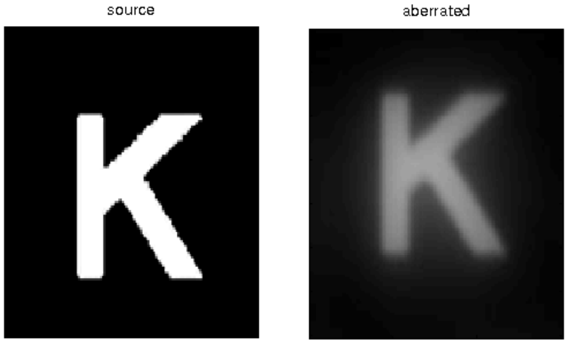

(a) (b)

Figure 5.4: Contrast metric images. (a) Inverted source image, (b) inverted blurred image. Note: grayscale mapping is consistent for both images.

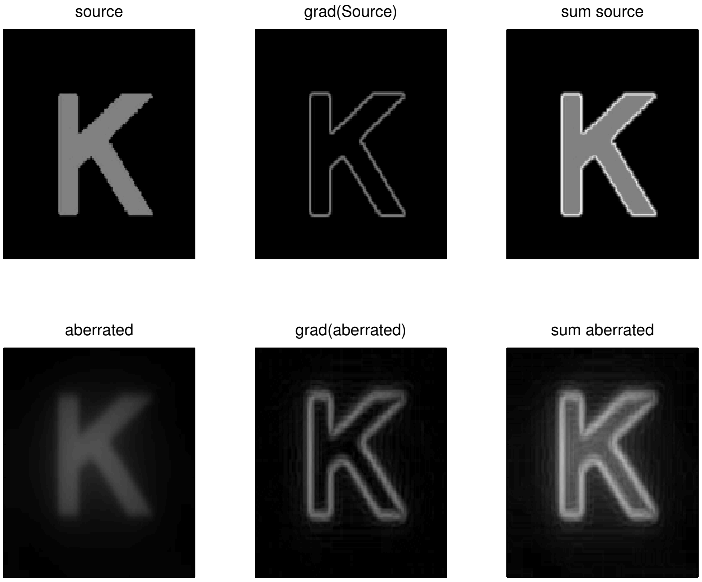

Figure 5.5: Edge-enhancement metric images. Top row, left to right: source image, gradient of source image, sum of source and gradient images. Bottom row, left to right: aberrated image, gradient of aberrated image, sum of aberrated and gradient images. Note: grayscale mapping is consistent for all six images.

The contrast metric captures behavior of blurring of a letter somewhat uniformly. It identifies that contrast, or pixel value difference, between a region where an in focus letter is expected and a region where an in focus letter is not expected (background region). The edge-enhancement metric aims to capture edge presence and sharpness information, yet also allows the inner fill region of the letter to contribute. These metrics can be thought of as inspired by the neurons in the retina discussed in detail in Section 5.2. The amacrine, bipolar, and horizontal cells serve to adjust “gain” in their signals, relative to their inputs which can be many cones in the fovea. These cells can alter the signals they send to the brain based on the signals they receive, i.e. boost contrast where there is a perceived edge.

5.3.3 Results

There are several assumptions implicit in this section of work. First, we assume that the base power corrects the individual’s distance vision. At the simulation level, this means that the software adds a phase to the measured wavefront equal to and opposite in sign as would be induced by the lens base power. From a clinical standpoint, this assumption makes sense as patients would have their distance vision corrected as a first step in fitting the lens by an optometrist. The second assumption or simplification made is that we assume no other aberrations are induced by the cornea or crystalline lens. With some added sophistication to the VA estimation software, an actual patient's ocular aberrations could be measured and added to the power profile used in these simulations, giving rise to more realistic simulated retinal images. However, this added complication is not needed at this point. Schwiegerling accomplished part of this, by taking patient corneal topographic data and incorporating those data into an eye model used for simulating retinal images [8]

5.3.3.1 ReVision Optics Raindrop Near Vision Corneal Inlay

For the monofocal case, with a 3.5mm pupil, our metric predicts the standard observer visual acuity for defocus values over the range ±2.0D well (to within 5 letters). Nonetheless, for all pupil sizes, clinical data is predicted fairly well, shown in Figure 5.6.

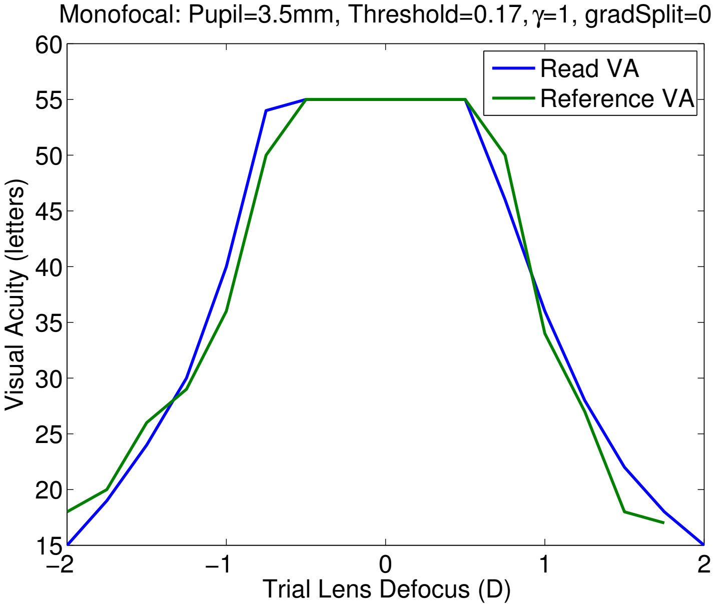

Figure 5.6: Defocus curve for preoperative clinical data provided by ReVision Optics.

For the multifocal case shown in Figure 5.7, with a 3.5mm pupil, the algorithm adequately predicts the standard observer visual acuity with the exception of two regions. The algorithm under-predicts the standard observer visual acuity with defocus less than −4.0D where contrast is greatly reduced. Near −2.0D, the algorithm fails to pick up the slight dip in VA apparent in the simulated images. Since clinical data was not available for Raindrop Inlay recipients, "standard observer" data was used for the reference VA for the inlay curves. These data were generated using three "standard observer" emmetropes, presented with simulated through focus ETDRS chart images. This effort was designed to develop metrics that capture features in multifocal simulated images. Human readers are not ideal and can learn to recognize blurry letters. However, now that the metrics are developed, their parameters can be optimized against a clean set of objectively measured data.

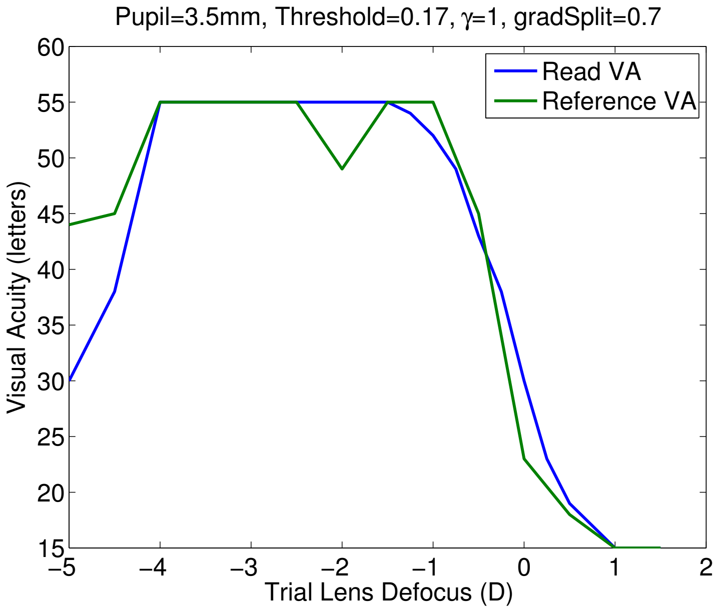

Figure 5.7: Data from standard observers reading images simulated with ReVision Optics' postoperative model eye. Data is overpredicted by the algorithm near -2D and -4.5D to -5D. At these defocus values, the model eye produces images with very low contrast between letter and background, yet still produces "clear" letters.

5.3.3.2 Alcon AcrySof® IQ ReSTOR® IOLs

Once the algorithm and metrics were developed using the data and images from ReVision Optics, the tool could be used to investigate the effect on VA and performance of other ophthalmic appliances. The first appliance that will be investigated is the Alcon Acrysof IQ ReSTOR IOL. Alcon provided physical prescription for three different styles of their ReSTOR IOL, a +2.5D add power, +3.0D add power, and +4.0D add power. Additionally, Alcon provided postoperative clinical acuity data from three separate clinical cohorts that had each of the three styles of IOL implanted during cataract surgery. These data are represented by the red curves in Figures 5.8 - 5.10. Error bars in the data are one standard deviation of the clinical cohort population above and below the mean. Figure 5.8 shows the visual acuity prediction and corresponding clinical data for ReSTOR +4.0D IOL recipients (red) along with estimate data from our tool. Figures 5.9 and 5.10 show similar curves for the clinical data and the +3.0D and +2.5D add lenses respectively.

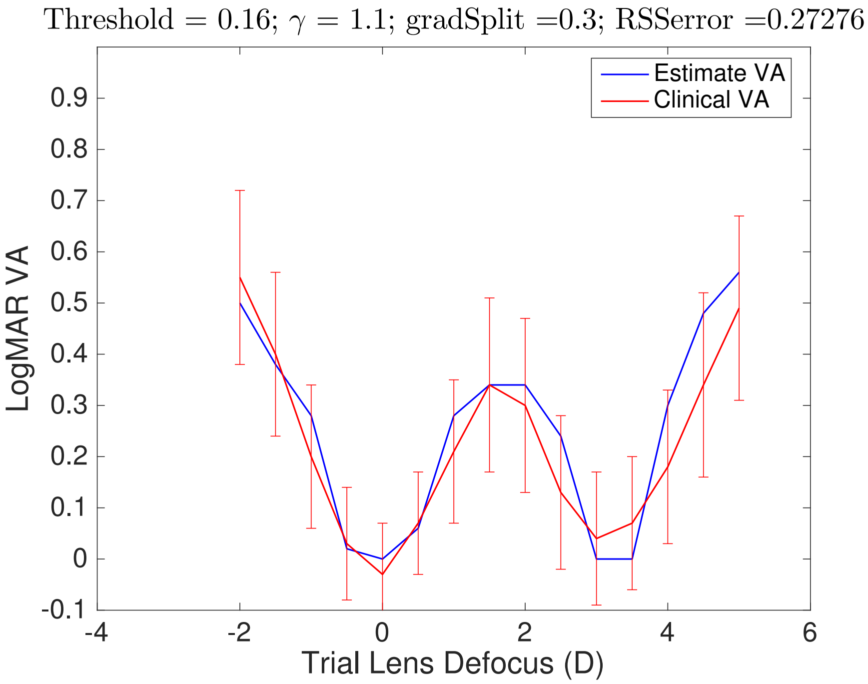

Figure 5.8: Comparison of clinical data for AcrySof® IQ ReSTOR® +4.0 Diopter (D) Intraocular Lens (IOL). This fit is generated with a threshold of $thresh = 0.16, \gamma = 1.1$, and $gradSplit = 0.3$, meaning this fit only uses the contrast metric. The error bars are $\pm\sigma$.

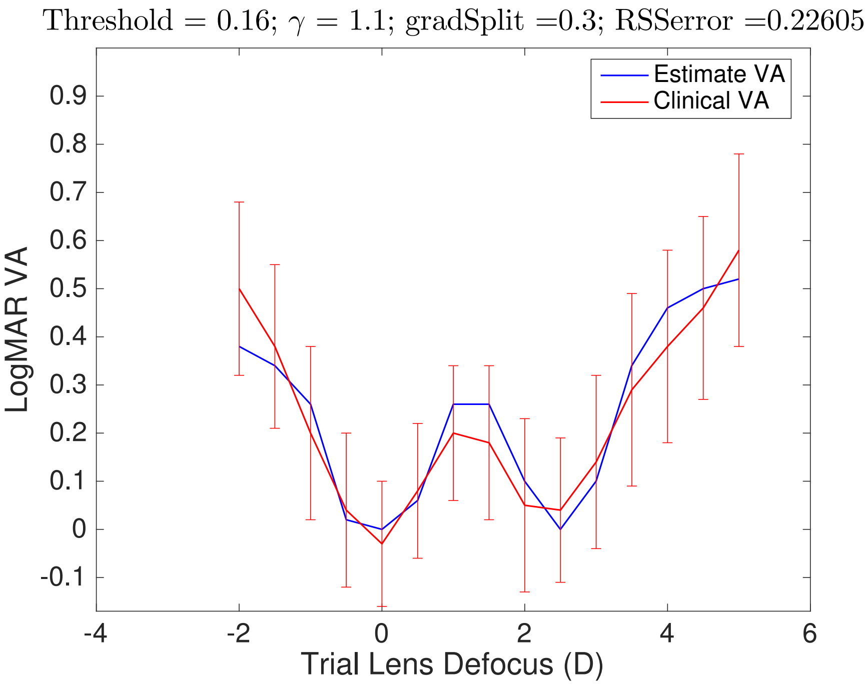

Figure 5.9: Comparison of clinical data for AcrySof® IQ ReSTOR® +3.0 Diopter (D) Intraocular Lens (IOL). This fit is generated with a threshold of $thresh = 0.16, \gamma = 1.1$, and $gradSplit = 0.3$, meaning this fit only uses the contrast metric. The error bars are $\pm\sigma$.

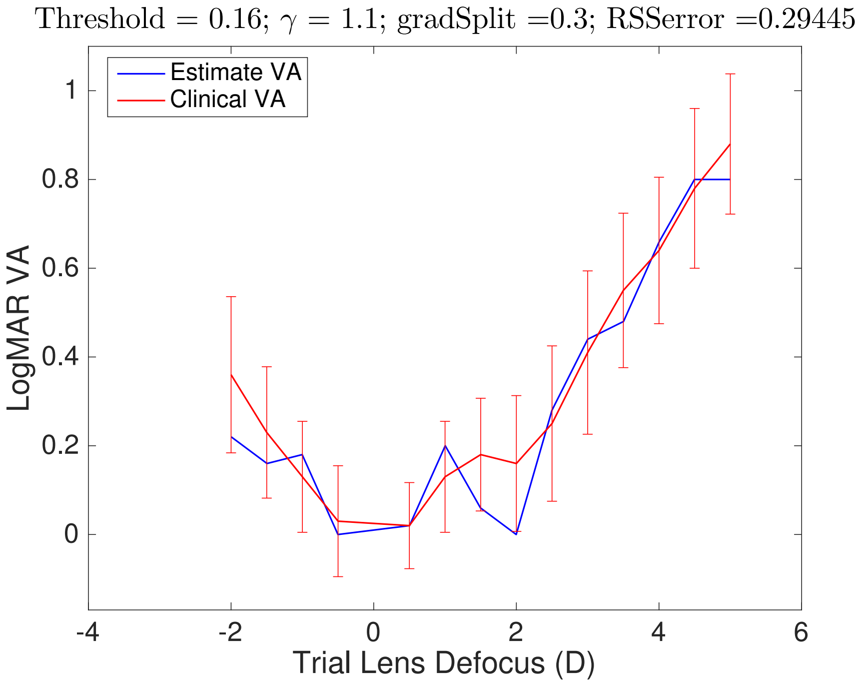

Figure 5.10: Comparison of clinical data for AcrySof® IQ ReSTOR® +2.5 Diopter (D) Intraocular Lens (IOL). This fit is generated with a threshold of $thresh = 0.16, \gamma = 1.1$, and $gradSplit = 0.3$, meaning this fit only uses the contrast metric. The error bars are $\pm\sigma$.

Parameters $threshold, \gamma,$ and $gradsplit$, representing the combined metric threshold, $\gamma-$correction, and metric weighting respectively were optimized by hand to produce the least total error in all three lens cases, where error is the root sum square (RSS) difference between clinical and estimate data. In general it seems like the metrics predict distance vision well, but tend to overpredict performance for the near vision and slightly underpredict performance of the intermediate vision. Nevertheless, the predictions tend to be within the error bars of the defocus curves. Now that this choice of parameters has been identified, we can use this tool, with this parameter set to predict visual acuity performance with other multifocal elements, namely, multifocal contact lenses.

5.3.3.3 Multifocal Contacts - Qualitative Results

Images shown in the following sections show a more qualitative way of making comparisons between lenses. These images show letter targets with a 20/80, 20/40, and a 20/20 letter E. The images show a series of targets with varying amounts of defocus in quarter diopters ranging from 2.5D on the far left and 0D on the far right.

Daily disposable contact lenses Figure 5.11 shows a comparison of low add power daily disposable contact lenses, each row was generated using data from a single lens type. Presented from top to bottom are, Air Optix, Acuvue Moist (AVMOIST), Biotrue, Clariti, Dailies Aqua Comfort Plus (DACP), and Proclear. Of the low add daily lenses shown in Figure 5.11, the Biotrue seems to have the largest range of focus, with a recognizable 20/80 letter out to about 1.50D. Air Optix, Clariti, and DACP come close to this range, showing a recognizable 20/80 letter to about 1.25D, and the AV MOIST and Proclear lenses have the smallest range of focus, showing a recognizable 20/80 letter to about 0.75D and 0.50D respectively.

The medium add category requires some explanation. The Proclear lenses are only available in one power profile design, therefore the images shown in Figures 5.11 - 5.13

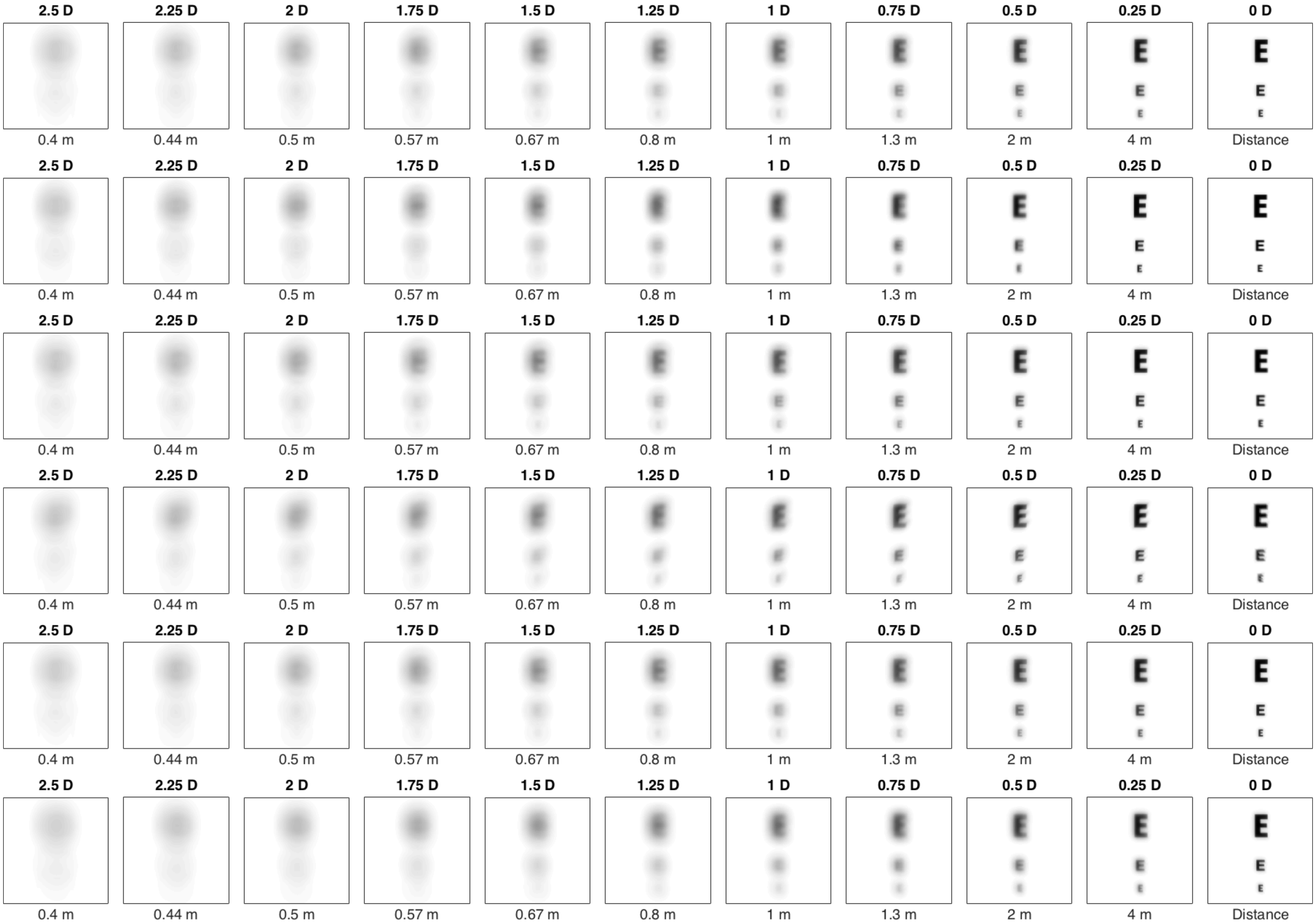

Figure 5.11: Dailies Contacts- Low Add, 4mm pupil. Images assume zero accommodation and are generated monocularly. From top to bottom: Air Optix, AVMOIST, Biotrue, Clariti, DACP, Proclear

designated Proclear were all generated using the same data. The Clariti lens does not have a medium add, only high and low, so it does not appear in Figure 5.12 The medium add comparison is shown in Figure 5.12, from top to bottom: Air Optix, AV MOIST, DACP, and Proclear. Here, the Air Optix and DACP lenses clearly show the largest range of focus, with a recognizable 20/80 letter to about 1.75D or 2D. AV MOIST has a range of focus of about 1.5D, and Proclear has a range of focus of about 0.5D.

In in high add category, images are shown in Figure 5.13. The Air Optix, AV MOIST, and DACP lenses show the largest range of focus of about 2.5D, with the Air Optix and DACP having slightly better contrast at the far left. The Clariti lens has a range of focus of about 2D - 2.25D, and the Proclear again has a range of about 0.5D.

Figure 5.14 shows the low add semimonthly and monthly contact lens images. The Biofinity N +1.00D and +1.50D lenses had a range of focus of about 1.75D, followed by the AV OASYS with a range of 1.50D. The Purevision lens had a range slightly larger than 1.25D. The Biofinity D +1.00 and +1.50 lenses had ranges of focus slightly larger than 1.00D and slightly less than 0.75D respectively. The Purevision2 lens hand a range of focus slightly less than 0.75D. The medium add semimonthly and monthly lenses are shown in Figure 5.15, missing are the Purevision and Purevision2 lenses which are not available in medium add. The AV OASYS lens had a large range of focus for a medium add lens at 2.50D, followed by the Biofinity N lens with a range of focus slightly larger than 1.75D, and finally the Biofinity D lens had a range of focus of about 1.00D. Monthly and semimonthly lenses are shown in Figure 5.16. Here, the Biofinity N and Purevision2 both had a large range of focus of over 2.50D and 2.50D respectively. The Biofinity N lens shows excellent contrast at for near vision (left side of row), yet performs poorly in the distant-intermediate, near about 1.00D. The AV OASYS and Purevision2 both had a range of focus of about 1.50D, and finally the Biofinity D lens had a range of focus of about 1.00D.

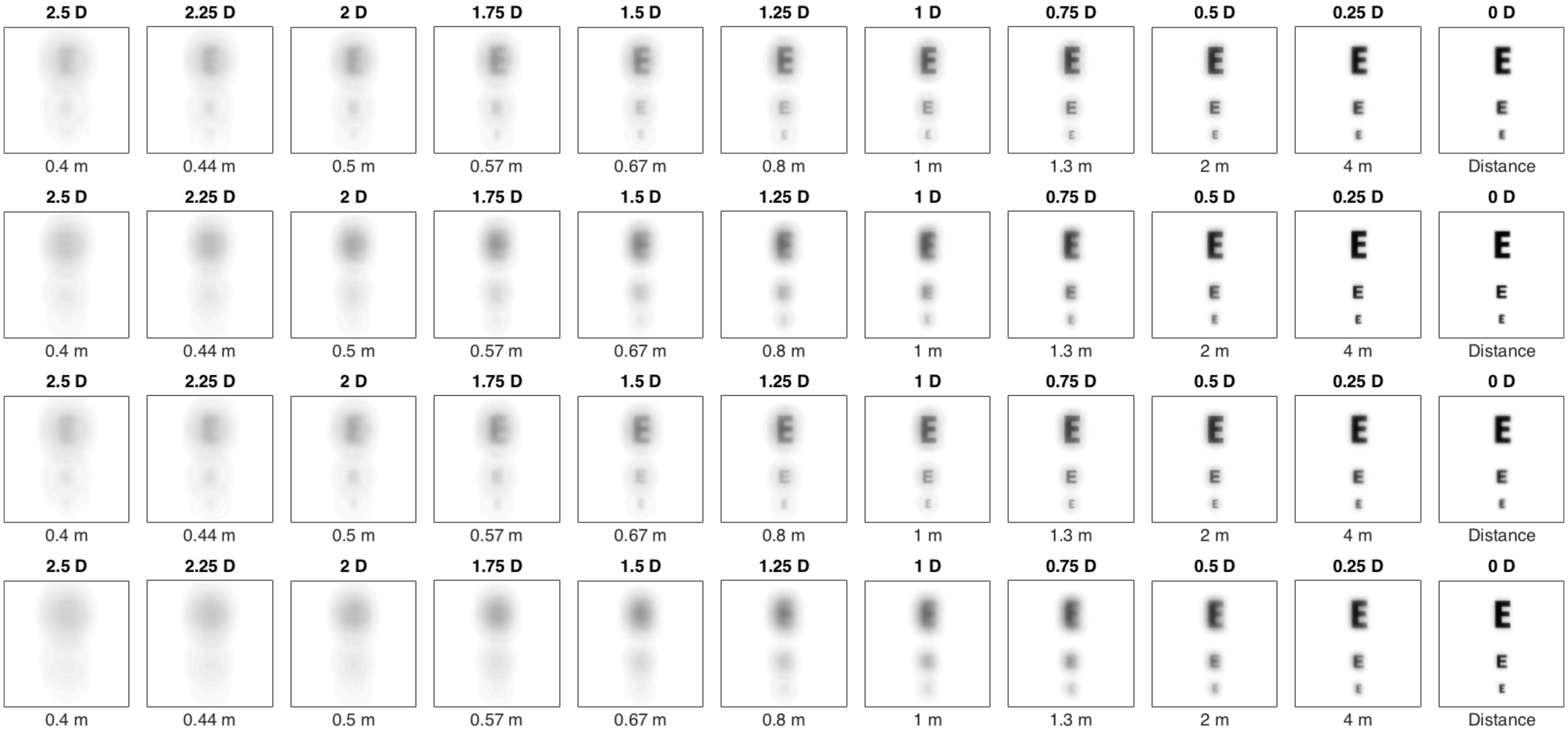

Figure 5.12: Dailies Contacts - Medium Add, 4mm pupil. Images assume zero accommodation and are generated monocularly. From top to bottom: Air Optix, AVMOIST, DACP, Proclear

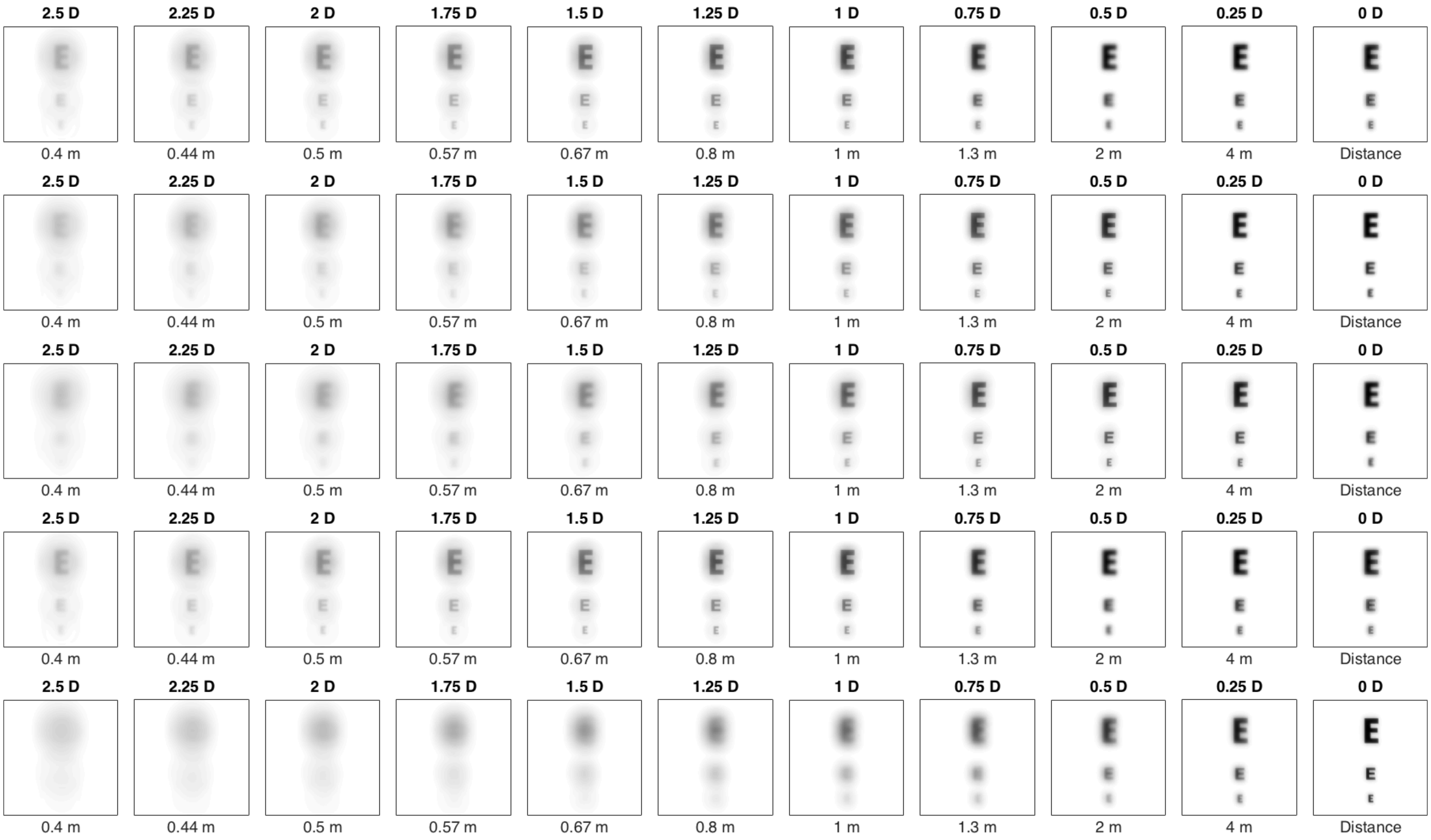

Figure 5.13: Dailies Contacts - High Add, 4mm pupil. Images assume zero accommodation and are generated monocularly. From top to bottom: Air Optix, AV MOIST, Clariti, DACP, Proclear

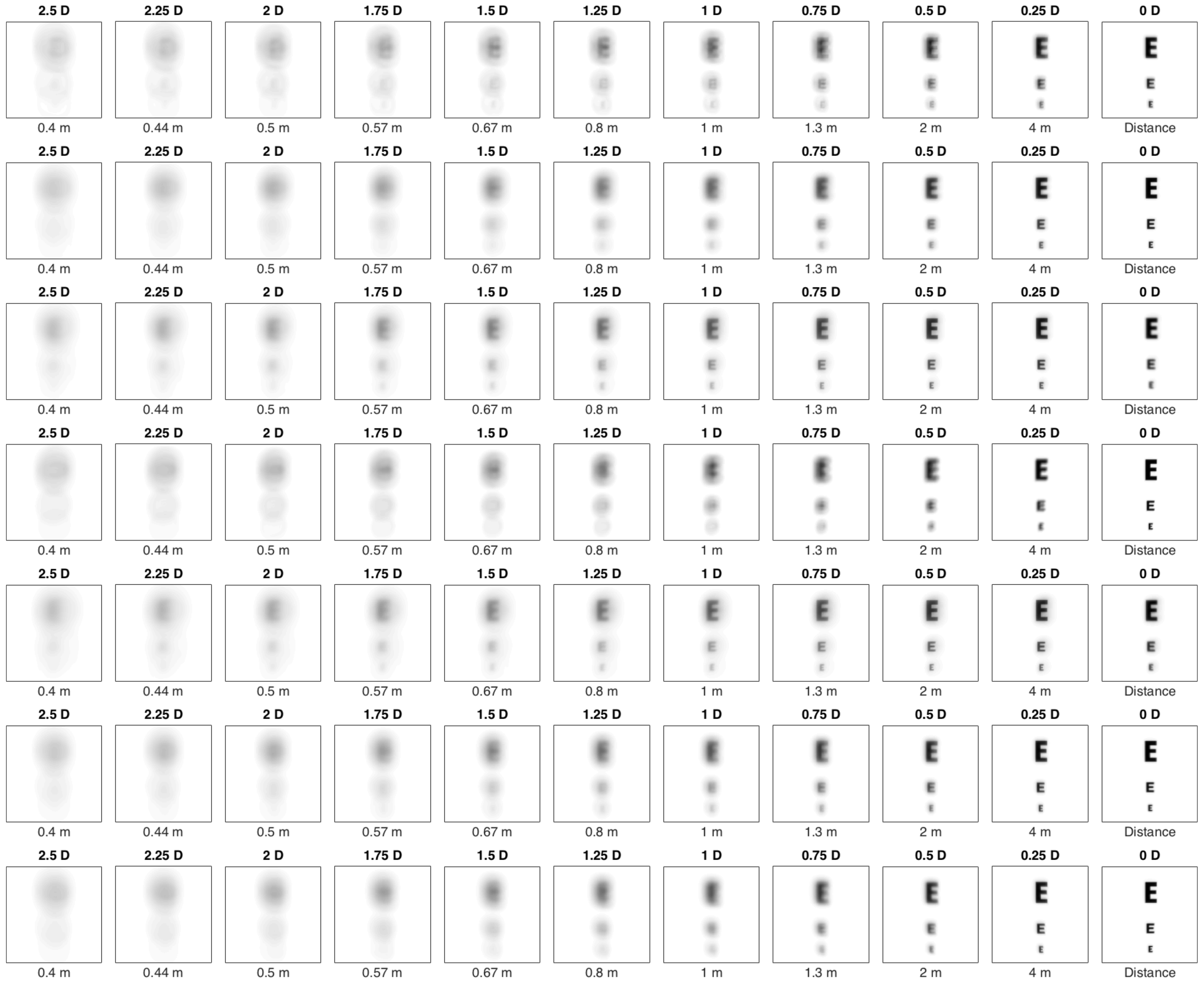

Figure 5.14: Semimonthly and Monthly Contacts - Low Add, 4mm pupil. Images assume zero accommodation and are generated monocularly. From top to bottom: AV OASYS, Biofinity +1.0 D, Biofinity +1.0 N, Biofinity +1.5 D, Biofinity +1.5 N,Purevision, Purevision2

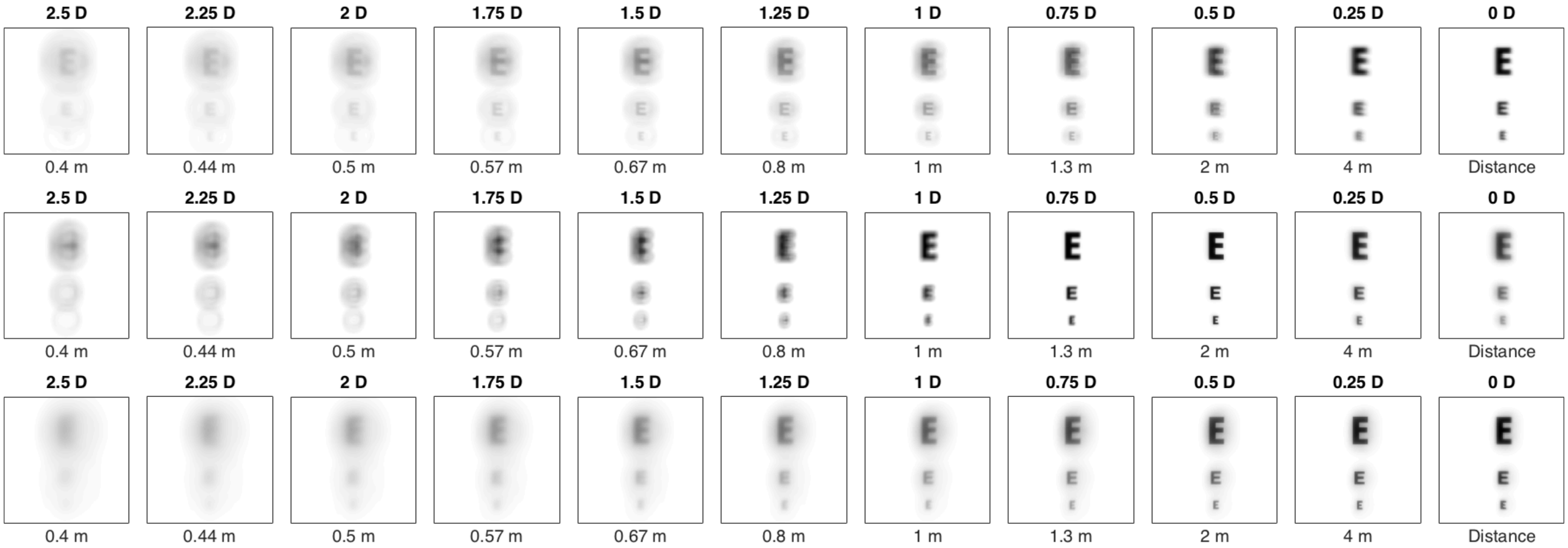

Figure 5.15: Semimonthly and Monthly Contacts - Medium Add, 4mm pupil. Images assume zero accommodation and are generated monocularly. From top to bottom: AV OASYS, Biofinity +2.0 D, Biofinity +2.0 N

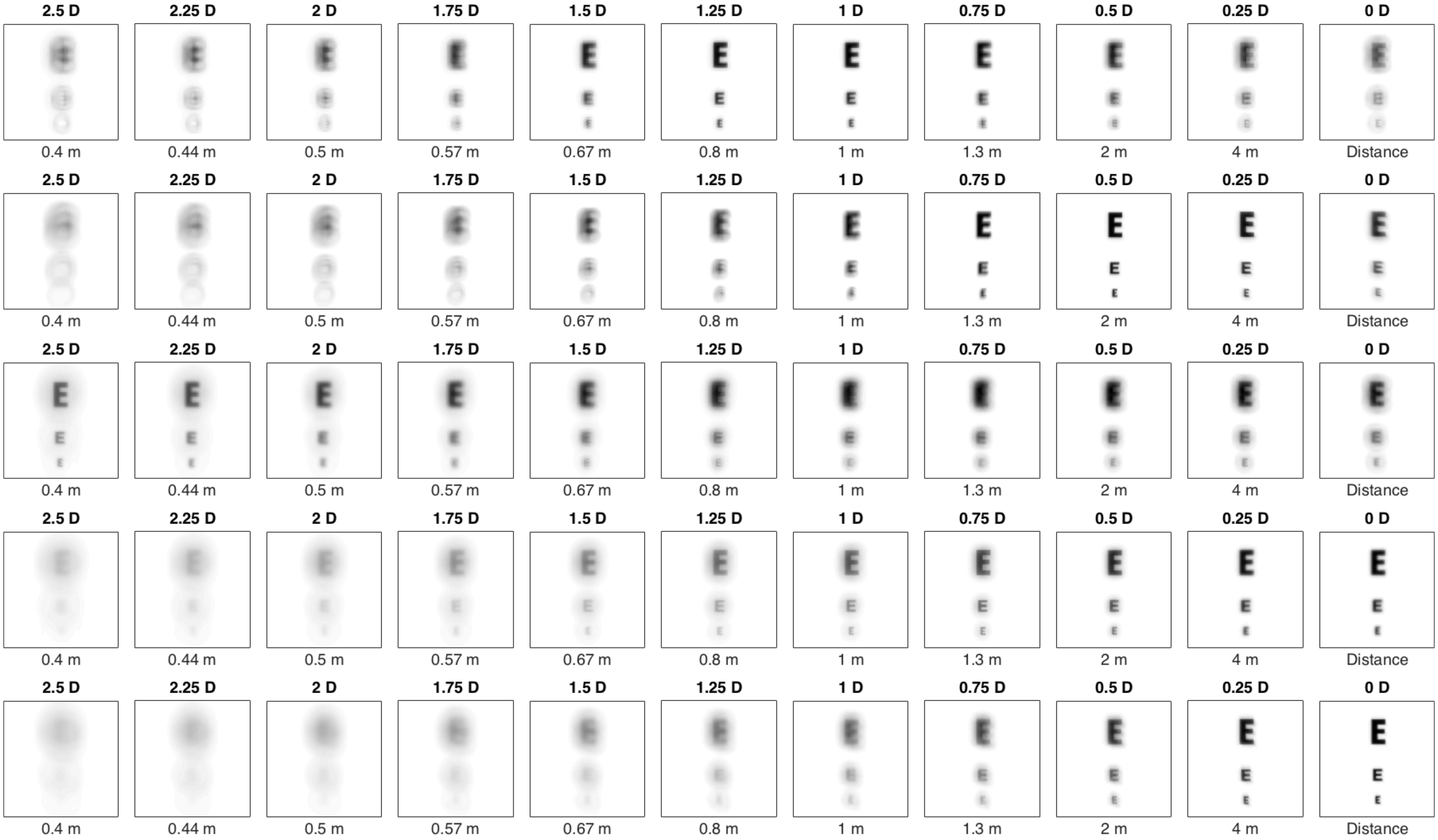

Figure 5.16: Semimonthly and Monthly Contacts - High Add, 4mm pupil. Images assume zero accommodation and are generated monocularly. From top to bottom: AV OASYS, Biofinity +2.5 D, Biofinity +2.5 N, Purevision, Purevision2

Results for the monocular images from the daily disposable and semimonthly/monthly disposable images are summarized in Table . The images in Figures 5.11 - 5.16 are generated in the monocular case (similarly, binocularly but with homogeneously fit contact lenses) with no accommodation included in the simulation.

Contact Lens	Low add	Med. add	High add	Note	Figures
Dailies					
Air Optix	1.25	1.75+	2.50		5.11, 5.12, 5.13
AV MOIST	0.75	1.50	2.50-		5.11, 5.12, 5.13
Biotrue	1.50	–			5.11, 5.13
Clariti	1.25	–	2.00+		5.11, 5.13
DACP	1.25	1.75+	2.50		5.11, 5.12, 5.13
Proclear	0.50	0.50	0.50		5.11, 5.12, 5.13
Semi-/Monthly					
AV OASYS	1.50	2.50	1.50		5.37, 5.38, 5.39
Biofinity D	1.00+	1.00	1.00	lens: +1.00D	5.37, 5.38, 5.39
	0.75-			lens: +1.50D	
Biofinity N	1.75	1.75+	2.50+	lens: +1.00D	5.37, 5.38, 5.39
	1.75			lens: +1.50D	
Purevision	1.25+	–	2.50		5.37, 5.39
Purevision2	0.75-	–	1.50-		5.37, 5.39

Table 5.2: Daily and Semimonthly/Monthly Contact lens performance summary, approximate range of focus given in diopters. Right column lists figures the contact data appears in.

Semimonthly and Monthly contact lenses

Homogeneously fitted contact lenses In Figures 5.17 through 5.21 we show the effects of pupil size for homogeneously fit binocular images for Daily contact lenses. Similar to the previous section, the DACP lenses shown in Figure 5.17 show slightly better performance at the 4mm pupil size compared to the 3mm pupil. The Acuvue Moist and Oasys lenses show similar performance with 3mm and 4mm pupils, shown in Figure 5.18 and 5.22 respectively. The Biotrue lens, images shown in Figure 5.19, show nearly similar performance at both pupil sizes, with about a 0.25D greater range at the larger 4mm pupil size. In Figure 5.20 is shown images for the Clariti lenses. The Clariti lenses don't show much pupil size dependent performance issues, for a 3mm and 4mm pupil. The 4mm pupil does give slightly better performance in the high add lens (third and fourth images in Figure 5.20) with about 0.75D greater range. The Proclear lens images shown in Figure 5.21 displays better performance at the 3mm pupil size, with about 0.5D greater range.

In Figures 5.23 through 5.26, pupil size dependent performance is shown for Monthly contact lenses. Overall, the Biofinity D lenses seem to exhibit marginally better performance at the 3mm pupil size for all add powers, shown in Figure 5.23. The Biofinity N lenses, shown in Figure 5.24, exhibit better performance at the 3mm pupil size, but show across the board improvement over the Biofinity D lenses. Purevision lenses shown in Figure 5.25 show similar performance between the pupil sizes for the low add lens, yet exhibit about a 0.25D-0.5D performance improvement at the 4mm pupil over the 3mm pupil. The Purevision2 lenses in Figure 5.26 exhibit almost no pupil size dependent performance over these pupil size.

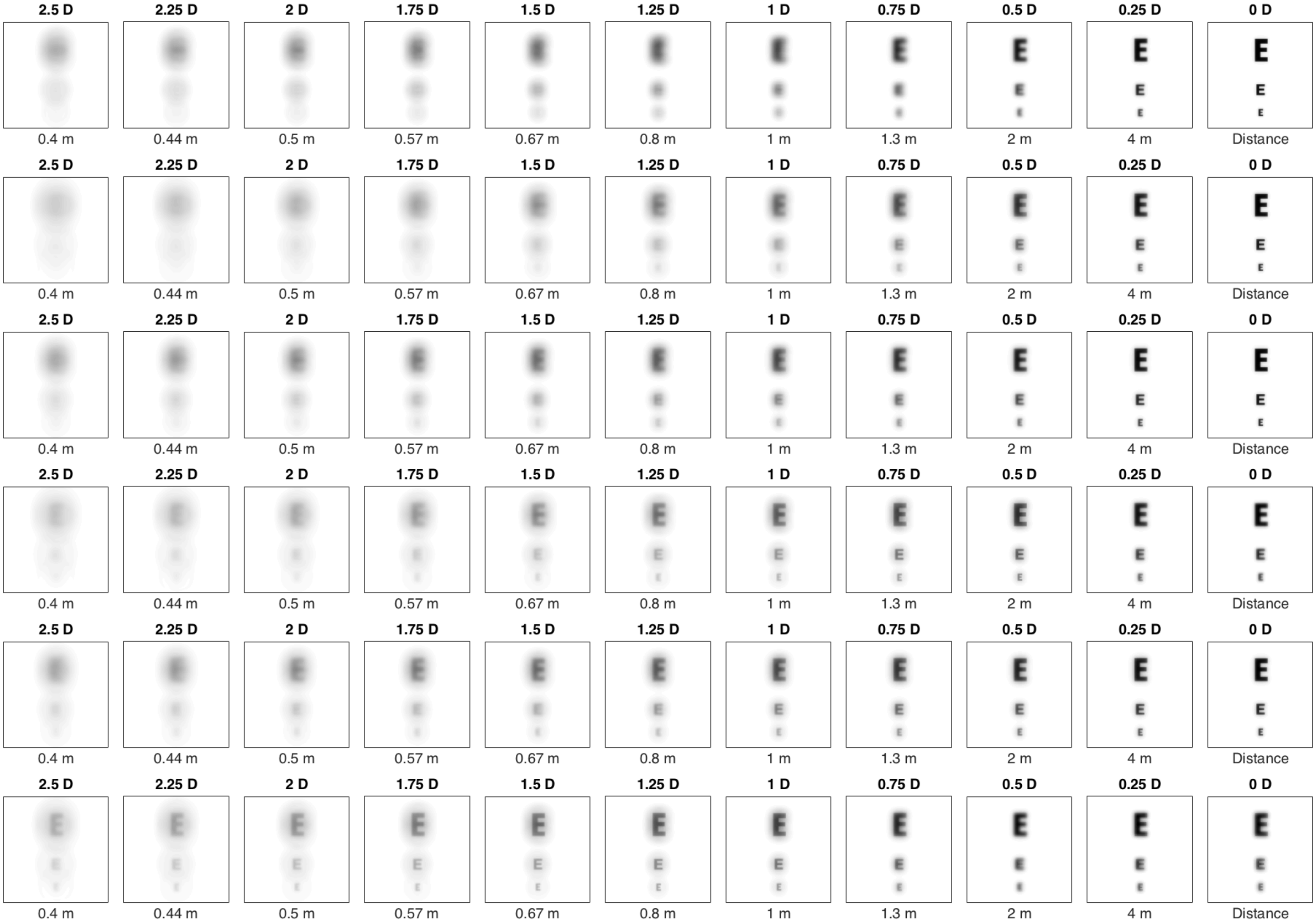

Figure 5.17: Dailies Contacts - DACP and Air Optix. Images assume zero accommodation and are generated monocularly. From top to bottom: low add with 3mm pupil, low add with 4mm pupil, medium add with 3mm pupil, medium add with 4mm pupil, high add with 3mm pupil, and high add with 4mm pupil.

Effect of pupil size As discussed in previous sections, the power profile of many multifocal contact lenses, specifically all of the lenses used in this study, have a radial power profile. Given this radial power profile of both multifocal IOLs and multifocal contact lenses, pupil size can play a role in the effective power profile of the lens as well as the object distances that will be in focus.

Mixed add power combinations Some contact lens fitting guides recommend the fitting of different lenses (add power) on the dominant and non-dominant eye. As will be discussed in Section 5.3.3.3, to produce binocular simulated images we take an equally weighted average of the images produced from each eye. This becomes particularly important for images simulated with contact lenses that are fit with different add powers on the dominant and non-dominant eyes. Figures 5.32 through 5.31 show the effects of pupil size for each set of mixed binocular.

Contact Lens	Combination			Pupil size (mm)		Figures
Dailies						
Air Optix	Low/Med	Med/High		3	4	5.30, 5.31
AV MOIST	Low/Med	Med/High	Low/High	3	4	5.27, 5.28, 5.29
DACP	Low/Med	Med/High		3	4	5.30, 5.31
Semi-/Monthly						
AV OASYS	Low/Med	Med/High		3	4	5.32, 5.33
Biofinity	+2.00D D/N	+2.50D D/N		3	4	5.34, 5.35

Table 5.3: Mixed Binocular Contact lenses

Figure 5.27 shows the Acuvue Moist lenses with a combination of Low and Medium add. Here, the pupil size doesn't play as large of a role, similar performance is achieved at both pupil sizes, with slightly better contrast at the 3mm pupil size. Figure 5.28 shows the Acuvue Moist lenses with a combination of medium and high add powers. This

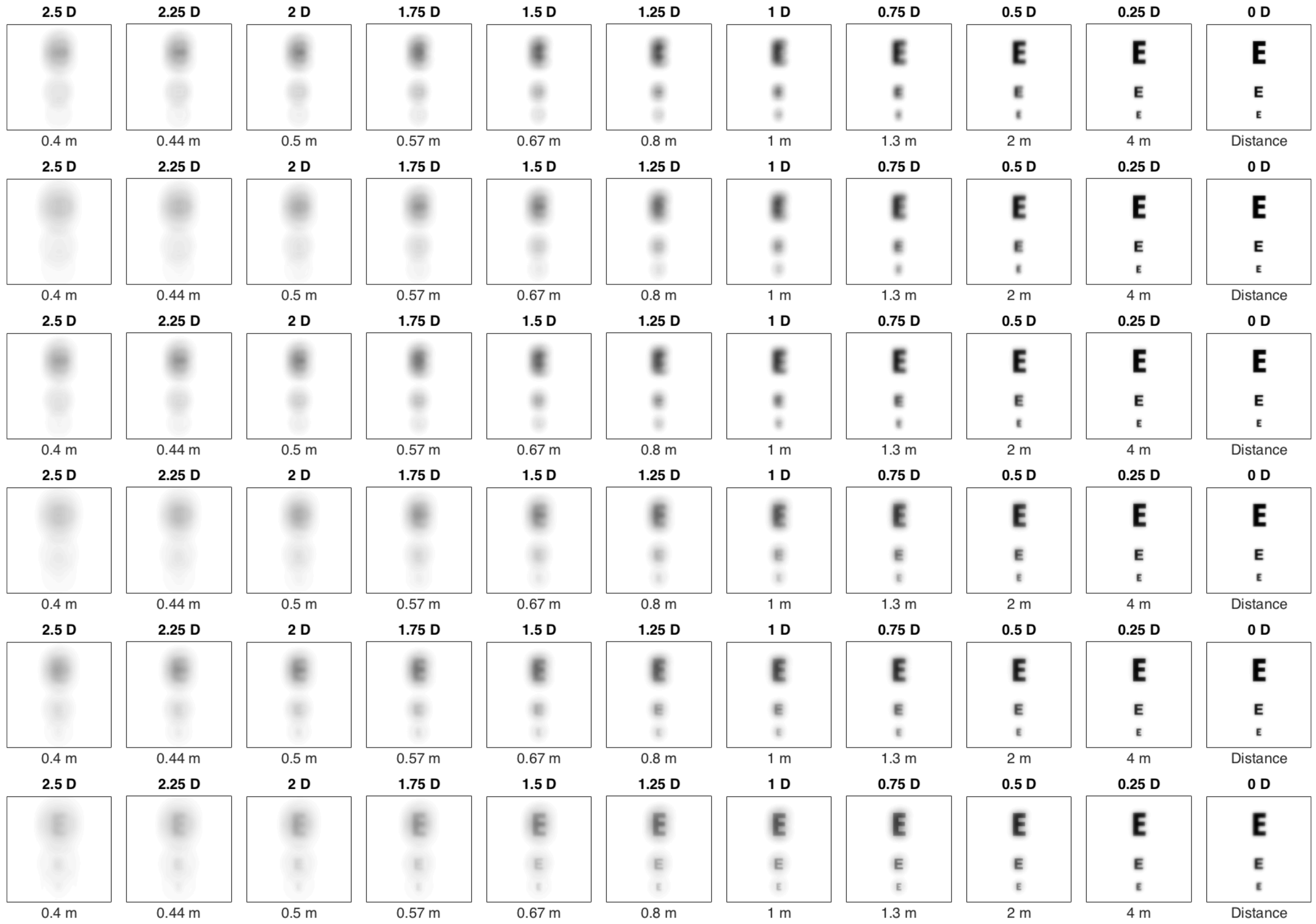

Figure 5.18: Dailies Contacts - Acuvue Moist. Images assume zero accommodation and are generated monocularly. From top to bottom: low add with 3mm pupil, low add with 4mm pupil, medium add with 3mm pupil, medium add with 4mm pupil, high add with 3mm pupil, and high add with 4mm pupil.

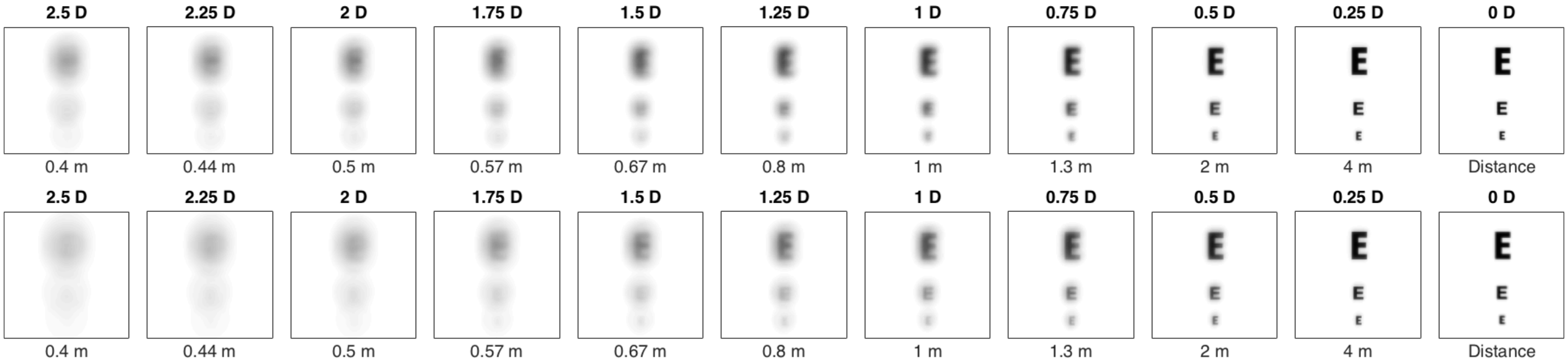

Figure 5.19: Dailies Contacts - Biotrue. Images assume zero accommodation and are generated monocularly. From top to bottom: low add with 3mm pupil, low add with 4mm pupil.

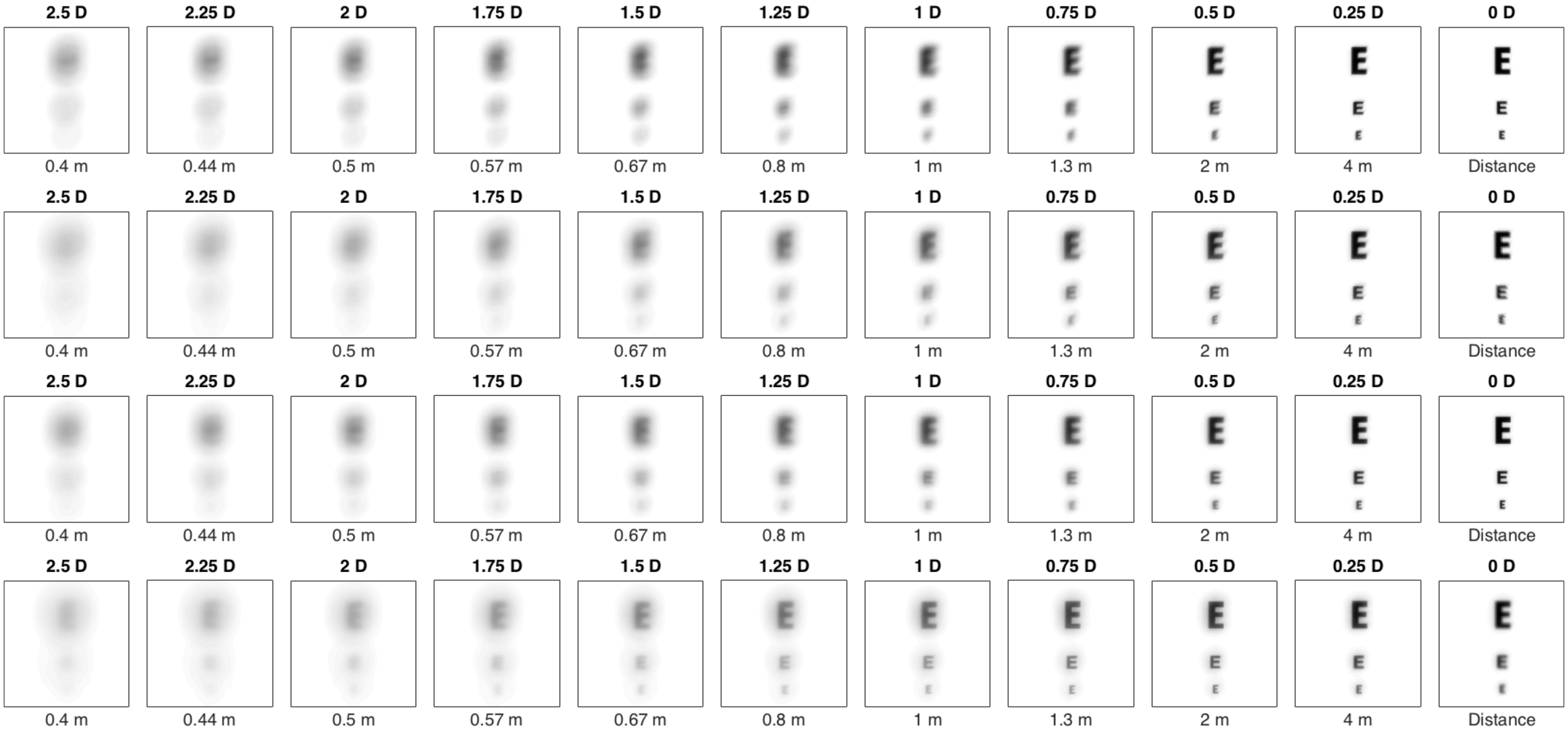

Figure 5.20: Dailies Contacts - Clariti. Images assume zero accommodation and are generated monocularly. From top to bottom: low add with 3mm pupil, low add with 4mm pupil, high add with 3mm pupil, and high add with 4mm pupil.

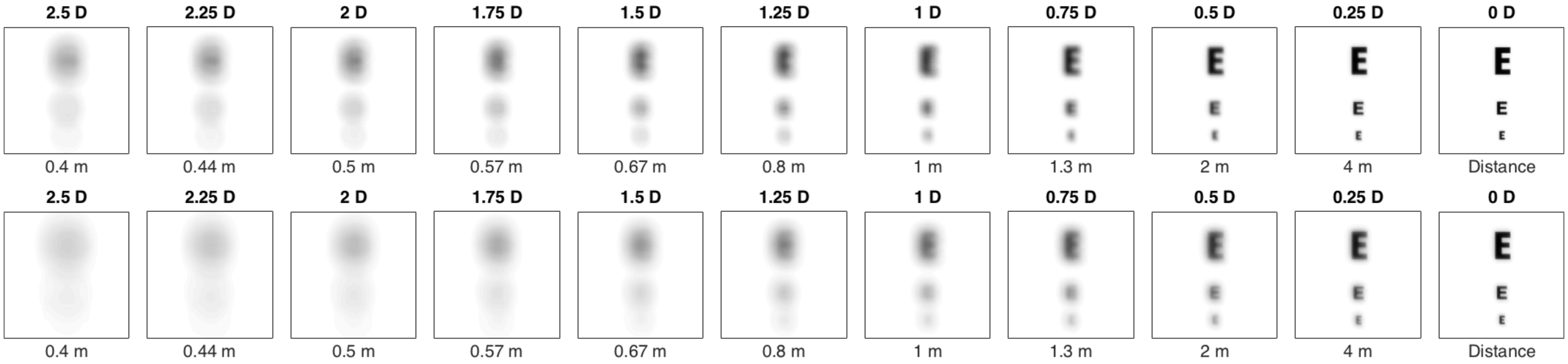

Figure 5.21: Dailies Contacts - Proclear. Images assume zero accommodation and are generated monocularly. From top to bottom: low add with 3mm pupil, low add with 4mm pupil, medium add with 3mm pupil, medium add with 4mm pupil, high add with 3mm pupil, and high add with 4mm pupil.

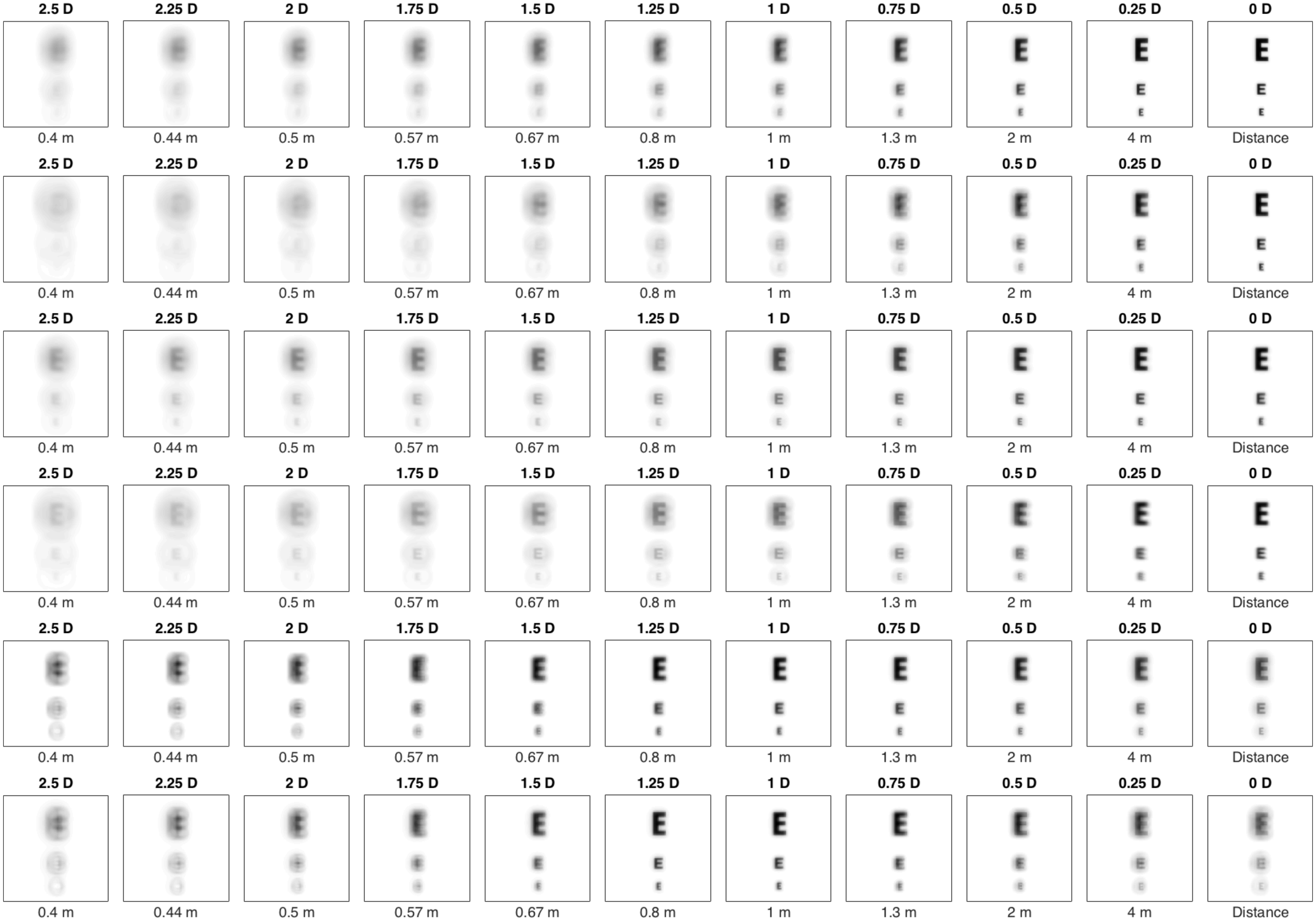

Figure 5.22: Semimonthly and Monthly Contacts - Acuvue Oasys. Images assume zero accommodation and are generated monocularly. From top to bottom: low add with 3mm pupil, low add with 4mm pupil, medium add with 3mm pupil, medium add with 4mm pupil, high add with 3mm pupil, and high add with 4mm pupil.

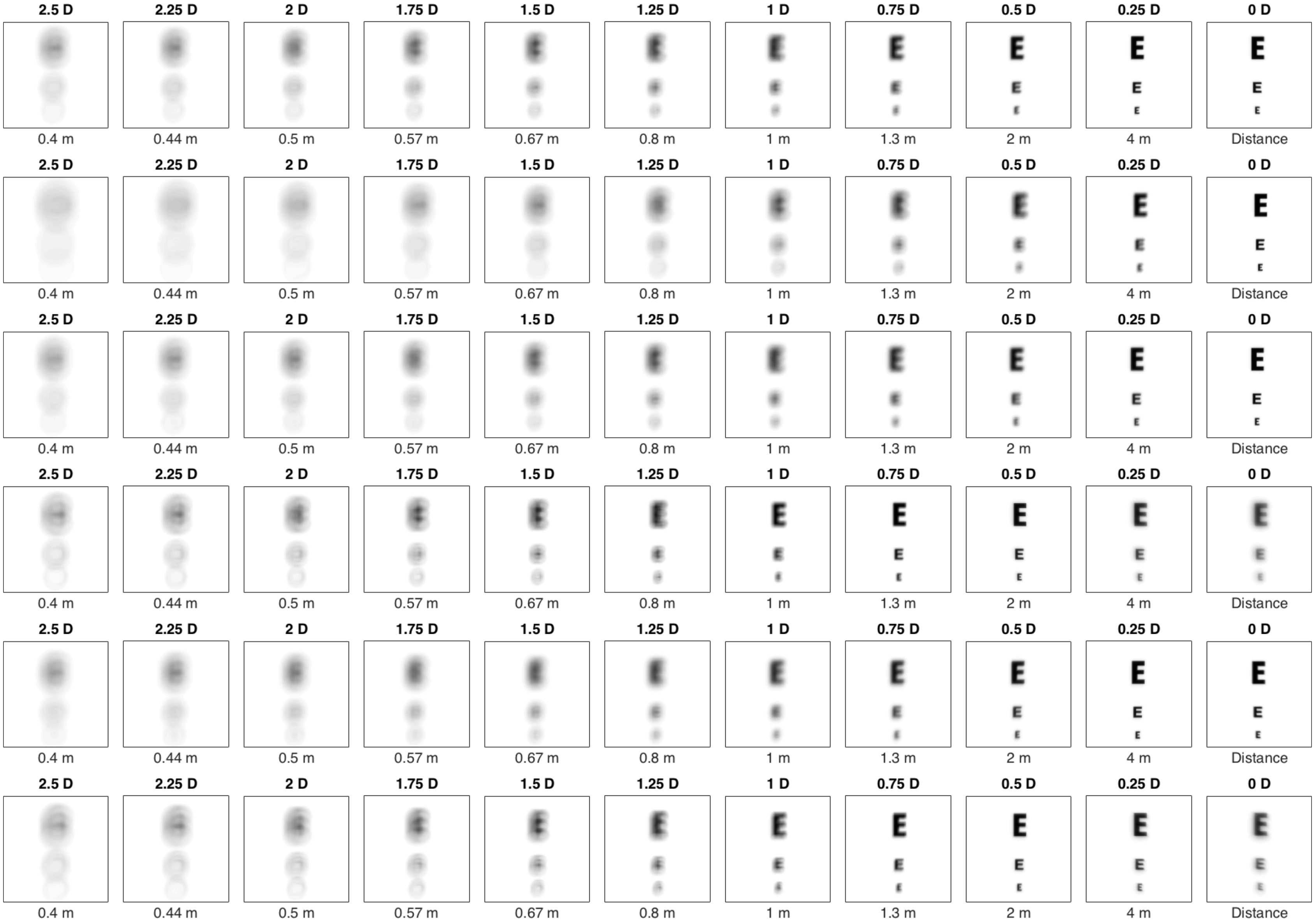

Figure 5.23: Semimonthly and Monthly Contacts - Biofinity center-distance lenses (D). Images assume zero accommodation and are generated monocularly. From top to bottom: +1.5D 3mm pupil, +1.5D 4mm pupil, +2.0D 3mm pupil, +2.0 4mm pupil, +2.5D 3mm pupil, and +2.5D 4mm pupil.

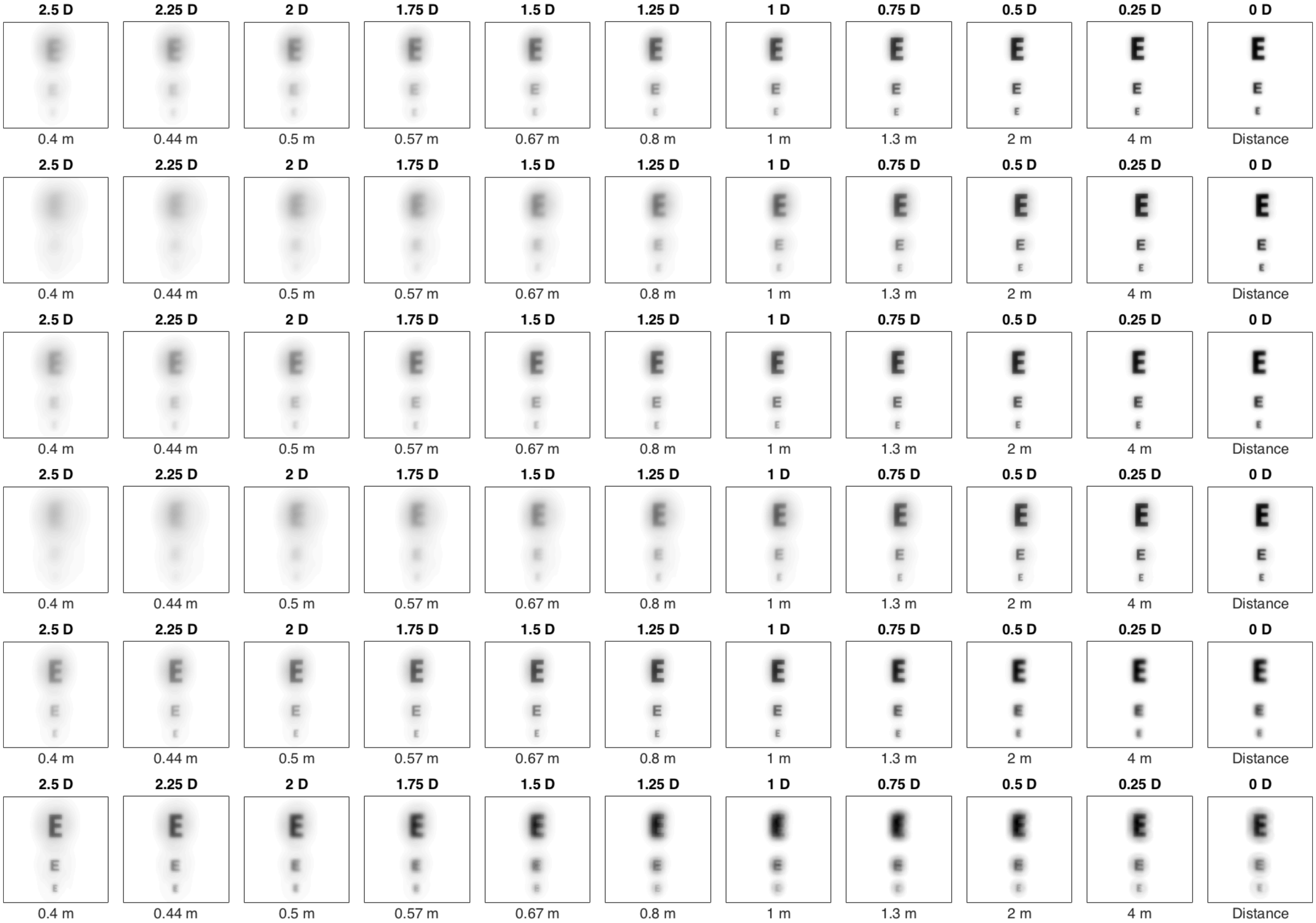

Figure 5.24: Semimonthly and Monthly Contacts - Biofinity center-near lenses (N). Images assume zero accommodation and are generated monocularly. From top to bottom: +1.5D 3mm pupil, +1.5D 4mm pupil, +2.0D 3mm pupil, +2.0 4mm pupil, +2.5D 3mm pupil, and +2.5D 4mm pupil.

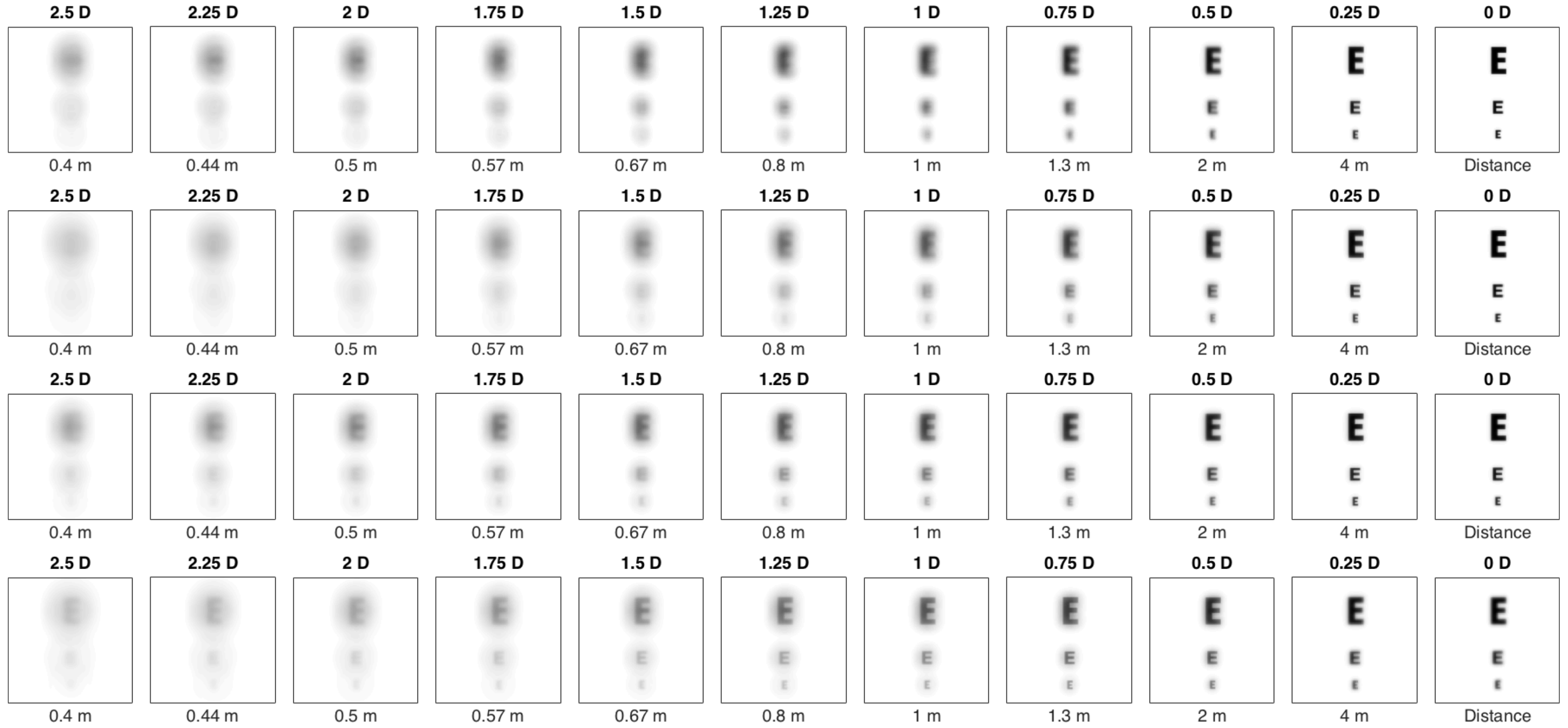

Figure 5.25: Semimonthly and Monthly Contacts - Purevision. Images assume zero accommodation and are generated monocularly. From top to bottom: low add 3mm pupil, low add 4mm pupil, high add 3mm pupil, high add 4mm pupil.

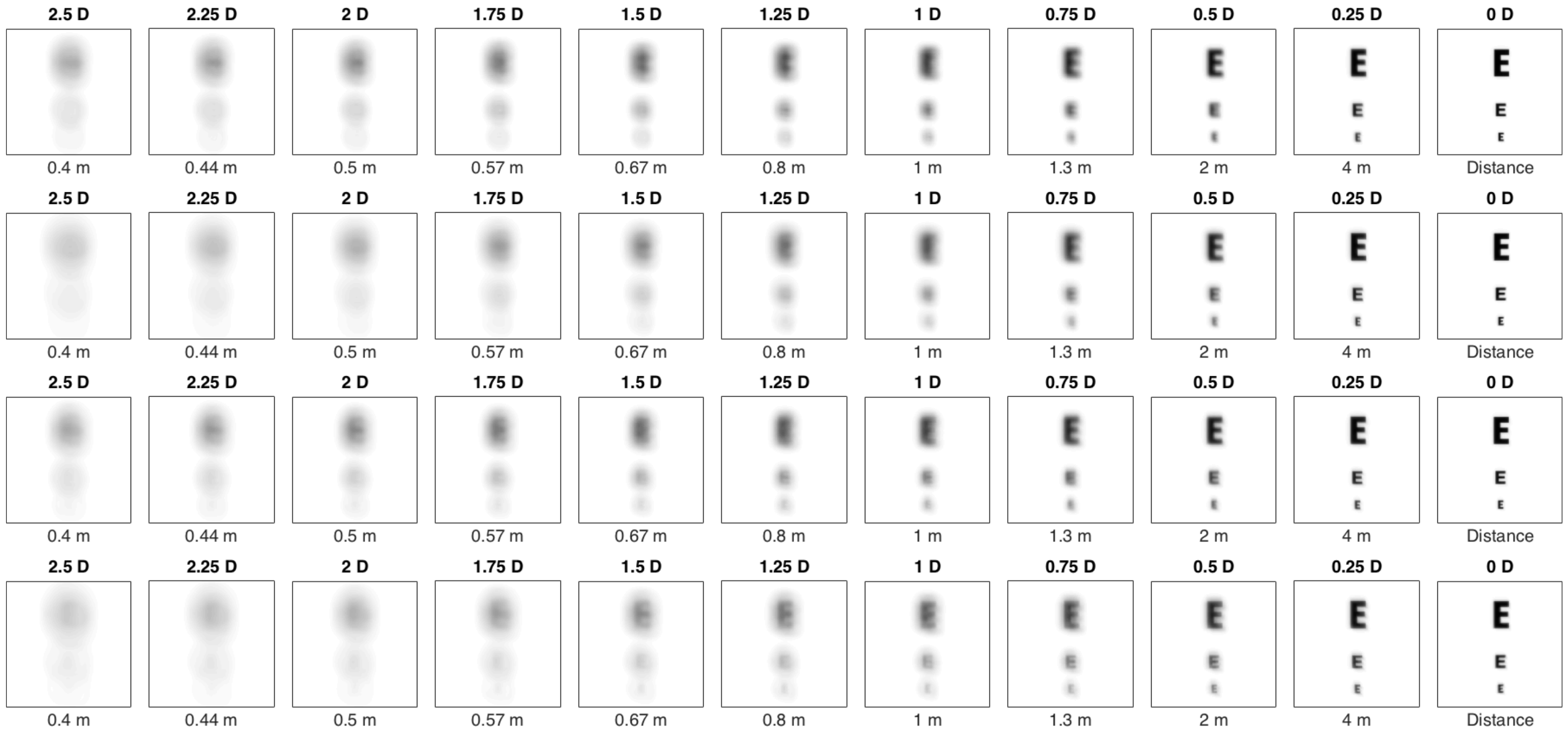

Figure 5.26: Semimonthly and Monthly Contacts - Purevision2. Images assume zero accommodation and are generated monocularly. From top to bottom: low add 3mm pupil, low add 4mm pupil, high add 3mm pupil, high add 4mm pupil.

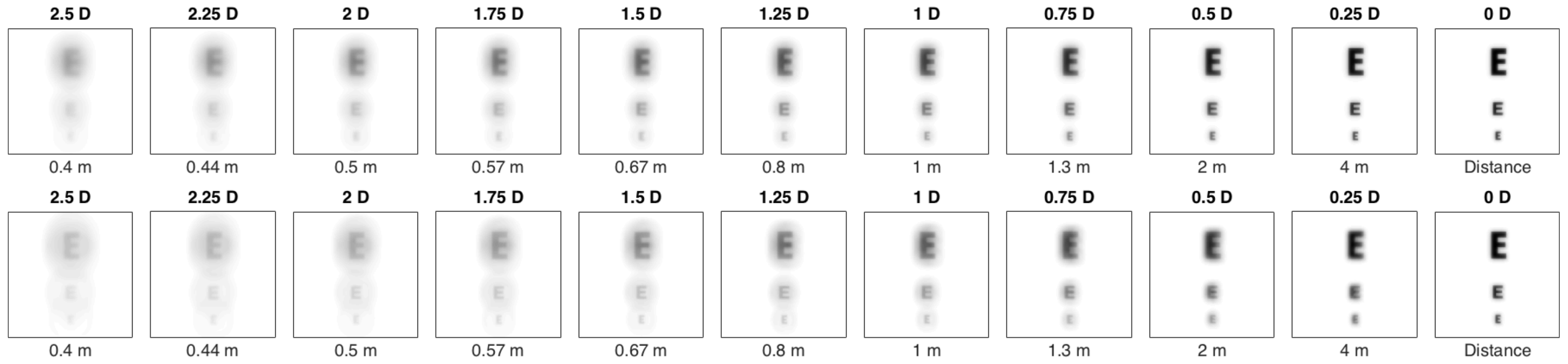

Figure 5.27: Dailies Contacts Binocular, AVMoist, Low-Medium, top 3mm, bottom 4mm

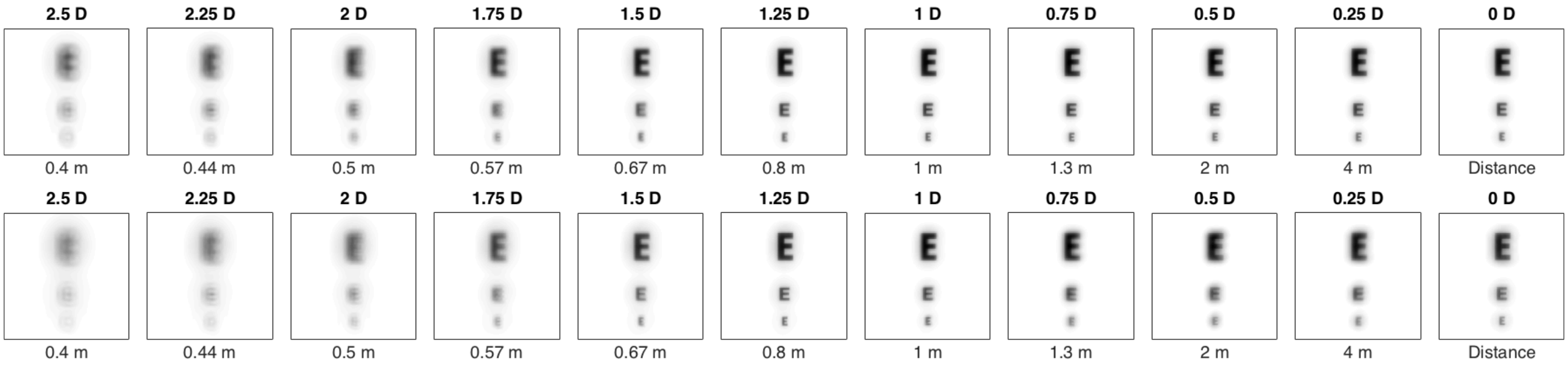

Figure 5.28: Dailies Contacts Binocular, AVMoist, Medium-High, top 3mm, bottom 4mm

combination of AV Moist lenses shows similar performance from both the 3mm and 4mm pupil sizes. Figure 5.29 shows the AV Moist lens combination of a low and high add power lens. This combination give slightly better performance at the 3mm pupil size for small amounts of accommodation, i.e. the images at 0.5D, the 3mm pupil image (top) is more clear than the bottom 4mm pupil image.

The Air Optix and Dailies Aqua Comfort Plus (DACP) lens combination of a low and medium add lens, shown in Figure 5.30, does show better performance at the 4mm pupil, with a clear 20/80 and 20/40 letter through about 1.5D while the smaller 3mm pupil only produces clear letters to about 0.5D or 0.75D. In Figure 5.31 the DACP medium-high add combination is shown with a similar disparity between performance at the 3mm and 4mm pupil sizes as with the low-medium add combination.

Figure 5.32 shows the Acuvue OASYS lens combination with low and medium add lenses, top shows a pupil diameter of 3mm and bottom shows a 4mm pupil. With this lens combination and these pupil sizes, the pupil size doesn't play a large role. The images between top and bottom are very similar, with the 4mm pupil (bottom) set of images providing slightly clearer images through 1.25D. Overall, very similar. Figure 5.33 shows a combination of the Acuvue OASYS Medium and High add lenses for both 3mm and 4mm pupil sizes. The bottom row of images shows better performance than the 3mm pupil for larger accommodation values near the left end.

The Biofinity lens fitting guide suggests that a D-N combination is only fit for add powers of +2.0D and +2.5D. Figure 5.34 shows an image set for a 3mm pupil (top) and 4mm pupil (bottom) for the +2.0D D-N lens combination. With a 3mm pupil, performance is diminished sooner than the 4mm pupil, yet the 4mm pupil does produce significant blur in the mid-range near 1D, with good performance on either side. Figure 5.35 shows the +2.5D add D-N combination exhibiting a similar feature as the +2.0D lenses. The 3mm pupil shows good performance through 2.5D yet the 4mm pupil does

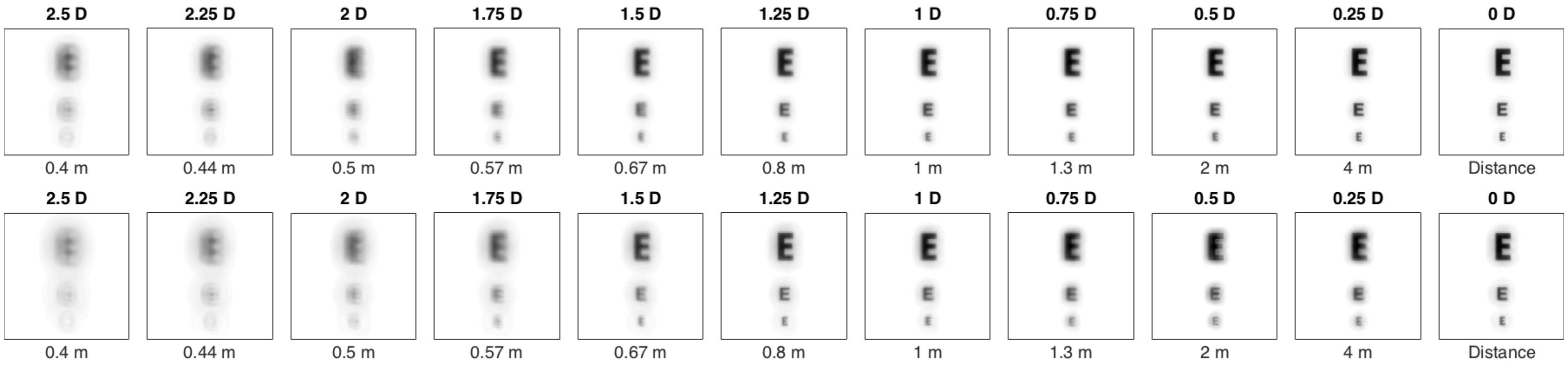

Figure 5.29: Dailies Contacts Binocular, AVMoist, Low-High, top 3mm, bottom 4mm

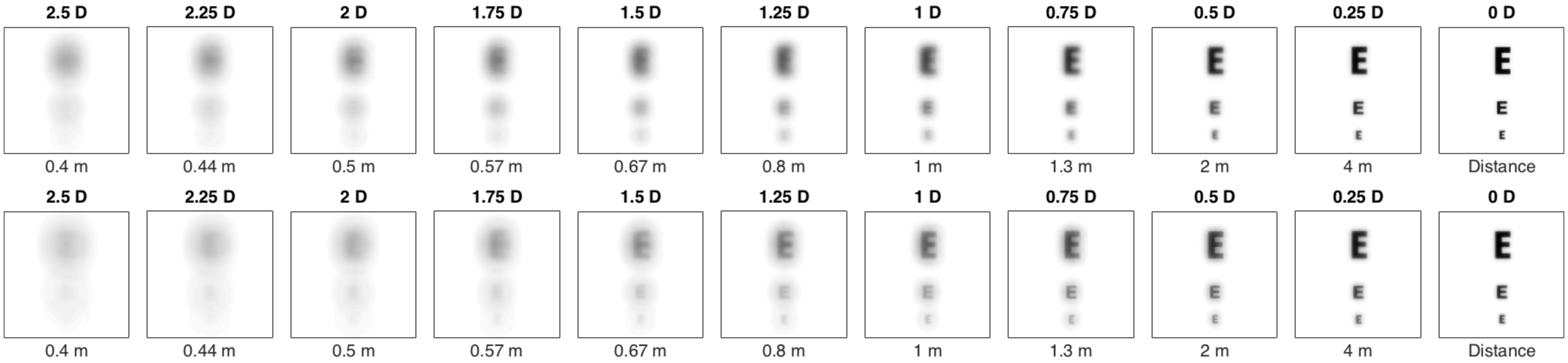

Figure 5.30: Dailies Contacts Binocular, Air Optix/DACP, low-medium, top 3mm, bottom 4mm

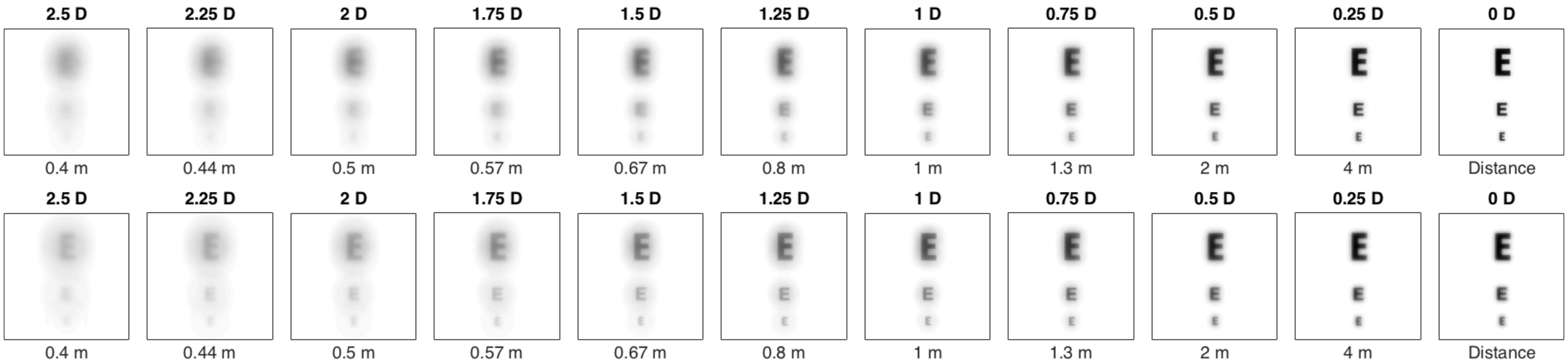

Figure 5.31: Dailies Contacts Binocular, Air Optix/DACP, Medium-High, top 3mm, bottom 4mm

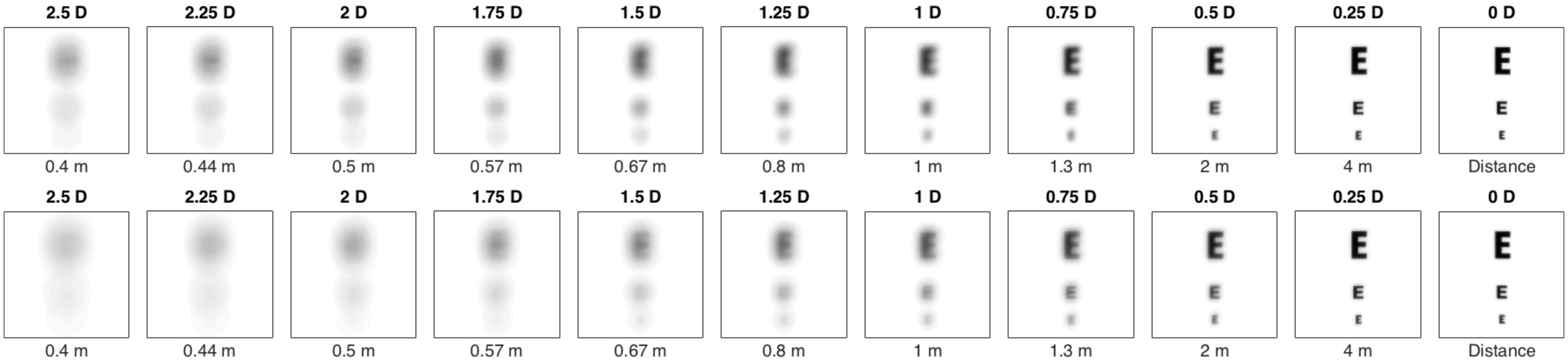

Figure 5.32: Semimonthly and Monthly Contacts Binocular, AV OASYS Low-medium combination, top 3mm, bottom 4mm

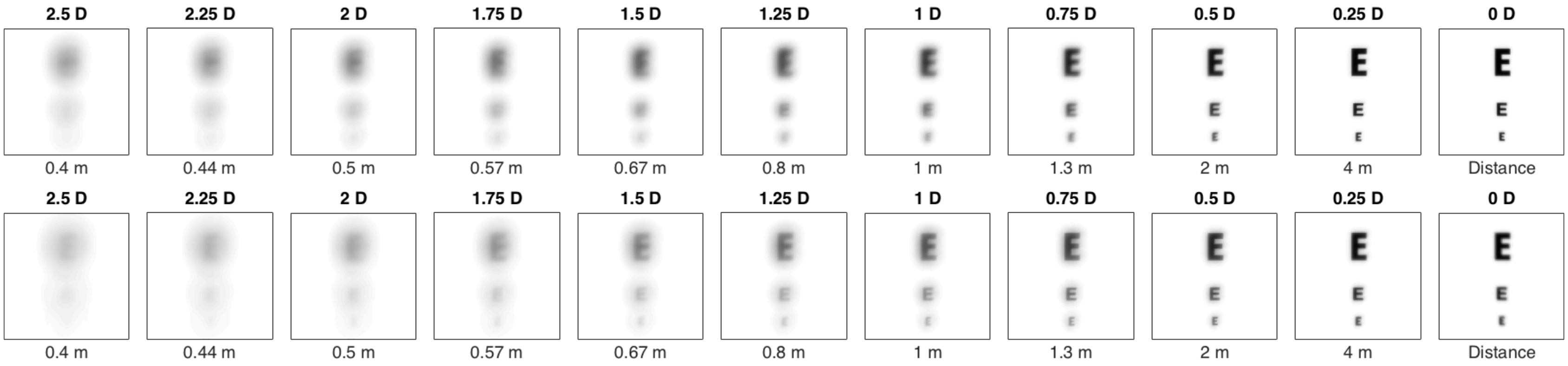

Figure 5.33: Semimonthly and Monthly Contacts Binocular, AVOASY Medium-High combination, top 3mm, bottom 4mm

have diminished performance near the 1D mark.

Of the four lenses that are fit heterogeneously on the dominant and non-dominant eye, the Acuvue Moist and Acuvue OASYS show the most similar performance between a 3mm and 4mm pupil size. The DACP lenses and the Biofinity lenses both exhibit pupil size dependent performance changes.

Binocular dominance Some multifocal contact lens fitting guides recommend fitting a patient with disparate add power on the dominant and non-dominant eye. The literature gives mixed results on the psychophysical mechanisms behind binocular acuity and is generally not in agreement [41, 42]. Nonetheless, it has been shown that ocular dominance in binocular vision tasks may be task dependent [41–43]. Our general approach for modeling binocular vision is to simply take an equally weighted average of the images produced with the left and right eye. Figure 5.36 shows what we consider the two extremes of a simplistic model for the task of binocular vision, namely a "winner take all" approach and an equally weighted approach. In the winner take all scenario, the dominant eye wins out over the non-dominant eye and the contribution to the image produced from the non-dominant eye is zero. On the other end of the spectrum, both eyes contribute equally. Further, Figure 5.36 shows the intermediate steps, in weighting steps of 0.1. Images generated for Figure 5.36 were generated with +2.50D Biofinity Multifocal lenses with a "D" lens on the dominant eye and an "N" lens on the non-dominant eye. The "D" and "N" lenses refer to the design power profile, "D" lenses are center-distance and the "N" lenses are center-near. This is to say that the central portion of the lens corrects for distance vision (center-distance, D) while the outer annulus corrects for near vision, or for near vision (center-near, N) with the outer annulus correcting for distance vision.

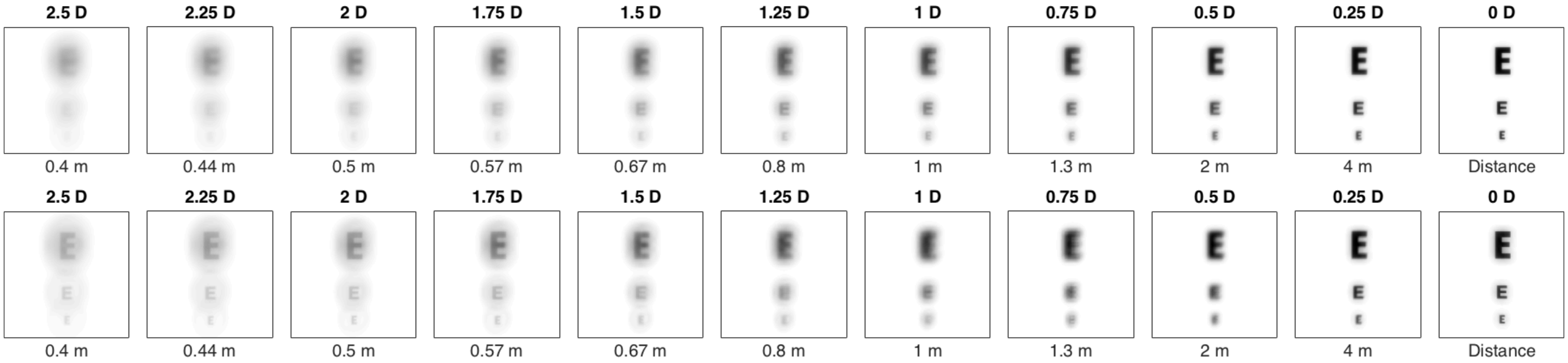

Figure 5.34: Monthly Contacts Binocular, Biofinity +2.0D D-N combination, top 3mm pupil, bottom 4mm pupil.

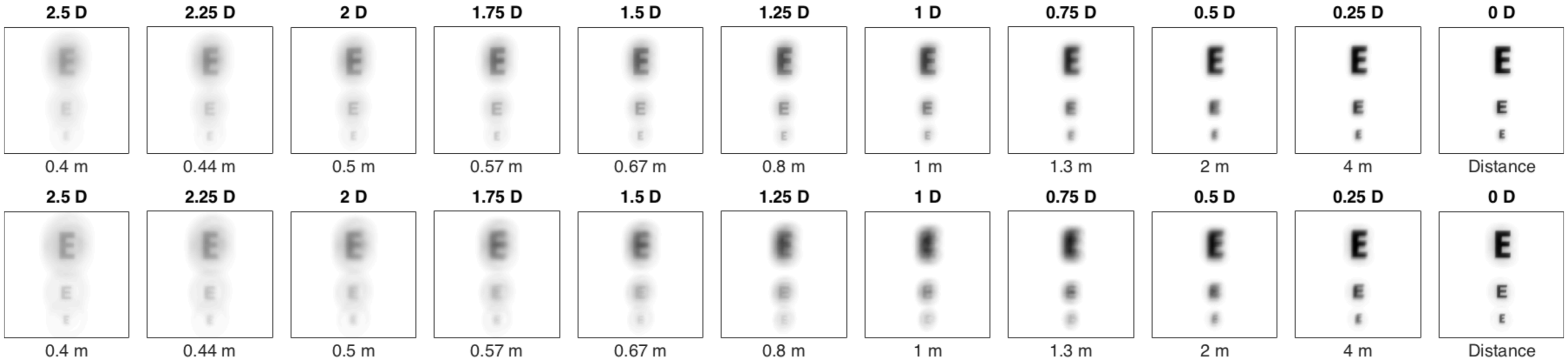

Figure 5.35: Monthly Contacts Binocular, Biofinity +2.5D D-N combination, top 3mm pupil, bottom 4mm pupil.

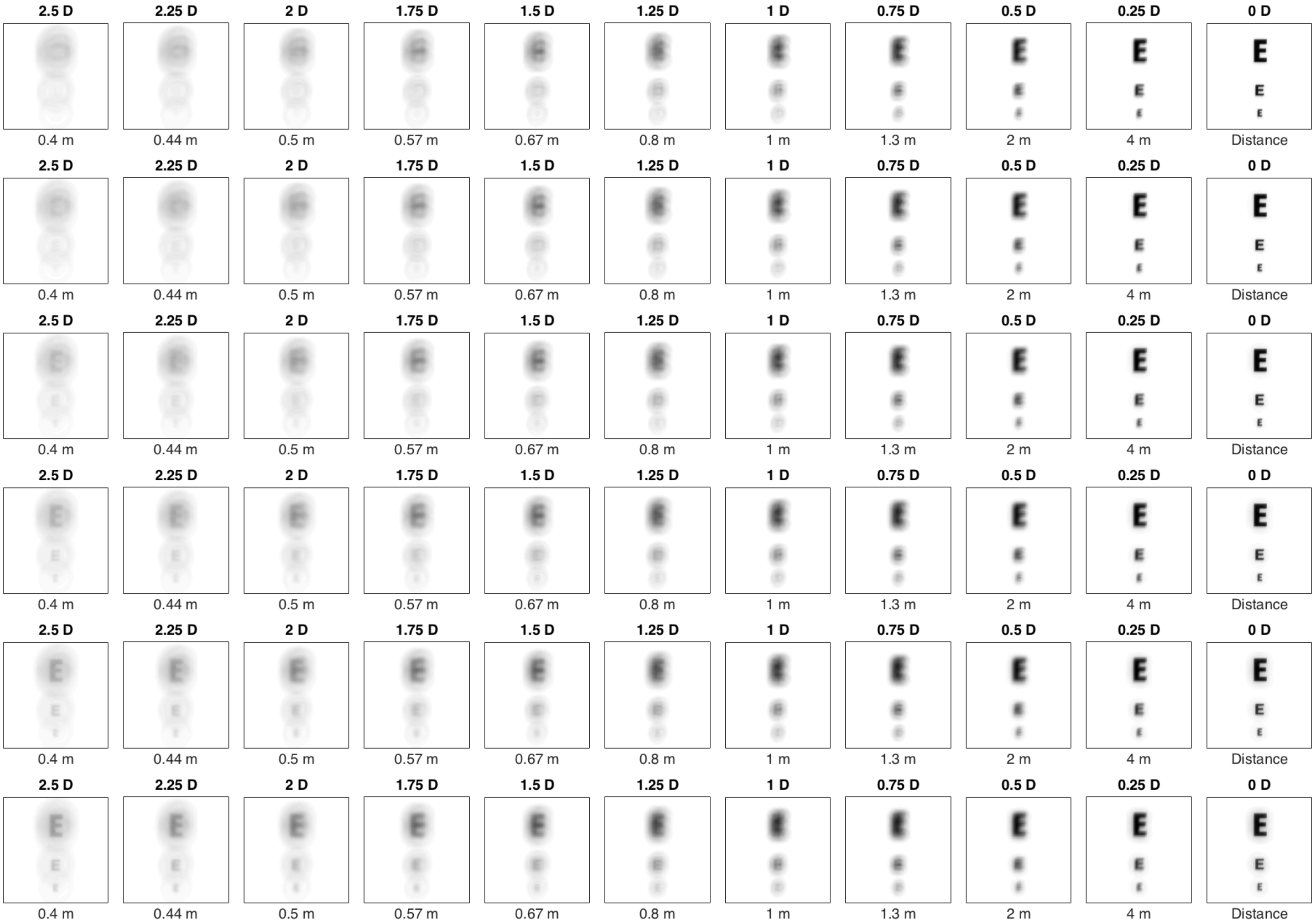

Figure 5.36: Comparison of weighting in producing binocular images. These images are meant to show the effect of weighting in binocular summation. Here we have used a Biofinity +2.50D D lens (center distance) on the dominant eye and a Biofinity +2.50D N lens (center near) on the non-dominant eye as per the Biofinity fitting guide. From top to bottom, weighting on the dominant eye used in average, 1 to 0.5 in steps of 0.1. Weighting on the non-dominant eye is 1 - (dominant weight). Top row shows the “winner take all” situation with the dominant eye weighted 100% and non-dominant eye weighted 0%. Bottom row shows an equally weighted binocular summation.

5.3.3.4 Multifocal Contacts - Quantitative Results

In the previous section, through focus simulated images were shown for three different letter sizes. These give a qualitative means of comparing the different multifocal contact lenses. With the tools developed previously, we can compare them quantitively. As discussed previously, the contact lenses that are compared in this work fall into two general categories: daily replacement and monthly or semi-monthly replacement. Figures 5.37 - 5.39 show through focus acuity curves for the dailies contact lenses broken down into low add, medium add, and high add powers. For all plots in this section, a winner take all approach was taken with respect to binocular summation, meaning only the dominant eye image is used. Fitting guides for each lens were used to determine which contact would be fit to the dominant eye.

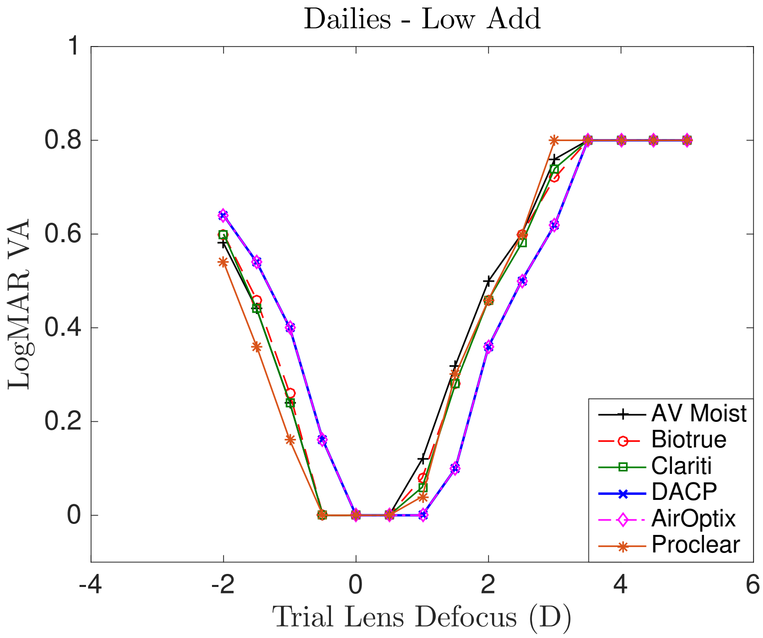

Figure 5.37: Daily Multifocal Contact Lens with low add power through focus acuity curves.

Figure 5.37 shows the low add dailies lenses. These lenses perform quite similarly. The Acuvue Moist, Biotrue, Clariti, and Proclear lenses show very similar performance with the DACP and Air Optix curves being similar in shape yet shifted to right.

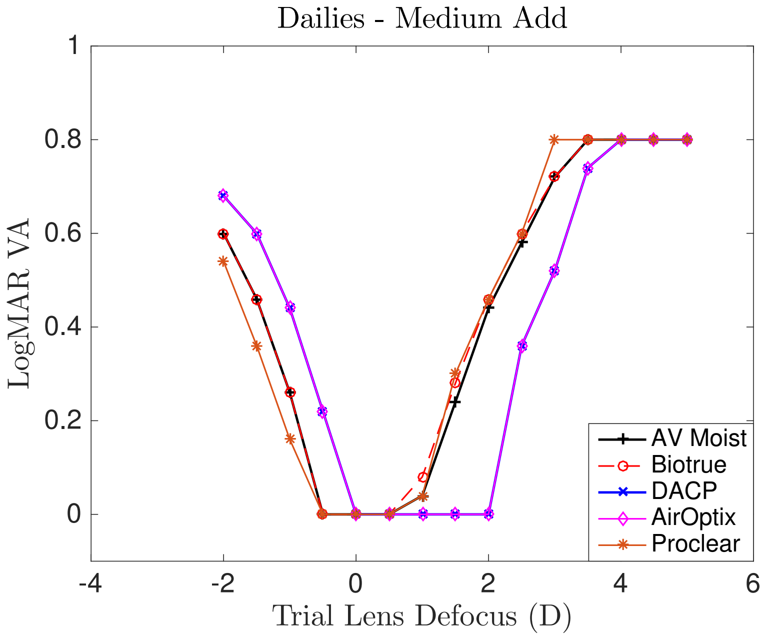

Figure 5.38: Daily Multifocal Contact Lens with medium add power through focus acuity curves.

In Figure 5.38 are the through focus acuity curves for the medium add dailies contacts. Here there is again similar performance in the AVMoist, Biotrue, and Proclear lenses. The DACP and AirOptix lenses have a larger region on good acuity out from 0D to 2D at logMAR VA of 0.

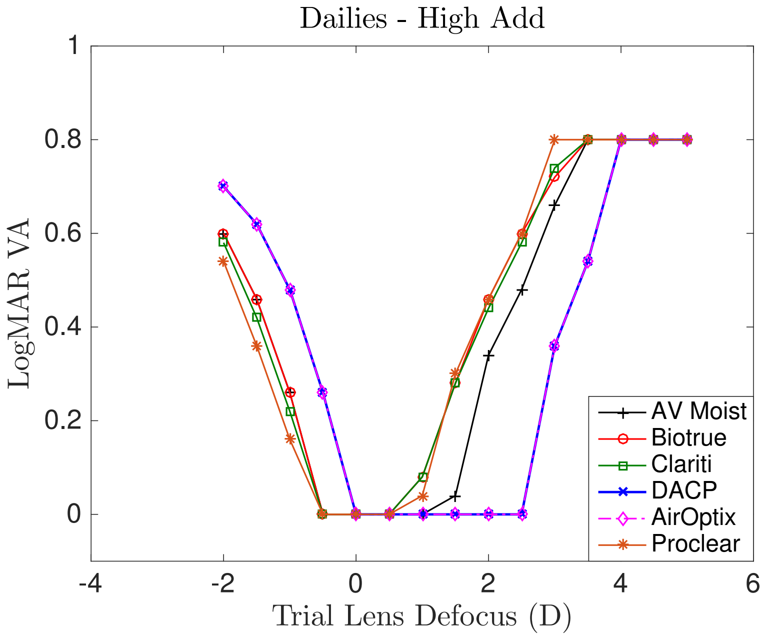

Figure 5.39: Daily Multifocal Contact Lens with high add power through focus acuity curves.

Finally, Figure 5.39 shows the high add dailies lenses. Again, the DACP and AirOptix perform much better, and achieve 20/20 acuity over a larger range from 0D to 2.5D than that of the rest of the group.

In Figures 5.40 - 5.42, defocus curves for semimonthly and monthly contact lenses are shown with low, medium, and high add powers. Low add lenses, Figure 5.40, perform nearly identically with a range of focus with 20/20 acuity of 1.00D.

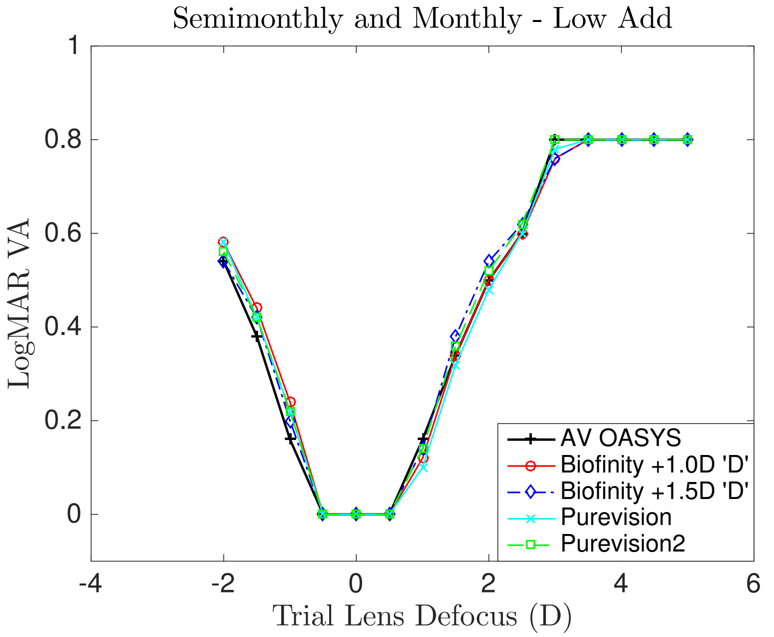

Figure 5.40: Semimonthly and Monthly Multifocal Contact Lens with high add power through focus acuity curves. In the low add category, we see that performance is very similar amongst the different lenses.

Shown in Figure 5.41 are medium add lenses. Purevision and Purevision2 are absent from this figure as there is not a medium add power available in those lenses. Acuvue Oasys performs far better than the Biofinity lens. The AV OASYS lens shows a range of focus with 20/20 acuity of 2.50D, while the Biofinity shows a range of 1.00D.

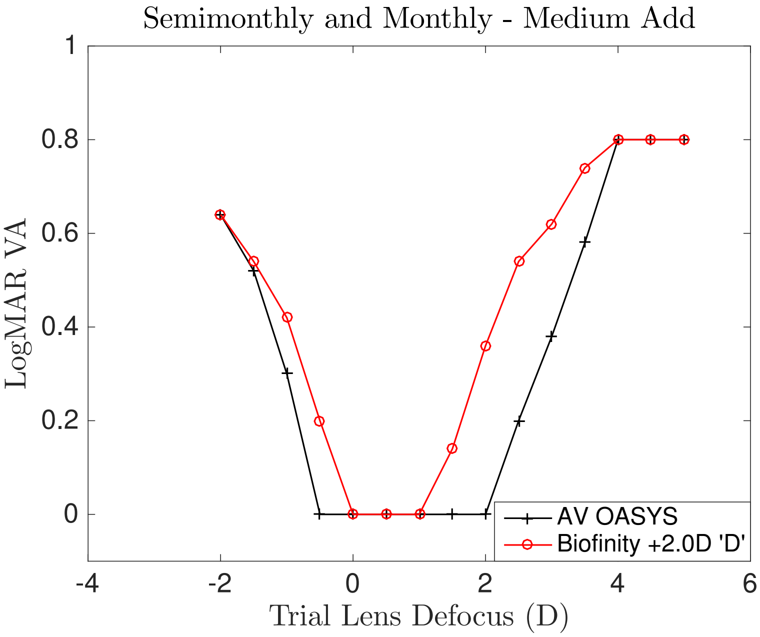

Figure 5.41: Semimonthly and Monthly Multifocal Contact Lens with high add power through focus acuity curves. At the medium add level, we see AV OASYS having a larger range of focus than that of the Biofinity lens.

The high add lenses in Figure 5.42 display interesting behavior. The Purevision lens shows an range of focus of 2.00D, while the rest of the field shows a range of focus of 1.00D.

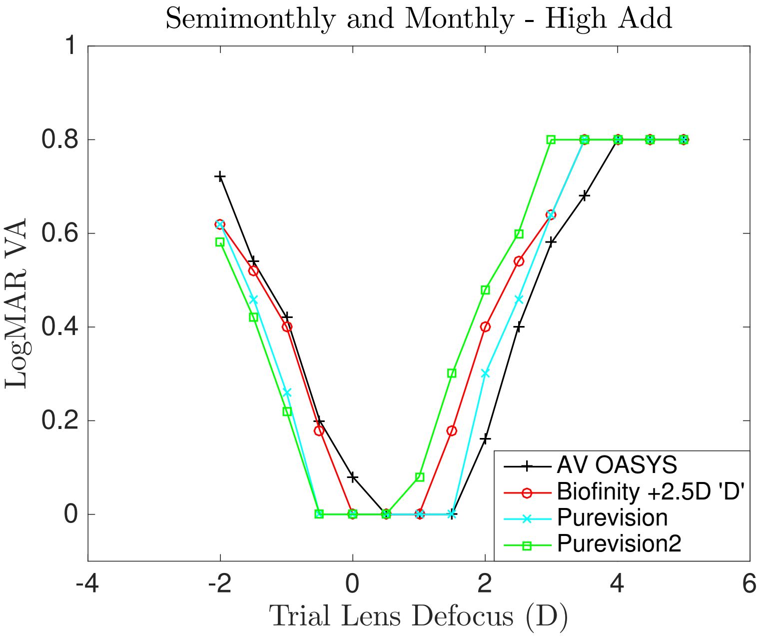

Figure 5.42: Semimonthly and Monthly Multifocal Contact Lens with high add power through focus acuity curves. Purevision performs best here, with a range of focus of 2.00D with 20/20 acuity. The AV OASYS, Biofinity, and Purevision2 lenses all show a range of focus with 20/20 acuity of 1.00D.

CHAPTER 6

CONCLUSION

In Chapter 1 the necessary building blocks were laid out in order for the reader to have an understanding of the visual system as well as common maladies and possible solutions. Chapter 2 discusses the necessary mathematics and methods used for simulating images for a given optical system. Chapter 3 examines the motivation for simulating three dimensional images for a given optical system as well as the methods used for this dissertation. In Chapter 4 presbyopia and its treatment Finally, Chapter 5 is concerned with the software and methods used to estimate and predict visual acuity for a range of multifocal ophthalmic optical elements, namely the ReVision Optics Raindrop Corneal Inlay, The Alcon Acrysoft ReSTOR multifocal IOL, and a range of multifocal contact lenses from various manufacturers.

We have shown that our software produces results two-fold. The software can generate images, either of real-scene simulations or of letter targets, through focus for a given ophthalmic appliance. These images can then be compared either qualitatively by looking at the images themselves or quantitatively by feeding them through the visual acuity estimation software. Using one study, clinical data from three cohorts having been implanted with three different intraocular lenses respectively, we were able to adjust the knobs or free parameters in the visual acuity estimation algorithm such that clinical data was by and large reproduced within the bounds of the clinical data standard deviation. With this choice of free parameters set, we can apply the algorithm to an array of multifocal contact lenses used in the treatment of presbyopia and compare their performance quantitively in the form of through focus acuity curves. Our novel metrics that enable the VA estimation mimic some of the processing done at the retina-level. These metrics and algorithms can be used to compare performance of other ophthalmics with relative ease.

REFERENCES

[1] A Duane. Studies in Monocular and Binocular Accommodation, with Their Clinical Application. *Transactions of the American Ophthalmological Society*, 20:132–157, 1922.

[2]

[3] C A Curcio, K R Sloan, R E Kalina, and A E Hendrickson. Human photoreceptor topography. *The Journal of comparative neurology*, 292:497–523, 1990.

[4] H L Liou and N A Brennan. Anatomically accurate, finite model eye for optical modeling. *Journal of the Optical Society of America. A, Optics, image science, and vision*, 14(8):1684–1695, 1997.

[5] Wikipedia. Benjamin franklin — wikipedia, the free encyclopedia, 2016. [Online; accessed 16-March-2016].

[6] Wikipedia. Bifocals — wikipedia, the free encyclopedia, 2016. [Online; accessed 16-March-2016].

[7] Jason Micali. *Interferometer for measuring dynamic corneal topography*. PhD thesis, University of Arizona, 2015.

[8] Jim Schwiegerling. Simulated retinal images following refractive surgery. In *Vision Sciences and its Applications*. Optical Society of America, 1999.

[9] Jack D Gaskill. *Linear systems, Fourier transforms, and optics*, volume 1. 1978.

[10] J W Goodman. *Introduction to Fourier Optics*. MaGraw-Hill, 2nd edition, 1996.

[11] J Schwiegerling. *Optical Specification, Fabrication, and Testing*. SPIE Digital Library. Society of Photo Optical, 2014.

[12] Zemax LLC Mark Nicholson. How to simulate high resolution images – zemax knowledgebase, October 31, 2008. [Online; accessed 28-March-2016].

[13] Ginni Grover, Ram Narayanswamy, and Ram Nalla. Simulating multi-camera imaging systems for depth estimation, enhanced photography and video effects. page IT3A.2. Optical Society of America, 2015.

[14] Robert J Schalkoff. *Digital image processing and computer vision*, volume 286. Wiley New York, 1989.

[15] Brian A Barsky. Vision-realistic rendering: Simulation of the scanned foveal image with elimination of artifacts due to occlusion and discretization. In *Computer Vision, Imaging and Computer Graphics. Theory and Applications*, pages 3–27. Springer, 2011.

[16] Brian a. Barsky, Michael J. Tobias, Derrick P. Chu, and Daniel R. Horn. Elimination of artifacts due to occlusion and discretization problems in image space blurring techniques. *Graphical Models*, 67(6):584–599, 2005.

[17] Brian A Barsky, Michael J Tobias, Derrick P Chu, and Daniel R Horn. Elimination of artifacts due to occlusion and discretization problems in image space blurring techniques. *Graphical Models*, 67(6):584–599, 2005.

[18] Brian Barsky, Michael Tobias, Daniel Horn, and Derrick Chu. Investigating Occlusion and Discretization Problems in Image Space Blurring Techniques. *First International Conference on Vision, Video, and Graphics*, (September 2003), 2003.

[19] Duco Hamasaki, Jin Ong, and Elwin Marg. The amplitude of accommodation in presbyopia*. *Optometry & Vision Science*, 33(1):3–14, 1956.

[20] Brien a Holden, Timothy R Fricke, S May Ho, Reg Wong, Gerhard Schlenther, Sonja Cronjé, Anthea Burnett, Eric Papas, Kovin S Naidoo, and Kevin D Frick. Global vision impairment due to uncorrected presbyopia. *Archives of ophthalmology (Chicago, Ill. : 1960)*, 126(12):1731–1739, 2008.

[21] Arthur Bradley, Harun Abdul Rahman, P Sarita Soni, and XiaoXiao Zhang. Effects of target distance and pupil size on letter contrast sensitivity with simultaneous vision bifocal contact lenses.pdf. *Optometry and Vision Science*, 70(6):476–481, 1993.

[22] Almudena Llorente-Guillemot, Santiago García-Lazaro, Teresa Ferrer-Blasco, Rafael J Perez-Cambrodi, and Alejandro Cerviño. Visual performance with simultaneous vision multifocal contact lenses. *Clinical and Experimental Optometry*, 95(1):54–59, 2012.

[23] Junoh Choi and Jim Schwiegerling. Optical performance measurement and night driving simulation of restor, rezoom, and tecnis multifocal intraocular lenses in a model eye. *Journal of Refractive Surgery*, 24(3):218–222, 2008.

[24] Martin Leyland and Edoardo Zinicola. Multifocal versus monofocal intraocular lenses in cataract surgery: A systematic review. *Ophthalmology*, 110(9):1789–1798, 2003.

[25] Hans Strasburger, Ingo Rentschler, and Martin Jüttner. Peripheral vision and pattern recognition: a review. *Journal of vision*, 11(5):13, 2011.

[26] H Snellen. Optotypi ad visum determinandum (letterproeven tot bepaling der gezichtsscherpte; probebuchstaben zur bestimmung der sehschaerfe). *Utrecht, The Netherlands: Weyers*, 1862.

[27] A G Bennett and R B Rabbetts. *Bennett and Rabbetts' Clinical Visual Optics*. Butterworth-Heinemann, 1998.

[28] Jim Schwiegerling. Field guide to visual and ophthalmic optics. SPIE Bellingham, WA, USA, 2004.

[29] Nancy B Carlson, Daniel Kurtz, David A Heath, Catherine Hines, and Roanne Flom. *Clinical procedures for ocular examination*, volume 3. McGraw-Hill New York, 2004.

[30] Selig Hecht, Simon Shlaer, and Maurice Henri Pirenne. Energy, quanta, and vision. *The Journal of general physiology*, 25(6):819–840, 1942.

[31] DA Baylor, TD Lamb, and King-Wai Yau. Responses of retinal rods to single photons. *The Journal of physiology*, 288(1):613–634, 1979.

[32] Gabriele Jordan, Samir S Deeb, Jenny M Bosten, and J D Mollon. The dimensionality of color vision in carriers of anomalous trichromacy. *Journal of vision*, 10(8):12, 2010.

[33] Samer Hattar, H-W Liao, Motoharu Takao, David M Berson, and K-W Yau. Melanopsin-containing retinal ganglion cells: architecture, projections, and intrinsic photosensitivity. *Science*, 295(5557):1065–1070, 2002.

[34] Ignacio Provencio, Ignacio R Rodriguez, Guisen Jiang, William Pär Hayes, Ernesto F Moreira, and Mark D Rollag. A novel human opsin in the inner retina. *The journal of Neuroscience*, 20(2):600–605, 2000.

[35] David M Berson, Felice A Dunn, and Motoharu Takao. Phototransduction by retinal ganglion cells that set the circadian clock. *Science*, 295(5557):1070–1073, 2002.

[36] JE Dowling. Information processing by local circuits: the vertebrate retina as a model system. *The neurosciences: Fourth study program*, pages 163–181, 1979.

[37] Stephen W Kuffler. Discharge patterns and functional organization of mammalian retina. *Journal of neurophysiology*, 16(1):37–68, 1953.

[38] Horace B Barlow. Summation and inhibition in the frog's retina. *The Journal of physiology*, 119(1):69, 1953.

[39] Roger F Steinert, Jim Schwiegerling, Alan Lang, Adam Roy, Keith Holliday, Enrique Barragán Garza, and Arturo S Chayet. Range of refractive independence and mechanism of action of a corneal shape–changing hydrogel inlay: Results and theory. *Journal of Cataract & Refractive Surgery*, 41(8):1568–1579, 2015.

[40] András Róka, Ádám Csapó, Barna Reskó, and Péter Baranyi. Edge Detection Model Based on Involuntary Eye Movements of the Eye-Retina System. *Sciences-New York*, 4(1):31–46, 2007.

[41] Einat Shneor and Shaul Hochstein. Eye dominance effects in conjunction search. *Vision Research*, 48(15):1592–1602, 2008.

[42] Jan Johansson, Gustaf Öqvist Seimyr, and Tony Pansell. Eye dominance in binocular viewing conditions. *Journal of vision*, 15(9)(21):1–17, 2015.

[43] Einat Shneor and Shaul Hochstein. Effects of eye dominance in visual perception. *International Congress Series*, 1282:719–723, 2005.